

**INVESTIGATING PHYSICS OF NANOSECOND-PULSED ARGON PLASMA  
DISCHARGES FOR A VLF PLASMA ANTENNA**

A Dissertation  
Presented to  
The Academic Faculty

by

Connie Y. Liu

In Partial Fulfillment  
of the Requirements for the Degree  
Doctor of Philosophy in the  
Daniel Guggenheim School of Aerospace Engineering

Georgia Institute of Technology

May 2019

Copyright © Connie Y. Liu 2019

**INVESTIGATING PHYSICS OF NANOSECOND-PULSED ARGON PLASMA  
DISCHARGES FOR A VLF PLASMA ANTENNA**

Approved by:

Dr. Mitchell Walker, Advisor  
School of Aerospace Engineering  
*Georgia Institute of Technology*

Dr. Morris Cohen, Co-Advisor  
School of Electrical and Computer  
Engineering  
*Georgia Institute of Technology*

Dr. Adam Steinberg  
School of Aerospace Engineering  
*Georgia Institute of Technology*

Dr. Wenting Sun  
School of Aerospace Engineering  
*Georgia Institute of Technology*

Dr. Lukas Graber  
School of Electrical and Computer  
Engineering  
*Georgia Institute of Technology*

Date Approved: May 9, 2019

“It’s a dangerous business, Frodo, going out your door. You step onto the road, and if you don’t keep your feet, there’s no telling where you might be swept off to.”

*J.R.R. Tolkien*

To my grandparents, 劉鼎錚、謝連景、彭鏡妹, who sparked my curiosity about the world and showed me the joy (and fun) of learning.

## ACKNOWLEDGEMENTS

Never was I more aware of how mentally, emotionally, and physically draining the doctoral research process was than when I was writing my dissertation and trying to condense four years of experiments, readings, successes, and failures into an intelligible document. It felt like there was always a new round of edits to make, and I was constantly chasing after that next state of being “done.” Without the support and encouragement of so many wonderful people, I would not be able to say that I have reached the end, and I am (actually) finally done.

First and foremost, my biggest thanks go to my family. They have been with me for every step of my academic journey and have bolstered me, challenged me, and inspired me. This dissertation and the successful completion of my Ph.D. is a testament to their unwavering love and support. To Mom and Dad, thank you for your understanding as I’ve criss-crossed the country every year in pursuit of balancing my academic aspirations and career goals. To Tom, thank you for being my model, for helping me reason through any problem, and for sharing epic soundtracks, trailers, and boss battle reactions – they provided me with much needed levity and entertainment during the writing process! To Amy, thank you for being my confidante, for motivating me to keep going no matter how rough the situation, and for conspiring with me about how *Game of Thrones* will end!

I was lucky to have two advisors, Professors Mitchell Walker and Morris Cohen, to guide me through my academic and research journey in graduate school. You challenged me to master topics beyond my initial interests and to adapt my technical skills and knowledge to new applications; you taught me to consider creative solutions and to ask what is the next step.

My committee was invaluable during my research process and thesis refining. Professor Adam Steinberg, I am grateful for your optics and spectrometer expertise during the set up for my experiment and for your patience as you taught me the basics of aligning

lenses and collimating light. Professors Lukas Graber and Wenting Sun provided insightful suggestions for plasma voltage breakdowns and working with nanosecond pulsers.

A special thank you to Professor Paulo Lozano at MIT and Dr. Kurt Polzin at NASA for nourishing my interest in electric propulsion and plasmas when I was an undergraduate student!

Much of my graduate experience has been defined by working at the High-Power Electric Propulsion Laboratory, and those experience have been enriched by my lab mates. Samuel Langendorf, I attended your Ph.D. defense my first day of graduate school, and you took the time that day and in the weeks that followed to make me feel welcome in the lab. Natalie Caruso, you worked magic on the beast that is VTF-1, and I'm glad you showed me the ropes (and the secrets) in getting it operational for my first solo test campaign. Jonathan Walker, you helped me navigate the collection of probes for that test when I could not distinguish a Langmuir from a Faraday, and your humor and experience were very much-appreciated. Aaron Schinder, I could always go to you for interesting discussions on math and theory; Cheong Chan, when I joined you on this project, you showed me the importance of relentlessly pushing towards the finish line and the necessity of good music when working. Lastly, Jason Frieman, thank you for being my "everything" mentor. You passed on Hall thruster testing knowledge, data analysis techniques, quals advice, and old lab lore. You were the person I called when I had issues in lab, from pumping down the chamber (thank you pump covers) to making a milli-Newton weight set, and what I learned from all those late-night tests have served me well in my graduate school years. You were right – I successfully crossed to the other side of the river!

For my peers, I wish you the best of luck in your research and careers post-graduate school – keep bringing back those wins! Nathan Brown, you were always there with a sympathetic ear for LabView struggles and uncooperative experiments. David Jovel, you were the social chair of the lab – you never hesitated to ask how we were doing or to

convince us to relax at Fellini's or Fox Bros. Jean Luis, your no-nonsense, straight-forward personality was so refreshing, and I'll miss our random conversations from qual tips to Japanese horror films. Nicholas Branch, you were the best roommate I could have asked for in this crazy, final year – you helped keep me sane, fed, and entertained. Thank you for the cathartic venting sessions, for being a willing springboard for ideas, for all the 2-o'clock Chick-fil-A runs, and for introducing me to *Legend of Zelda: Breath of the Wild*. Sara Miller and David Gomez – good luck as you continue through your journey!

My way through graduate school was primarily funded by a National Science Foundation fellowship and was supported by scholarships from the Coca-Cola Foundation, Achievement Rewards for College Scientists (ARCS) Foundation, American Institute of Aeronautics and Astronautics (AIAA), Society of Women Engineers (SWE), and the Georgia Institute of Technology President's Fellowship. The actual research would not have been possible without support from the Office of Naval Research.

I could not have completed this dissertation without the hard work and dedication of my team: Parker Singletary for working alongside me on this project, through all the ups and downs, Myra Lattimore for tackling whatever task I needed and for being the new high-voltage, resistor-soldering expert, Robert Ashcom for all the CAD and electrode work, Divya Sunkara for MATLAB coding and Langmuir probe assembly, and Cole Blaney for your invaluable help in all parts of my research, including analyzing thousands on thousands of spectra in the final few weeks.

Outside of HPEPL, Dan Fries from the Combustion Lab provided laser and optics support in characterizing the PI-MAX. Viktoriya Golovkina and Igor Golovkin from PrismSPECT, Jonathan Malenfant, Bill Fischer, Sabbir Liakat, and Sebastian Remi from Princeton Instruments, and Jim Prager, Chris Bowman, and Alex Henson from Eagle Harbor Technologies answered all my questions regarding their software/hardware and helped me troubleshoot.

A strong support network was crucial for me, and I was lucky to have several great

groups of people behind me. Hanna Ek, Nathan Prestridge, and Matthew Sirignano – you were the first people I met at Georgia Tech, and I am so appreciative of the adventures we have had together, from study sessions in Guggenheim (or the CRC!) to post-final celebrations at Dad’s Garage. And of course, “today’s going to be a good day...because why shouldn’t it be?” Joanna So and Amy Ishiguro, your Skype calls and beautiful flower arrangements never failed to cheer me up, and I am looking forward to our next girls’ night! To the Miss Align crew (Jennifer Huang, Stephen Li, Alex Lin, Xander Lin, Felix Sung, Allison Xie, and Linda Xu), thank you for the Pinturillo, Don’t Starve Together, and Ibb and Obb marathons and for reminding me that there is a world beyond my academic bubble!

Finally, ballroom dance was instrumental in keeping me sane through my Ph.D., so to my coaches, Sergiy Samchynskyy and Yuliya Besarab, thank you for pushing me to dance at the highest level and for teaching me not just about dance but also about life. To Daniel Boman, Lana Hanlon, Kaley Hart, Kelsey Johnson, Max-Daniel Sokollek, and Alexander Sun – you helped me destress with movie nights, game nights, and food nights, you sympathized when research was going poorly and celebrated when it was, you were always up for a Sweet Hut or Bookhouse trip, and you kept me motivated and focused, especially in the last few weeks of writing. To Matthew Boguslawski, my biggest thank you for being my partner and for encouraging me every step of the way, in dance and in research. You have impacted me positively in so many ways. Thank you for practicing with me – even when I was going crazy with work – for joining me on late-night food runs and mid-day smoothie runs, and for reaching our goal of winning a national championship!

## TABLE OF CONTENTS

<b>Acknowledgments</b> . . . . .	v
<b>List of Tables</b> . . . . .	xiv
<b>List of Figures</b> . . . . .	xv
<b>Nomenclature</b> . . . . .	xxi
<b>Summary</b> . . . . .	xxv
<b>Chapter 1: Introduction</b> . . . . .	1
1.1 Plasma Overview . . . . .	1
1.1.1 Plasma Generation . . . . .	4
1.1.2 Pulsed Plasma . . . . .	6
1.2 Antenna Overview . . . . .	8
1.2.1 VLF Waves . . . . .	9
1.3 Plasma Antennas . . . . .	13
1.3.1 Multi-Cell Plasma Antenna . . . . .	16
1.3.2 Plasma Waves . . . . .	17
1.3.3 Plasma Parameters . . . . .	24
1.3.3.1 Plasma Frequency . . . . .	24

1.3.3.2	Plasma Conductivity . . . . .	24
1.3.3.3	Electron Density & Temperature . . . . .	25
1.3.3.4	Plasma Breakdown & Quench Times . . . . .	25
1.4	Research Goals . . . . .	26
1.4.1	Dissertation Overview . . . . .	27
<b>Chapter 2: Experimental Setup</b>	. . . . .	<b>28</b>
2.1	Plasma Cell . . . . .	29
2.1.1	Plasma . . . . .	30
2.1.2	Electrodes . . . . .	31
2.2	Vacuum System . . . . .	32
2.2.1	Mass Flow System . . . . .	33
2.2.2	Pressure Control System . . . . .	34
2.2.2.1	Manual Pressure Control . . . . .	34
2.2.2.2	Automated Pressure Control . . . . .	35
2.3	Power . . . . .	36
<b>Chapter 3: Diagnostics</b>	. . . . .	<b>39</b>
3.1	Steady-State Diagnostics . . . . .	39
3.1.1	Time-Averaged Optical Emission Spectroscopy . . . . .	39
3.1.1.1	Wavelength Calibration . . . . .	40
3.1.1.2	Intensity Calibration . . . . .	41
3.2	Time-Resolved Diagnostics . . . . .	41
3.2.1	PI-MAX ICCD Camera . . . . .	43

3.2.1.1	Gating Characteristics . . . . .	46
3.2.2	Spectrograph . . . . .	47
3.2.2.1	First Light . . . . .	49
3.2.2.2	Wavelength Calibration . . . . .	50
3.2.2.3	Intensity Calibration . . . . .	51
3.2.2.4	Step & Glue . . . . .	51
3.2.3	Photodiode . . . . .	52
3.3	Timing Synchronization . . . . .	53
3.3.1	Pulse Delay Generator . . . . .	53
3.3.2	Nanosecond Pulser . . . . .	54
3.3.2.1	Voltage Measurements . . . . .	55
3.3.2.2	Mitigating Voltage Reflections . . . . .	57
<b>Chapter 4: Spectral Analysis . . . . .</b>		<b>60</b>
4.1	Equilibrium Plasma Models . . . . .	60
4.1.1	Complete Thermodynamic Equilibrium . . . . .	61
4.1.2	Local Thermodynamic Equilibrium . . . . .	61
4.1.2.1	Validity Conditions . . . . .	62
4.1.3	Coronal Approximation . . . . .	63
4.2	Collisional-Radiative Model . . . . .	64
4.3	Spectral Line Fits . . . . .	65
4.4	Line Ratio Analysis . . . . .	67
4.5	PrismSPECT . . . . .	68

<b>Chapter 5: Time-Averaged Plasma Discharge</b> . . . . .	70
5.1 Steady-State Plasma Discharge . . . . .	70
5.1.1 OES Analysis Overview . . . . .	71
5.1.1.1 Experimental Intensities . . . . .	72
5.1.2 PrismSPECT Simulations . . . . .	73
5.1.3 Line Ratio Comparison . . . . .	74
5.2 Pulsed-Plasma Discharge . . . . .	78
5.2.1 OES Analysis Overview . . . . .	79
5.2.2 Line Ratio Comparison . . . . .	80
 <b>Chapter 6: Nanosecond-Pulsed Plasma Discharge</b> . . . . .	 83
6.1 Experimental Parameters . . . . .	83
6.2 Experimental Overview . . . . .	84
6.2.1 Optical Setup . . . . .	84
6.2.2 Test Matrix . . . . .	86
6.2.3 NSP Voltage Waveforms . . . . .	88
6.3 OES Analysis Overview . . . . .	90
6.3.1 Process Diagram . . . . .	92
6.4 Results . . . . .	94
6.4.1 Line Ratio Comparison . . . . .	95
6.5 Time-Resolved Nanosecond Pulsed Plasma . . . . .	100
6.5.1 Effects on Electron Temperature . . . . .	101
6.5.2 Effects on Electron Density . . . . .	109

6.5.3	Effects on Plasma Frequency . . . . .	110
6.5.4	Ionization & Recombination Times . . . . .	111
6.5.5	Uncertainty Analysis . . . . .	111
<b>Chapter 7: Conclusions &amp; Future Work . . . . .</b>		<b>116</b>
<b>Appendix A: Acton SP-308 Calibration . . . . .</b>		<b>119</b>
<b>Appendix B: Experimental Procedure . . . . .</b>		<b>122</b>
<b>Appendix C: Data Processing . . . . .</b>		<b>131</b>
<b>Appendix D: PI-MAX Troubleshooting . . . . .</b>		<b>134</b>
<b>Appendix E: NSP Troubleshooting . . . . .</b>		<b>137</b>
<b>References . . . . .</b>		<b>144</b>

## LIST OF TABLES

3.1	Wavelength calibration parameters used for the SP-308 spectrometer during nanosecond-pulsed plasma testing. . . . .	51
5.1	Summary of the three main test groups. . . . .	70
5.2	Selected argon emission spectral lines for line ratio calculations of steady-state plasma [32]. . . . .	72
5.3	Summary of time-averaged electron temperature and electron density measurements for different pulsed plasma conditions using OES line ratio calculations. . . . .	82
6.1	Range of values tested for experimental parameters. . . . .	83
6.2	Complete nanosecond-pulsed plasma test matrix. . . . .	87
6.3	Voltage waveform properties for nanosecond pulsed plasma generation. . . . .	89
6.4	Selected argon neutral spectral lines for line ratio calculations of nanosecond pulsed plasma. . . . .	91
6.5	Selected argon ion +1 emission spectral lines for line ratio calculations of nanosecond pulsed plasma. . . . .	91

## LIST OF FIGURES

1.1	Debye shielding around a point-charge $+Q$ from electron attraction and ion repulsion in the Debye length. . . . .	2
1.2	Types of laboratory and natural plasmas over a range of electron number densities and temperatures [1]. . . . .	5
1.3	I-V curves for four distinct DC gas discharge regimes [2]. . . . .	6
1.4	Example Paschen curves for various gases [2]. . . . .	7
1.5	Basic operation of a traditional antenna. . . . .	9
1.6	U.S. Naval radio tower array using top-hat loading in Cutler, Maine; modified from [21]. . . . .	10
1.7	A monopole whip antenna (left) and a top-hat loaded antenna (right) with a partial representation of current distribution in the antennas; modified from [13]. . . . .	11
1.8	Early plasma antenna by Alexeff and Anderson [25]. . . . .	14
1.9	Demonstration plasma antenna by Alexeff and Anderson [26]. . . . .	14
1.10	30-cm-long plasma column antenna by Kumar and Bora [28]. . . . .	15
1.11	Array of five antenna elements in a 25-cm-long plasma column by Kumar and Bora [29]. . . . .	15
1.12	Diagram of proposed plasma antenna solution with signal input on the left and the plasma cells on the right [13]. . . . .	16
1.13	Propagation of an example modulated signal through 20 plasma cells switching on and off. . . . .	18

1.14	Plasma behaves as a conductor when the traveling wave frequency is less than the plasma frequency ( $\omega < \omega_{pe}$ ), resulting in the wave being damped in the plasma. Plasma behaves as a dielectric when $\omega > \omega_{pe}$ , and the wave propagates through the plasma. . . . .	23
2.1	Experimental setup with plasma cell, electrodes, and vacuum system. . . . .	29
2.2	Glass plasma tube with ISO-type flanges, modified from [31]. . . . .	30
2.3	Rivet electrodes in its Macor housing. . . . .	32
2.4	Serrated electrodes in its Macor housing. . . . .	32
2.5	Needle electrode & supporting threaded rod. . . . .	32
2.6	Flow schematic for argon flow into the plasma cell. . . . .	33
2.7	Conversion from desired argon gas pressure to displayed nitrogen gas pressure on the Lesker pressure controller. Fit line from a 2nd order polynomial fit with $R^2 = 0.99$ . . . . .	34
2.8	Automated pressure control system with KJLC, Arduino board, and low-pass filter holding pressure at 1-Torr argon (1.79-Torr nitrogen). . . . .	36
2.9	Available operating parameter space for the NSP-120-20F at different load types [36]. . . . .	38
3.1	HR4000 spectrometer with components: 1. SMA Connector; 2. slit; 3. filter; 4. collimating mirror; 5. grating; 6. focusing mirror; 7. L2 detector collection lens; 8. CCD detector [37]. . . . .	40
3.2	Major components of the intensifier-CCD, pulled from PI-MAX manual [45].	44
3.3	Spectral response characteristics for PI-MAX photocathode [45]. . . . .	45
3.4	Identifying the fastest PI-MAX gating capabilities by measuring a pulsed laser intensity as a function of gate times. . . . .	46
3.5	Verifying PI-MAX 4-ns gate time by sweeping gated intensity across laser pulse. . . . .	47
3.6	Internal components of the Acton SP-308 spectrograph; pulled from SP-300i manual [47]. . . . .	48

3.7	Schematic of PI-MAX camera connected with Acton SP-300i spectrograph for OES; adapted from PI-MAX manual [45]. . . . .	49
3.8	Uncalibrated HG-1 spectra taken in “spectroscopy” and “imaging” mode with a 600 groove/mm grating centered at 720 nm and an exposure time of 200 ms for first light verification. . . . .	50
3.9	Timing synchronization setup for PI-MAX camera, spectrometer, nanosecond pulser, and photodiode. . . . .	54
3.10	Representative timing relationship of delay generator, pulser, and PI-MAX-SP-308 assembly. . . . .	55
3.11	Electrical schematic of voltage divider for measuring NSP waveform, adapted from [50]. . . . .	56
3.12	Experimental setup of the resistive voltage divider and high-voltage differential probe. . . . .	56
3.13	Evolution of measured NSP voltage waveforms by implementing ringing and voltage reflection mitigation strategies. . . . .	59
4.1	Comparison of a normalized Gaussian and Lorentzian profile with equal FWHM = 2 and a Voigt profile from the convolution of the Gaussian and Lorentzian, pulled from [51]. . . . .	66
5.1	DC argon plasmas at two different operating conditions. . . . .	71
5.2	Argon emission spectra at 450 V, 1 Torr. . . . .	72
5.3	Separate peaks (of mostly Ar II lines) shown in a sample argon test spectra from 300-550 nm. . . . .	73
5.4	Finding best Gaussian fits to data (from a double Gaussian MATLAB fit) by comparing Gaussian center to NIST Ar I and Ar II emission wavelengths. . . . .	74
5.5	Simulated argon emission spectra from PrismSPECT for two different electron temperature plasmas at 1 Torr. . . . .	75
5.6	Evolution of argon neutral and ion population with electron temperature in PrismSPECT at 1 Torr. . . . .	76

5.7	Plasma electron density as a function of electron temperature in PrismSPECT at 1 Torr. . . . .	76
5.8	PrismSPECT simulated emission line intensity and line ratio as a function of electron temperature at 1 Torr. . . . .	77
5.9	Line ratio comparisons between steady-state experimental data and PrismSPECT simulations to calculate electron temperature. . . . .	78
5.10	Pulsed argon plasma discharge “column” across two electrodes 1 cm apart at two pulse repetition frequencies. . . . .	79
5.11	Pulsed argon emission spectra at 1000 V, 5 ns, 10 kHz and taken at 300-ms integration time. . . . .	80
5.12	Line ratio comparisons between pulsed experimental data and PrismSPECT simulations to calculate electron temperature. . . . .	81
6.1	Complete experimental setup with all diagnostics and time-synchronization equipment. . . . .	84
6.2	Example ROI with a 60 pixel bin height. . . . .	85
6.3	Measured voltage waveform, photodiode, and 4-ns camera gate monitoring signal over 34 gates with their respective averaged values. . . . .	87
6.4	Comparison of low-voltage and high-voltage pulses on the NSP. . . . .	90
6.5	Diagram of full process, from data collection to time-resolved $T_e$ and $n_e$ measurements. . . . .	94
6.6	Pictures of nanosecond-pulsed plasma at different pulse frequencies, 10 kV, and 1 Torr. . . . .	96
6.7	Pictures of nanosecond-pulsed plasma at different discharge voltages, 2 kHz, and 1 Torr. . . . .	97
6.8	Pictures of nanosecond-pulsed plasma at different pressure conditions, 20 kV, and 4 kHz. . . . .	97
6.9	Emission spectra of nanosecond pulsed plasma at different operating conditions. Note the trend of increased intensities as discharge voltage and pulse frequency were increased. All spectra shown were taken at the gate time corresponding to maximum voltage pulse. . . . .	99

6.10	Example line ratio comparison (ratios of Ar I 696.53 nm to Ar II lines) of plasma at 16 kV, 1 Torr, 4 kHz at maximum voltage pulse. . . . .	100
6.11	Time-resolved results of pulse frequency study at 1 Torr, 10 kV. . . . .	101
6.12	Time-resolved results of pulse frequency study at 1 Torr, 8 kV. . . . .	102
6.13	Time-resolved results of pulse frequency study at 1 Torr, 14 kV. . . . .	102
6.14	Time-resolved results of voltage study at 1 Torr, 1 kHz. . . . .	103
6.15	Time-resolved results of voltage study at 1 Torr, 2 kHz. . . . .	103
6.16	Time-resolved results of voltage study at 1 Torr, 4 kHz. . . . .	104
6.17	Time-resolved results of pressure study at 10 kV, 1 kHz . . . . .	104
6.18	Time-resolved results of pressure study at 10 kV, 4 kHz . . . . .	105
6.19	Time-resolved results of pressure study at 14 kV, 1 kHz . . . . .	105
6.20	Time-resolved results of pressure study at 14 kV, 4 kHz . . . . .	106
6.21	Time-resolved results of pressure study at 20 kV, 1 kHz . . . . .	106
6.22	Time-resolved results of pressure study at 20 kV, 4 kHz . . . . .	107
6.23	PrismSPECT-simulated population fraction of argon neutrals (Ar I) and ions (Ar II) as a function of electron temperature for a 1-Torr plasma. . . . .	110
6.24	20 individual raw emission spectra at a given delay time and the averaged emission spectra (in black). . . . .	113
6.25	Spread of 20 $T_e$ and $n_e$ values from each emission spectra at a given delay time and test condition (blue markers) and $T_e$ and $n_e$ values and standard deviation from the averaged spectra (solid and dotted red lines). . . . .	114
6.26	Spread of $T_e$ and $n_e$ values from individual line ratios of a given emission spectrum (blue markers) and $T_e$ and $n_e$ values and standard deviation from averaged line ratio (solid and dotted red lines). . . . .	114
C.1	Taking spectra from wavelength calibrations and calculating appropriate wavelength corrections for experimental spectra. . . . .	131

C.2	Taking spectra from intensity calibrations and calculate appropriate intensity corrections for experimental spectra. . . . .	132
C.3	Taking spectra from nanosecond-pulsed plasma, finding strong Ar I and Ar II peaks, and outputting those peaks' wavelengths and intensities. . . . .	132
C.4	Consolidating all peak wavelengths and intensities from a given test. . . . .	132
C.5	Calculating experimental line ratios and comparing them to PrismSPECT-generated line ratios. . . . .	133
D.1	Measured dark spectra with large periodic noise. . . . .	135
D.2	Speckled background of spectrometer causing large periodic noise. . . . .	136

## NOMENCLATURE

$B$	magnetic field
$E_\ell$	longitudinal electric field component
$E_t$	transverse electric field component
$E$	electric field
$j$	current density
$k$	wave propagation vector
$u$	electron velocity
$\epsilon_0$	permittivity of free space
$\gamma_{se}$	secondary electron emission coefficient
$\lambda$	wavelength
$\lambda_D$	Debye length
$\lambda_{De}$	electron Debye length
$\lambda_{Di}$	ion Debye length
$\mu_0$	permeability of free space
$\nu_m$	collision frequency
$\omega$	electromagnetic wave frequency
$\omega_c$	ion cyclotron frequency
$\omega_{pe}$	electron plasma frequency
$\rho$	charge density
$A$	Einstein coefficient
$a_0$	Bohr radius
$B$	magnitude of magnetic field

$c$	speed of light
$d$	gap distance between electrodes
$e$	charge of electron
$E_\infty$	ionization energy of atom
$E_H$	ionization energy of hydrogen
$E_{12}$	ionization energy of atom from ground state to first ionized state
$f_M(\mathbf{v})$	particle velocity distribution function
$h$	Plank's constant
$I$	driving antenna current
$I$	intensity from emission spectral line
$I_0$	peak driving current
$k_B$	Boltzmann's constant
$L$	physical dimension of the plasma
$l$	total length of dipole antenna
$m_e$	mass of electron
$m_i$	mass of ion
$n_e$	electron number density
$n_e^*$	critical electron number density from Griem criterion
$n_i$	ion number density
$n_j$	ion number density of charge state j
$n_n$	neutral number density
$n_{e0}$	initial electron density
$n_{i0}$	initial ion density
$P$	antenna radiating power
$p$	pressure
$Q$	single point charge
$q_i$	charge of ion

$R_{loss}$	loss resistance
$R_{rad}$	radiation resistance
$T_e$	electron temperature
$T_g$	gas temperature
$T_i$	ion temperature
$t_{delay}$	time delay on delay generator
$t_{FWHM}$	full-width at half-max
$t_{gate}$	gate time of ICCD camera
$t_{pulse}$	width of laser pulse
$V$	antenna voltage
$V_0$	peak voltage
$v_g$	group velocity
$V_{bd}$	breakdown voltage
$\nu_{en}$	collision frequency of electron to neutrals
$\nu_{ph}$	phase velocity
$X_A$	imaginary antenna impedance
$Z$	impedance
$Z_i$	ion partition function
$Z_n$	neutral partition function
$Z_{in}$	input impedance
CRM	collisional-radiative model
CTE	complete thermal equilibrium
HF	High Frequency
ICCD	intensified charge-coupled device
LTE	local thermal equilibrium
MFC	mass flow controller
NSP	nanosecond pulser

OES optical emission spectroscopy

SNR signal-to-noise ratio

TDLAS tunable diode laser absorption spectroscopy

VHF Very High Frequency

VLF Very Low Frequency

## SUMMARY

Radio waves below 300 kHz are unwieldy to operate as these antenna arrays span over 5 km<sup>2</sup>. However, these low frequency (LF) and very low frequency (VLF) waves are useful in communication and navigation because of their ability to deeply penetrate the ground and ocean surface. They also help with satellite protection as VLF signals are a key driver in removing energetic charged particles trapped in the Van Allen radiation belts that damage satellite electronics.

Current construction for shorter VLF antennas is efficiency-limited – the signal propagates down the antenna and reflects back faster than the signal period; the reflection thereby interferes with and nearly cancels the outgoing signal. A current solution is a top-hat loaded antenna, which radiates more efficiently but is constrained to a very small bandwidth. A plasma antenna with a series of individually-controlled plasma cells could overcome the bandwidth limitations. Modulating the plasma conductivity in each segment to turn a portion of the antenna on or off may suppress reflected waves in the time-domain by removing the necessary electrically conducting pathway.

For a multi-celled, VLF plasma antenna to be operational, the plasma in the antenna must switch from conductive to non-conductive on the order of nanoseconds and have an accurately-tuned electron density, electron temperature, and plasma frequency. The feasibility of this plasma antenna and the physics of the necessary plasma were investigated by generating nanosecond-pulsed, argon plasma at various pulse frequencies, widths, and pressures. Argon emission lines were analyzed with an ICCD-spectrometer assembly gating at 4 ns, and relative intensities of strong argon neutral and ion lines were used in line-ratio calculations. Experimentally-determined ratios were compared to theoretical ratios generated from PrismSPECT, a collisional-radiative spectral analysis software, to obtain time-resolved electron temperature  $\sim \mathcal{O}(1 \text{ eV})$ , electron number density  $\mathcal{O}(10^{14} - 10^{15} \text{ cm}^{-3})$ , and plasma frequency  $\sim 200 \text{ GHz}$ .

These values were used to discover time-resolved trends over the lifetime of the plasma and extract sets of plasma parameters for the rapid ionization and recombination needed for a successful VLF plasma antenna design. Further investigations into the physics of nanosecond-pulsed plasmas could include analysis of wavelength transitions and processes as well as the effects of electrode geometry and discharge gas on plasma properties. Additional future work needed for a VLF plasma antenna demonstration would entail developing the signal propagation technology needed for transmission through the plasma antenna cell.

# CHAPTER 1

## INTRODUCTION

### 1.1 Plasma Overview

Plasma is commonly known as the fourth state of matter after solid, liquid, and gas. It describes a collection of free electrons and ions that can interact with, as well as create, electromagnetic fields. Plasmas are good electrical conductors and also exhibit wave behavior (to be discussed in further detail in Section 1.3.2). Naturally found in stars and interstellar gases, plasmas are the most common state of matter in the universe. They naturally appear on Earth in the form of lightning, the ionosphere, and auroras but are also found in man-made items such as fluorescent lights.

However, not all collections of charged particles can be characterized as a plasma. The following criteria need to be met:

1. *Debye Shielding:* Assume a point-charge  $+Q$  is placed in a homogeneous plasma that has equal electron and ion densities. Within a Debye length, the  $+Q$  is felt by other charged particles, and their trajectories are altered – electrons are attracted and ions are repelled. A cloud of electrons surrounds the positive point charge; from far away, it appears as if the charges are balanced. The bulk plasma is effectively “shielded” by the collective effects of the plasma particles within a Debye length of the point charge and is not affected by the electrostatic fields that arise from the nonzero potential of the point charge. Figure 1.1 illustrates the trajectory bending of ions and electrons in response to  $+Q$  that leads to Debye shielding.

The Debye length  $\lambda_D$  combines the shielding action of electrons and ions. The two

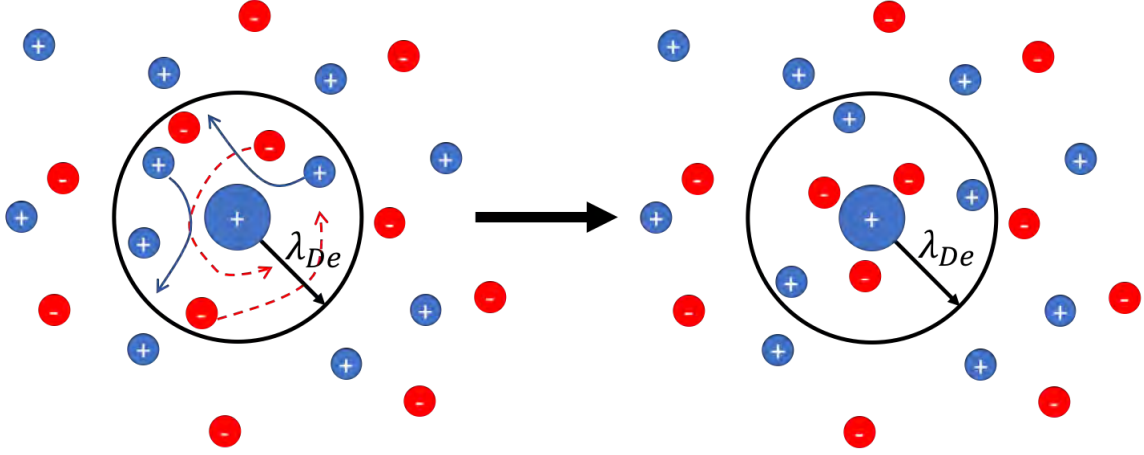


Figure 1.1: Debye shielding around a point-charge  $+Q$  from electron attraction and ion repulsion in the Debye length.

contributions can be separated:

$$\lambda_{De} = \sqrt{\frac{\epsilon_0 k_B T_e}{n_{e0} e^2}} \quad (1.1a)$$

$$\lambda_{Di} = \sqrt{\frac{\epsilon_0 k_B T_i}{n_{i0} e^2}} \quad (1.1b)$$

where  $\lambda_{De}$  is the electron Debye length and  $\lambda_{Di}$  is the ion Debye length.  $\epsilon_0$  is the permittivity of free space,  $k_B$  is Boltzmann's constant,  $T_e$  is electron temperature,  $T_i$  is ion temperature,  $n_{e0}$  and  $n_{i0}$  are respectively the initial electron and ion densities, and  $e$  is the charge of an electron. For gas discharges, typical values are around  $T_e = 10^4$  K and  $n_e = 10^{16} - 10^{18} \text{ m}^{-3}$ , so  $\lambda_{De}$  is usually small,  $\sim 10^{-4}$  m.

For Debye shielding to exist, two more criteria for a plasma must be met:

$$L \gg \lambda_{De} \quad (1.2)$$

$$n_e \lambda_{De}^3 \gg 1 \quad (1.3)$$

Equation 1.2 says that the characteristic physical dimension of the plasma system,  $L$ , is large compared to  $\lambda_{De}$ . Equation 1.3 says that the number of electrons inside a

Debye sphere, a sphere inside the plasma of radius  $\lambda_{De}$ , must be large so the average distance between electrons (approximately  $n_e^{-1/3}$ ) is small compared to  $\lambda_{De}$ .

2. *Macroscopic Neutrality (Quasineutrality)*: For distances greater than the Debye length, the characteristic length scale for plasmas, a plasma is quasineutral and has no net electric charge. With  $n_j$  as the ion number density of charge state  $j$  and  $n_e$  as the electron number density, this criterion can be summarized as:

$$n_e = \sum_j n_j \quad (1.4)$$

3. *Plasma Frequency*: While the Debye length describes the distance across which the plasma feels a perturbation, the plasma frequency describes the time scale in which the plasma will collectively respond to a perturbation. Because of their low mass, electrons will respond more quickly than the heavy ions. Consider a uniform plasma at rest with a sudden charge separation. The electrons will accelerate towards the ions to restore charge neutrality but will overshoot them. The electrons will then accelerate in the opposite direction and thus continue to oscillate in the vicinity of ions. The frequency of this electron oscillation is called the electron plasma frequency:

$$\omega_{pe} = \sqrt{\frac{n_e e^2}{m_e \epsilon_0}} \quad (1.5)$$

where  $m_e$  is the mass of an electron. This leads to the fourth criterion for a plasma:

$$\frac{\omega}{\nu_{en}} > 1 \quad (1.6)$$

where  $\nu_{en}$  represents the frequency with which an electron collides with neutrals. This criterion states that the electron number density must be high enough such that the plasma frequency is larger than the electron-neutral collision frequency.

Figure 1.2 illustrates the wide temperatures, densities, plasma frequencies, and Debye

lengths that different types of plasmas can achieve, from low-temperature, sparse interstellar gases to high-temperature, dense thermonuclear plasma.

### 1.1.1 Plasma Generation

Plasmas are created when the environment is conducive for a large number of atoms to be ionized. Two common methods of generating plasmas are photoionization and electrical discharge in gases [1, 2]. In the photoionization process, an atom absorbs an energetic photon whose energy is at least the ionization potential of the atom. This process is most common in space plasmas or in environments like the Earth's ionosphere where there are a large number of highly energized photons in the ultraviolet, x-ray, or gamma-ray range. In a gas discharge, a power source initiates the electric breakdown in a gas. Free electrons are then accelerated to sufficiently high energies to ionize atoms via collisions in a cascade event. When the power source feeding the plasma is removed or turned off, the ions will recombine with free electrons back into neutrals.

Direct current (DC) gas discharges are generated by applying a high enough voltage difference between two electrodes to spark electric breakdown. In the example shown in Figure 1.3, a discharge voltage of 600 V was applied. Up to discharge currents of 1  $\mu\text{A}$ , the discharge voltage remains close to the breakdown voltage and is independent of the current. As there is no visible glow in the discharge channel, this regime is known as the Townsend dark discharge. As discharge current continues to increase, the gas discharge moves through subnormal glow, normal glow, anomalous glow, and finally the unstable arc discharge where the discharge voltage continues to drop at high currents.

The breakdown voltage for a DC gas discharge as a function of pressure, gas type, and electrode gap distance is characterized by Paschen's law:

$$V_{bd} = \frac{Bpd}{\ln(Apd) - \ln \left[ \ln \left( 1 + \frac{1}{\gamma_{se}} \right) \right]} \quad (1.7)$$

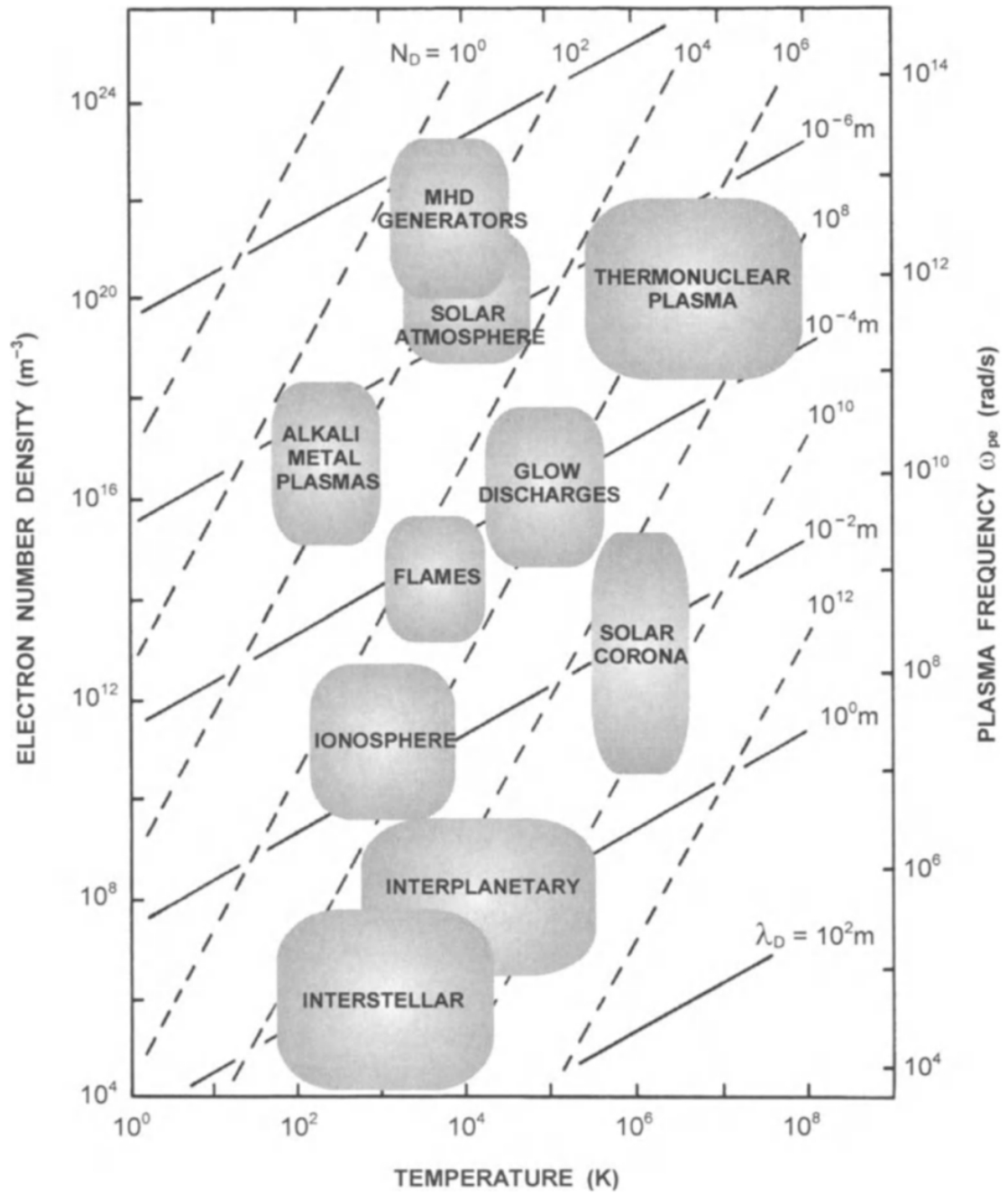


Figure 1.2: Types of laboratory and natural plasmas over a range of electron number densities and temperatures [1].

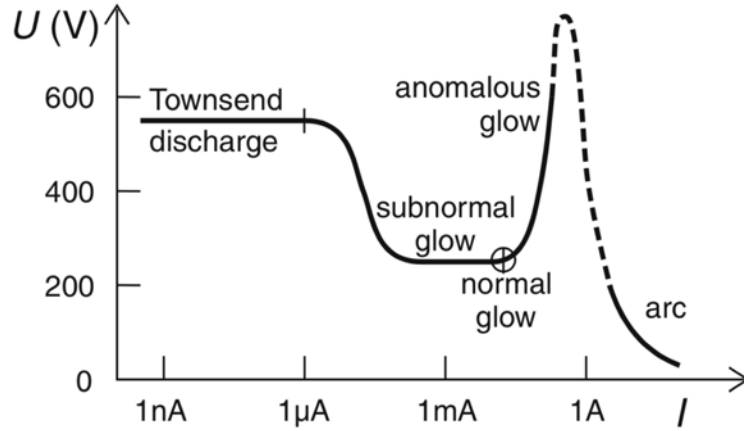


Figure 1.3: I-V curves for four distinct DC gas discharge regimes [2].

where  $p$  is the pressure in pascals,  $d$  is the gap distance in meters,  $\gamma_{se}$  is the secondary electron emission coefficient, and  $A$  and  $B$  are empirically-determined constants for a given gas. Therefore, gas selection is critical for characterizing breakdown voltage. Figure 1.4 depicts the typical Paschen curve for various gases. For a given gas, there is a minimum breakdown voltage. Left of the minimum, there are too few atoms for effective ionization; right of the minimum, electrons have insufficient time between collisions to acquire enough energy to overcome the ionization potential. In both cases, a higher voltage is thus necessary to initiate a DC glow discharge.

### 1.1.2 Pulsed Plasma

Similar to steady plasma generation, pulsed-plasma discharges can be created with a pulsed voltage source. There has been renewed interest recently in nanosecond pulsed plasma discharges in enhancing and stabilizing combustion (i.e., by shortening ignition delay times, extending extinction limits, improving flame stabilization, increasing flame speed, and suppressing soot formation) [3, 4], biochemical decontamination by removing harmful gases via plasma [4, 5], and material processing and surface treatment applications such as depositing, etching, and coating [5–7].

Nanosecond-pulsed discharges can be used to effectively produce a stable plasma with

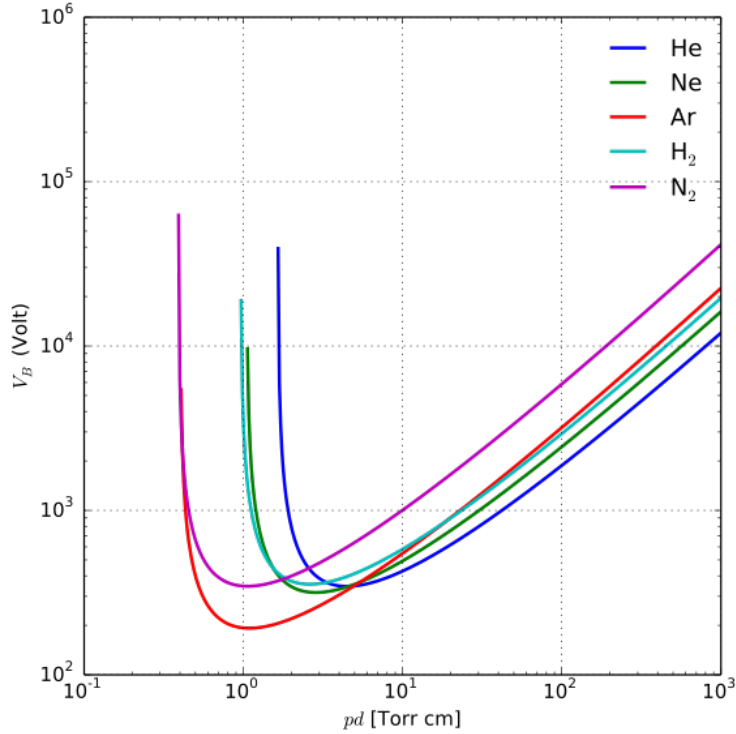


Figure 1.4: Example Paschen curves for various gases [2].

a high concentration of metastable species, ions, and high-energy electrons [3, 7], and pulsed discharges require less input power – up to 250 times lower – than steady discharges to produce a plasma with the same electron density [5]. These types of plasma also provide more flexibility than steady plasmas because it is possible to control plasma parameters such as electron temperature, electron number density, and plasma conductivity (parameters discussed in more detail in Section 1.3.3) by changing the characteristics of the input voltage pulses.

However, there are limited references in literature that experimentally investigate the plasma dynamics of nanosecond-pulsed plasmas. Alami et al. used cylindrical and flat Langmuir probes and a triple probe to measure electron densities and electron temperatures in a high-power, pulsed magnetron discharge with microsecond resolution. Peak electron densities of  $10^{19} \text{ m}^{-3}$  were measured by applying high-power pulses (0.5 MW) with a pulse width of  $100 \mu\text{s}$  and a repetition rate of 20 ms, and it was observed that electron temperature was initially very high in the plasma but rapidly decreased when

the pulse turned off [8]. Laimer et al. investigated what type of voltages pulses would provide the most temporally and spatially uniform plasma. Through visual observations, it was concluded that a bipolar pulsed power supply capable of providing both positive and negative pulses would be the best option and would cause a small increase in the conductivity of the plasma at the beginning of each negative pulse [9].

Liu et al. created a more complete model of pulsed plasma dynamics that investigated the effects various discharge parameters had on the plasma characteristics of a pulsed, RF-capacitive argon glow discharge [10]. While electron temperature and total ionization rate dropped during the voltage switch off period, the electron density was higher. If the applied voltage or distance between electrodes was increased, the plasma potential, electron temperature, and electric field increased, but the opposite trend held true if modulation frequency or duty cycle for the pulser was increased.

## **1.2 Antenna Overview**

First built in 1888 by Heinrich Hertz to prove the existence of electromagnetic waves, antennas are electrical conductors of a specific length that radiate and receive radio waves propagating through space by converting electromagnetic radiation into electric currents or vice versa [11, 12]. As seen in Figure 1.5, an oscillating current is supplied and fed into the transmitting antenna during transmission. This creates an oscillating electric and magnetic field around the antenna and radiates energy away from the antenna as a moving electromagnetic (radio) wave. During reception, the time-varying electric and magnetic fields of the incoming radio wave exert a force on the electrons in the receiver antenna, which causes them to shift. This movement of electrons produces the oscillating current in the antenna that is then read by the receiver.

The design of an antenna can be modified to suit the application (i.e., omnidirectional or directed radiation, the frequency of radio waves, etc.), but there are three main tradeoffs for any antenna design: high bandwidth, small antenna size, and good efficiency. These

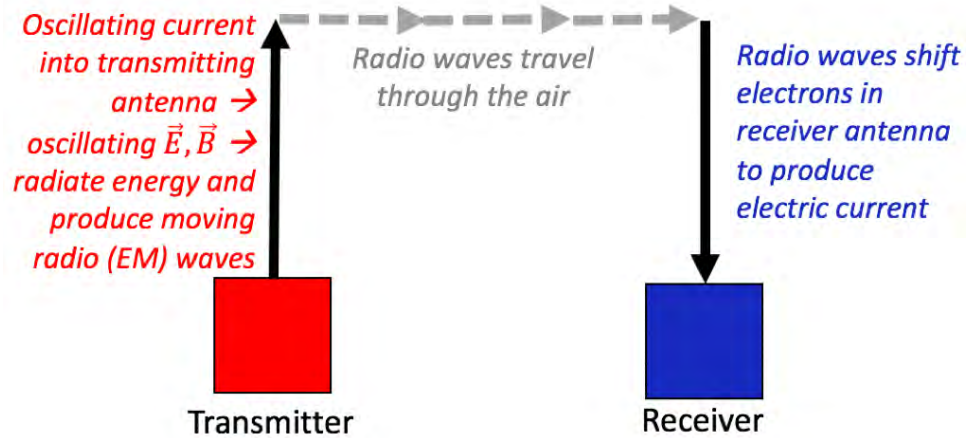


Figure 1.5: Basic operation of a traditional antenna.

tradeoffs are further described below.

### 1.2.1 VLF Waves

Very Low Frequency (VLF) radio waves (3-30 kHz) have long wavelengths (10-100 km long). As a result, VLF waves are not hindered by large ground obstacles and can penetrate 10s of meters deep into seawater. They are mostly reflected 70 km and above in the Earth's ionosphere and can therefore be guided in the Earth-ionosphere waveguide to global distances [13, 14]. For example, low-frequency radio signals generated by lightning strikes can be received by receivers around the world.

Therefore, VLF is still important for submarine communications, underground imaging and detection, global communications, and navigation [15, 16]. They can be used to track outages in satellite-to-ground communications by monitoring the ever-changing ionosphere, through which all satellite-ground signals must pass [17]. VLF waves also help with radiation belt remediation and satellite protection. VLF signals from lightning strikes are a key driver in the removal of energetic charged particles trapped in the Van Allen radiation belts that can severely damage satellite electronics [18, 19].

Unfortunately, one of the biggest problems with VLF antennas is that their kilometers-long wavelengths necessitate an enormous physical platform, greater than

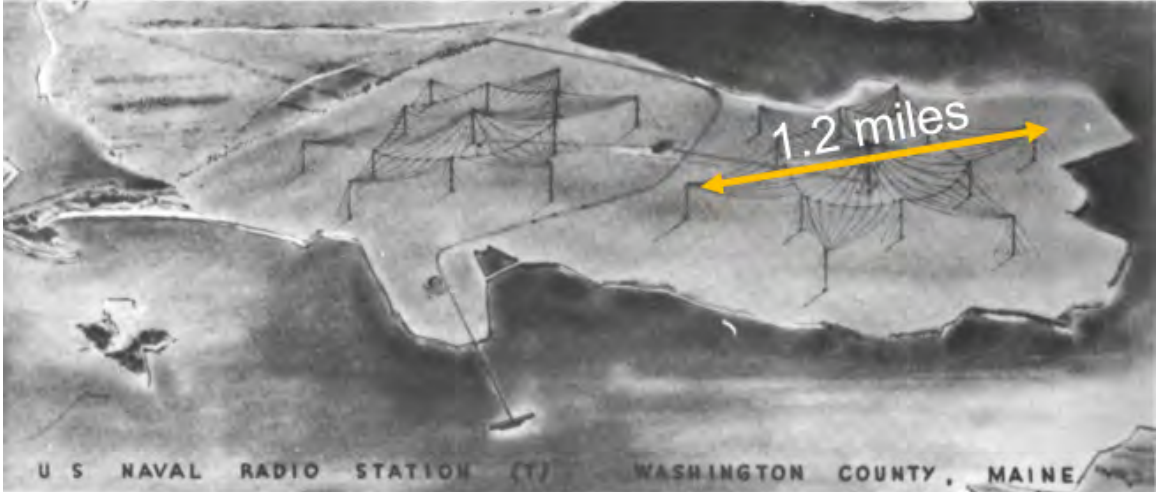


Figure 1.6: U.S. Naval radio tower array using top-hat loading in Cutler, Maine; modified from [21].

5 km<sup>2</sup>, to efficiently transmit and receive VLF waves. For example, Figure 1.6 shows a 2-MW U.S. Navy VLF transmitter site in Cutler, Maine that transmits at 24 kHz to submerged submarines. The array covers almost 3000 acres or 4.69 square miles [20].

VLF facilities cannot be easily moved due to their size, yet traditional VLF antennas also cannot be made shorter. One of the simplest antennas is a dipole antenna constructed of two separated, co-linear conductors with a driving current of  $I(t) = I_0 \cos(\omega t)$  where  $I_0$  is the peak driving current. Assuming current in the dipole antenna drops linearly from the center to zero at the ends, the formula for time-averaged radiated power from an electrically short dipole ( $l < \lambda/4$ ) is as follows [12]:

$$\langle P \rangle = \frac{\pi^2}{3c} \left( \frac{I_0 l}{\lambda} \right)^2 \quad (1.8)$$

where  $c$  is the speed of light,  $l$  is the total length of the dipole, and  $\lambda$  is the wavelength. This states that the smaller an antenna is compared to its wavelength, the less power it can broadcast.

Shorter antennas also suffer from inefficiencies due to voltage reflections. The end of a short monopole whip antenna, as seen in Figure 1.7, is an open circuit. A voltage pulse

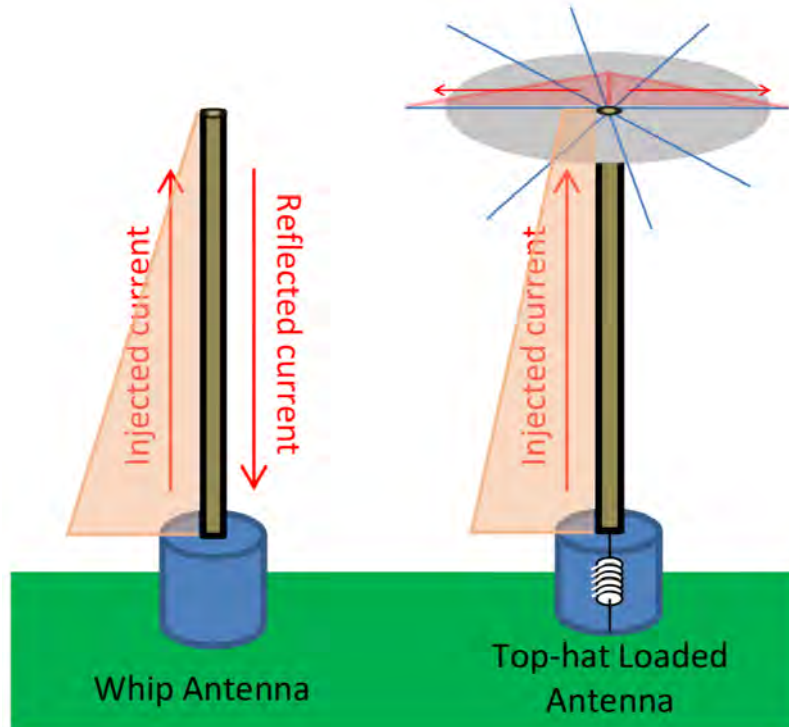


Figure 1.7: A monopole whip antenna (left) and a top-hat loaded antenna (right) with a partial representation of current distribution in the antennas; modified from [13].

sent down the antenna towards the tip will reflect with a +1 coefficient, and the current will reflect with a -1 coefficient. If the length of the antenna is much smaller than the wavelength ( $d \ll \lambda$ ), the reflected current almost exactly cancels with the injected current [13]. For a given antenna length, an enormous amount of voltage is needed for little current to be transmitted along the antenna; from Equation 1.8, very little power is radiated. This is a major limitation for conventional, electrically-short antennas.

The current method to mitigate this efficiency constraint for VLF antennas is to use a top-hat loaded antenna instead of a whip monopole or a quarter-wave dipole [11, 13, 21]. Top-hat loading involves setting long wires or a metal structure at the top of the antenna to build up a capacitance between the end of the antenna and the ground. The horizontal wires radiate little power but add capacitance to the end of the antenna, which increases the current at the end of the vertical conductor (see Figure 1.7). The antenna can radiate more power or is more sensitive to incoming signals and is thus more efficient.

Another way to analyze the benefits of top-hat loading is to consider the input impedance of an antenna, which relates the voltage to the injected current of the antenna:

$$V(t) = V_0 \cos(\omega t) = I(t) \|Z\| \quad (1.9)$$

$$I(t) = \frac{V(t)}{\|Z\|} \quad (1.10)$$

where  $Z$  is the impedance. The lower the input impedance for a given voltage sinusoid, the larger the current. Input impedance can be broken into its components by:

$$Z_{in} = R_{rad} + R_{loss} + jX_A \quad (1.11)$$

where  $R_{rad}$  is the radiation resistance that can be thought of as the radiation across some imaginary resistor when a voltage  $V$  is sent across the antenna,  $R_{loss}$  is the loss resistance from imperfections in the metal conductor, and  $X_A$  is the imaginary antenna impedance [13]. The structure at the tip of the antenna lowers the antenna impedance enough such that it becomes a negative imaginary term (i.e., the voltage signal lags the current signal by  $90^\circ$ ). An inductor, which has a positive imaginary impedance (i.e., the voltage signal leads the current signal by  $90^\circ$ ), is placed at the base of the antenna. Thus, the third term entirely cancels out for a top-hat loaded antenna.  $Z_{in}$  is now smaller, so per Equations 1.10 and 1.8, the top-hat antenna can radiate more efficiently. Unfortunately, antenna input impedance changes rapidly with frequency, so top-hat loaded antennas only work in narrow frequency bands of 100-200 Hz [21]. Existing VLF antennas that can efficiently transmit are therefore bandwidth-limited, and top-hat loaded antennas (like the Cutler, Maine VLF installation) are still enormous in physical size.

The major efficiency versus bandwidth tradeoff that still has not been overcome in conventional antennas operating in the VLF range is summarized as follows:

1. An antenna utilizes top-hat matching and achieves 2-4 times greater efficiency but

can only operate in a narrow (100-200 Hz) bandwidth [21].

2. An antenna has no bandwidth constraint but has poor efficiency as halving the frequency for a given antenna geometry drops the radiated power by 16 times [13].
3. For either configuration, the antennas are still incredibly large in physical size.

### **1.3 Plasma Antennas**

A proposed solution to build a VLF antenna with both high efficiency and bandwidth is to block the reflected waves at all frequencies by building a plasma antenna. A plasma antenna uses ionized gases in a glass tube as the conducting medium instead of solid metal wires as in a traditional antenna. When the low-pressure gas in the tube is ionized, the charged particles behave like the metal conductors of a traditional antenna and allow radio waves to be transmitted or received. When there is no ionizing voltage applied to the tube, the plasma returns to its charge-neutral gaseous state and becomes non-conductive. Therefore, rapidly turning a plasma antenna on and off can block the reflected waves (further explained in Section 1.3.1).

Experiments over the past two decades have successfully demonstrated the use of a plasma antenna. Borg et al. showed that plasma column antennas are efficient enough (i.e., 25% – 50% efficient) and generate low enough noise (i.e., similar noise spectra between metal and surface wave driven plasma antennas with a maximum noise difference of 4 dB) to be used in narrowband high-frequency (HF) (3-30 MHz) and very high-frequency (VHF) (30-300 MHz) communications [22, 23]. Rayner et al. showed that the proportional relationship among the length of a column, the applied RF power, and the linear conductivity along the column should make it possible to design an antenna with an electrically-controllable length that would allow for rapid reconfiguration for different transmission frequencies just by changing the plasma characteristics [24].

Alexeff and Anderson made significant contributions in theoretical and experimental

plasma antenna work [25–27]. Using fluorescent and neon tubes to create their plasma antennas (Figures 1.8 and 1.9), Alexeff and Anderson demonstrated the wide operational transmission and reception frequency range of plasma antennas from 500 MHz to 20 GHz. They also discovered that by ionizing the gas tubes with a series of short DC pulses, they could produce plasma in  $2 \mu\text{s}$ . The plasma took about 1 ms to turn off. Pulsing the plasma with DC bursts also produced a higher plasma density ( $4 \times 10^{10} \text{ cm}^{-3}$ ) compared to steady-state DC discharges ( $6.4 \times 10^9 \text{ cm}^{-3}$ ). Their experiments suggested that the antenna efficiency and noise level of the plasma antenna were comparable to their metal analog as long as the plasma density is sufficiently high – the plasma frequency should be at least an order of magnitude greater than the desired radio frequency – and the coupling to the plasma is optimized [25]. Alexeff and Anderson also proposed a more versatile plasma antenna by having an array of small plasma elements. Turning select elements off by returning the gas tube to its non-conductive, gaseous state could reconfigure the plasma antenna and open different transmitting windows.

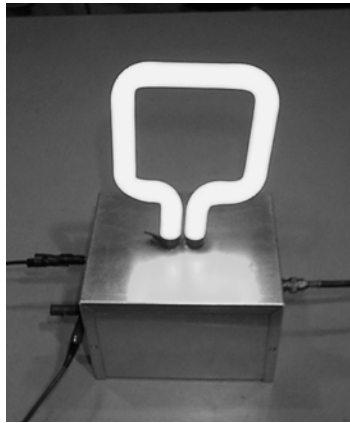


Figure 1.8: Early plasma antenna by Alexeff and Anderson [25].



Figure 1.9: Demonstration plasma antenna by Alexeff and Anderson [26].

Kumar and Bora further investigated the reconfigurability of plasma antennas by changing operating parameters such as working pressure, input power, and glass type [28, 29]. As seen in Figures 1.10 and 1.11, they were able to transform a single plasma antenna column into multiple stationary plasma striations or “plasma blobs,” where each striation

acts as an antenna element. One array of a plasma antenna can, therefore, operate like several different antennas.



Figure 1.10: 30-cm-long plasma column antenna by Kumar and Bora [28].

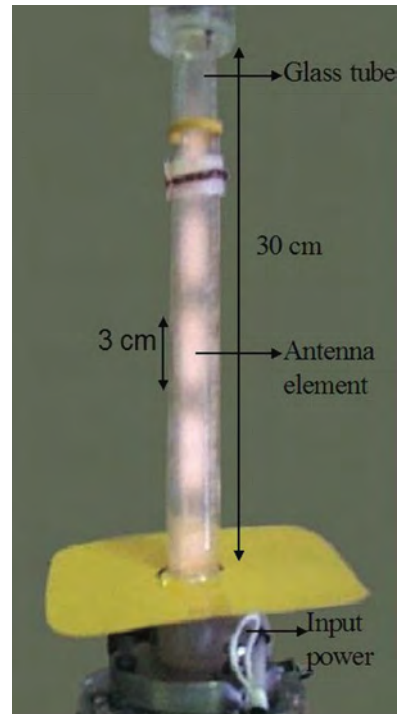


Figure 1.11: Array of five antenna elements in a 25-cm-long plasma column by Kumar and Bora [29].

Compared to conventional metal antennas, plasma antennas have the following advantages [13, 22–29]:

1. *Stealth*: Unlike a metal antenna, a plasma antenna that is turned off will not reflect radar signals. The gas only needs to be ionized when transmitting or receiving, so a plasma antenna can immediately be turned off after sending or receiving a pulse. The now dielectric tube has a small radar-scattering cross-section and is effectively radar invisible. Even when a plasma antenna is operating, it will still be invisible to high-frequency radar that is far above the antenna's plasma frequency.
2. *Ringling Mitigation*: Ringing after pulse excitation is very common for metal antenna

designs. Immediately deionizing the plasma antenna after a signal pulse minimizes signal corruption and degradation brought by antenna ringing.

3. *Reconfigurability & Versatility:* A single plasma antenna array can be rapidly reconfigured into multiple antennas with different frequencies, bandwidths, and effective lengths by changing operating parameters. This allows for compact communication systems on ships or submarines where several different transmitting frequencies may be necessary.
4. *Size & Weight:* Plasma antennas can be smaller in size and lower in weight than metal antennas, especially in the low-frequency radio range.

### 1.3.1 Multi-Cell Plasma Antenna

The efficiency and size problem of VLF antennas can be solved by creating a plasma antenna with a series of individually controllable segments. The conductivity in each plasma cell can be turned on and off via the electrodes in each segment to allow or block VLF signals respectively. Figure 1.12 illustrates the proposed process.

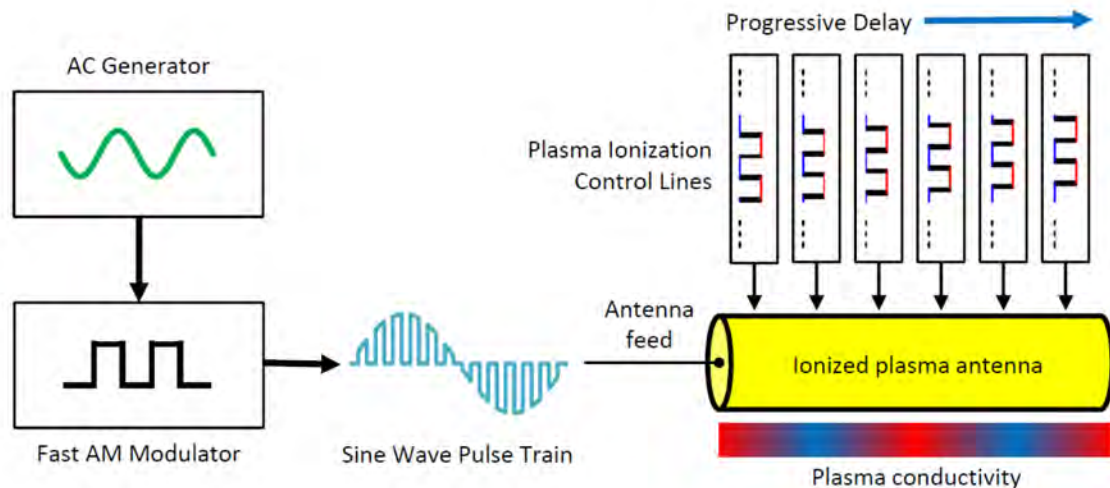


Figure 1.12: Diagram of proposed plasma antenna solution with signal input on the left and the plasma cells on the right [13].

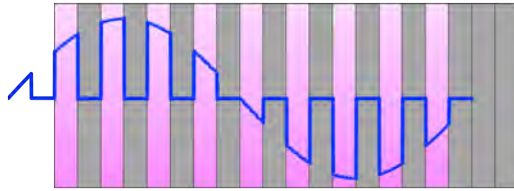
The low-frequency signal that needs to be transmitted is first subjected to high-frequency amplitude modulation and divided into a series of short pulses. This modulated signal is fed into the plasma antenna. The pulses will propagate down the antenna and reflect at the end. However, before the reflection can take place, the plasma at the end segment will turn off. Without a conducting path, the reflected signal will dissipate, thus eliminating the efficiency problem caused by signal reflections for short, traditional metal antennas. Figure 1.13 shows how the conductivity of 20 plasma cells is switched on and off to allow a modulated signal through the plasma antenna and to block the reflected signal.

Unlike top-hat loading, this segmented plasma antenna blocks reflections in the time domain instead of the frequency domain, so it is not bandwidth limited. Theoretically, the plasma antenna can match across the entire spectrum and can operate at any frequency. It is also much more portable than a whip or top-hat loaded antenna for VLF signals. As frequency decreases and an electrically short antenna becomes shorter compared to the wavelength, the current along the plasma antenna will stay approximately constant due to its reflection-blocking attribute [13]. Based on simulations, a 15-meter-long plasma antenna produces  $\sim 30$  times more current than a whip antenna at 30 kHz. From Equation 1.8, such a plasma antenna would produce  $\sim 900$  times more power than a whip with the same input.

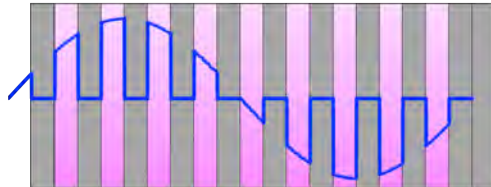
### 1.3.2 Plasma Waves

One of the underlying principles for a segmented plasma antenna is that the plasma can interact with the VLF wave as both a conductive and dielectric medium. This subsection investigates the concept of plasma waves in more detail and highlights why plasma frequency of the plasma antenna is a critical operating parameter.

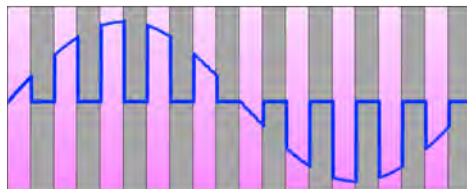
Each individual plasma cell of the antenna will generate an unmagnetized, isotropic cold plasma. Cold plasma is one in which the thermal kinetic energy of the ions and



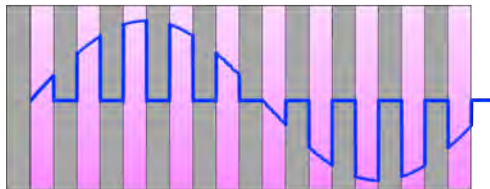
(a) Modulated signal through plasma antenna.



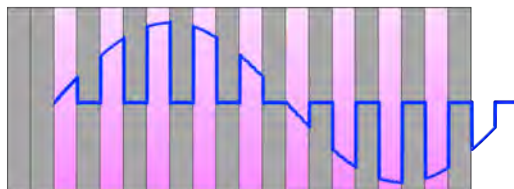
(b) Signal propagating; last cells still turned off.



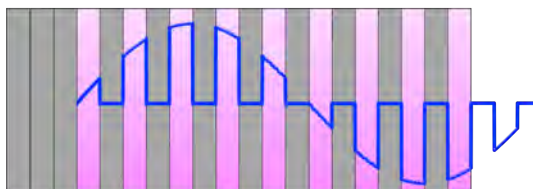
(c) Signal fully in plasma antenna.



(d) First cell turned off since signal completely past.



(e) Last cell turned off to block reflected signal.



(f) First cells turned off.

Figure 1.13: Propagation of an example modulated signal through 20 plasma cells switching on and off.

neutrals is low compared to that of the electrons. Therefore, the thermal kinetic energy of the heavy species can be ignored. Assuming that high-frequency waves, whose frequencies  $\omega$  are large compared to the ion cyclotron frequency  $\omega_c$ , will be propagating through the plasma medium, only electron motion will be considered.  $\omega_c$  is the frequency of the ion's spiraling, circular motion due to a magnetic field  $B$ :

$$\omega_c = \frac{|q_i|B}{m_i} \quad (1.12)$$

where  $q$  is the charge of the ion and  $m_i$  is the mass of the ion. Plasma waves in a cold electron gas satisfy the continuity equation, the equation of motion for electrons, and Maxwell's equations:

$$m_e \frac{D\mathbf{u}}{Dt} = q(\mathbf{E} + \mathbf{u} \times \mathbf{B}) - m_e \nu_m \mathbf{u} \quad (1.13)$$

where  $\nu_m$  is the collision frequency, the frequency that an electron will collide with another plasma particle, and  $\mathbf{u}$  is the electron velocity.

$$\frac{\partial n_e}{\partial t} + \nabla \cdot (n_e \mathbf{u}) = 0 \quad (1.14)$$

$$\nabla \cdot \mathbf{E} = \frac{\rho}{\epsilon_0} \quad (1.15)$$

$$\nabla \cdot \mathbf{B} = 0 \quad (1.16)$$

$$\nabla \times \mathbf{E} = -\frac{\partial \mathbf{B}}{\partial t} \quad (1.17)$$

$$\nabla \times \mathbf{B} = \mu_0 \left( \mathbf{j} + \epsilon_0 \frac{\partial \mathbf{E}}{\partial t} \right) \quad (1.18)$$

where  $\epsilon_0$  and  $\mu_0$  are the vacuum permittivity and permeability,  $\rho$  is the charge density and  $\mathbf{j}$  is the current density, and  $\mathbf{E}$  is electric field and  $\mathbf{B}$  is magnetic field.

Considering only one type of positive ion with charge  $q_i$  and ion number density  $n_i$ , the total electric charge density for an unmagnetized, cold plasma is:

$$\rho = -en + q_i n_i \quad (1.19)$$

Coupling with the continuity equation and  $v_i = 0$  (no ion motion considered), the electric current density is

$$\mathbf{j} = -en\mathbf{v} \quad (1.20)$$

The harmonic plane wave solutions can be written as

$$\psi_j(\mathbf{r}, t) = \psi_j \exp[i\mathbf{k} \cdot \mathbf{r} - i\omega t] \quad (1.21)$$

where  $\mathbf{k}$  is the wave propagation vector,  $\|\mathbf{k}\| = 2\pi/\lambda$ , and  $\psi_j$  represents one of the components of  $\mathbf{E}$ ,  $\mathbf{B}$ ,  $\mathbf{u}$ , and  $n$ .

The magnetic field and number density equations can be separated into two parts:

$$\mathbf{B}(\mathbf{r}, t) = \mathbf{B}_0 + \mathbf{B}_1(\mathbf{r}, t) \quad (1.22)$$

$$n(\mathbf{r}, t) = n_0 + n_1(\mathbf{r}, t) \quad (1.23)$$

where  $\mathbf{B}_0$  is a constant, uniform field and  $n_0$  is the electron number density in the absence of waves. For cold, isotropic plasmas,  $\mathbf{B}_0 = 0$ . Equation 1.13 can be further simplified as the second-order, nonlinear  $\mathbf{u} \times \mathbf{B}_1$  term can be neglected in plasma waves if the average electron velocity is much less than the wave phase velocity ( $u \ll \omega/k$ ), which holds for the proposed plasma antenna.

In the Fourier transformation,  $\nabla$  and  $\partial/\partial t$  are replaced by  $i\mathbf{k}$  and  $-i\omega$  respectively, so neglecting second-order terms and using Equation 1.20, transformations of Equations 1.13, 1.17, and 1.18 are transformed:

$$\begin{aligned} -i\omega m\mathbf{u} &= -e(\mathbf{E} + \mathbf{u} \times \mathbf{B}_0) - m\mathbf{v}\mathbf{u} \\ &= -e\mathbf{E} - m\mathbf{v}\mathbf{u} \end{aligned} \quad (1.24)$$

$$\mathbf{u} = -\frac{e}{m(\mathbf{v} - i\omega)}\mathbf{E} \quad (1.25)$$

$$\mathbf{k} \times \mathbf{E} = \omega \mathbf{B}_1 \quad (1.26)$$

$$i\mathbf{k} \times \mathbf{B}_1 = \mu_0(-en_0\mathbf{u} - i\omega\varepsilon_0\mathbf{E}) \quad (1.27)$$

The electric field vector can be separated into a longitudinal ( $\mathbf{E}_\ell$  parallel to  $\mathbf{k}$ ) and transverse ( $\mathbf{E}_t$  perpendicular to  $\mathbf{k}$ ) component:

$$\mathbf{E} = \mathbf{E}_\ell + \mathbf{E}_t \quad (1.28)$$

From Equations 1.26, 1.27, and 1.25:

$$\mathbf{k} \times \mathbf{E}_\ell = 0 \quad (1.29)$$

$$\mathbf{k} \times (\mathbf{k} \times \mathbf{E}_t) = -k^2 \mathbf{E}_t = -\left[ \frac{i\omega\mu_0 e^2 n_0}{m(\nu - i\omega)} + \frac{\omega^2}{c^2} \right] (\mathbf{E}_\ell + \mathbf{E}_t) \quad (1.30)$$

Separating Equation 1.30 into its longitudinal and transverse components yields the dispersion relation for a longitudinal mode (assuming  $\mathbf{E}_\ell \neq 0$ ):

$$\left[ \frac{\omega_{pe}^2}{c^2(1 + i\nu/\omega)} - \frac{\omega^2}{c^2} \right] \mathbf{E}_\ell = 0 \quad (1.31)$$

$$\omega^2(1 + i\nu/\omega) - \omega_{pe}^2 = 0 \quad (1.32)$$

and a transverse mode (assuming  $\mathbf{E}_t \neq 0$ ):

$$-k^2 \mathbf{E}_t - \left[ \frac{\omega_{pe}^2}{c^2(1 + i\nu/\omega)} - \frac{\omega^2}{c^2} \right] \mathbf{E}_t = 0 \quad (1.33)$$

$$(\omega^2 - k^2 c^2)(1 + i\nu/\omega) - \omega_{pe}^2 = 0 \quad (1.34)$$

Assuming that collisions can be ignored when  $\nu/\omega \ll 1$  (i.e., collision frequency much

less than wave frequency), the longitudinal and transverse modes respectively turn into:

$$\omega^2 = \omega_{pe}^2 \quad (1.35)$$

$$k^2 c^2 = \omega^2 - \omega_{pe}^2 \quad (1.36)$$

Equation 1.35 shows that longitudinal oscillations can only occur at the plasma frequency. Equation 1.36 shows that traveling waves  $k$  are imaginary when  $\omega < \omega_{pe}$  but real when  $\omega > \omega_{pe}$ . When  $k$  is real, the transverse wave propagates with phase velocity  $v_{ph} = \frac{\omega}{k} = \frac{c}{\sqrt{1 - \omega_{pe}^2/\omega^2}}$  and group velocity  $v_g = \frac{\partial \omega}{\partial k} = \frac{c^2}{v_{ph}}$ . However, if  $k$  is imaginary and  $\omega < \omega_{pe}$ , the transverse wave is exponentially damped. These “evanescent waves” will not propagate through the plasma.

Plasma frequency  $\omega_{pe}$  – and therefore electron number density (from Equation 1.5) – is the most important parameter in determining if the plasma acts like a conductor or dielectric. For incoming wave frequencies less than the plasma frequency ( $\omega < \omega_{pe}$ ), the plasma behaves like a conductor – electrons have enough time to respond and exponentially dampen the incoming electromagnetic wave. As the signal frequency increases and approaches the plasma frequency, the electrons cannot respond quickly enough, and the signal propagates through the plasma like a dielectric medium. Figure 1.14 illustrates the dual behavior of plasmas depending on the frequency of the incoming wave compared to the plasma frequency.

For the plasma antenna to be operational, the plasma must behave as a conductor. Therefore, when a segment is turned on, a plasma must be generated with a high enough electron density such that the plasma frequency is greater than the pulse frequency of the incoming VLF waves.

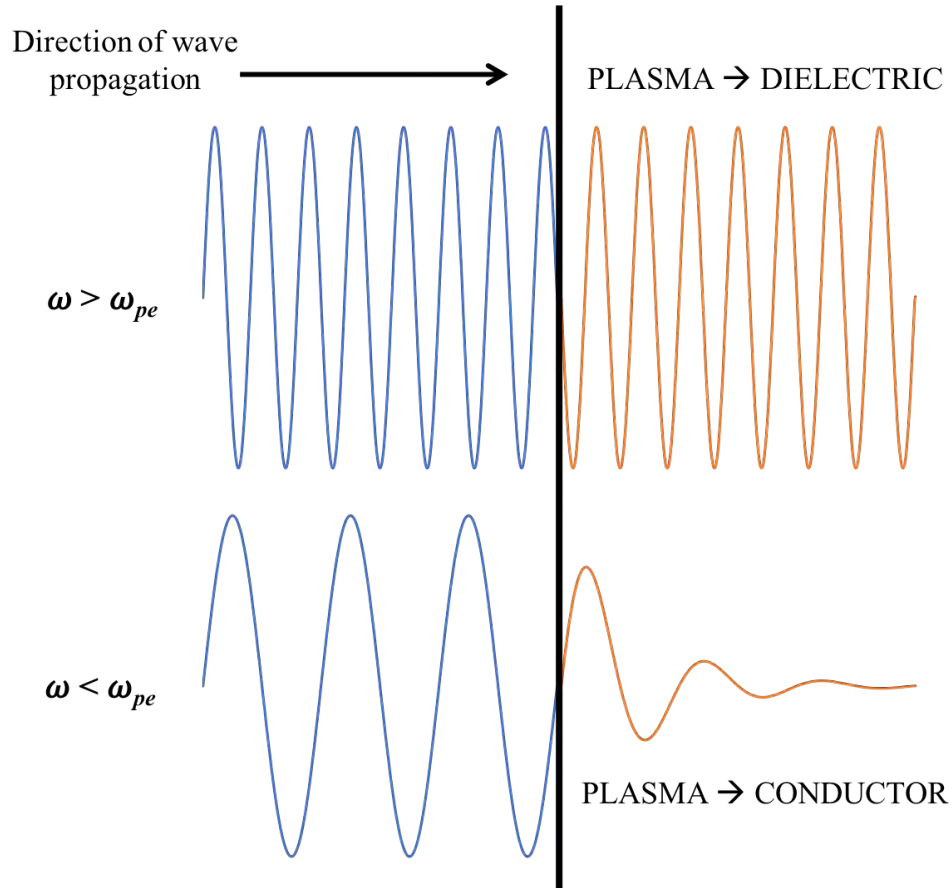


Figure 1.14: Plasma behaves as a conductor when the traveling wave frequency is less than the plasma frequency ( $\omega < \omega_{pe}$ ), resulting in the wave being damped in the plasma. Plasma behaves as a dielectric when  $\omega > \omega_{pe}$ , and the wave propagates through the plasma.

### 1.3.3 Plasma Parameters

This subsection will go into more detail about the crucial plasma parameters that determine if the generated plasma is suitable to be used in a segmented plasma antenna.

#### *1.3.3.1 Plasma Frequency*

Plasma frequency refers to how quickly the plasma can collectively react to a disturbance. If the plasma is assumed to be cold and the thermal motions of the electrons are neglected, the electron density is considered to oscillate at the plasma frequency given by Equation 1.5. For plasma antenna applications, the plasma frequency is the cutoff frequency. As seen in Figure 1.14, the plasma acts as a conductor to signals passing through with a lower frequency and as a dielectric to signals passing through with a higher frequency. For a plasma antenna, the  $\omega$  of interest is not the 3-30 kHz of VLF waves but instead the high-frequency modulated pulses that encapsulate the VLF waves.

#### *1.3.3.2 Plasma Conductivity*

Plasma conductivity is a measure of how well a plasma can conduct an electric current. The AC longitudinal conductivity for an isotropic (unmagnetized) plasma is [1]:

$$\sigma_0 = \frac{n_e e^2}{m_e(\nu_c - i\omega)} = \frac{n_e e^2(\nu_c + i\omega)}{m_e(\nu_c^2 + \omega^2)} \quad (1.37)$$

As also seen in Figure 1.14, plasma conductivity depends on wave frequency  $\omega$  and  $\omega_{pe}$ . A plasma antenna will be a good, low-loss conductor only when its operating frequencies are below the plasma frequency. When the plasma is turned off, and the electron number density drops enough such that the plasma frequency is now less than the operating frequency, the plasma becomes non-conducting – that segment of the antenna is off.

### 1.3.3.3 *Electron Density & Temperature*

Electron density describes the number of electrons in a given plasma volume. Similar number densities can be given for the other species in a plasma, including ions and neutrals. Each of these species follows a velocity distribution function. If the electrons, for example, follow a Maxwellian distribution, the temperature of that distribution is defined as the electron temperature  $T_e$ . The electron temperature in a plasma can be significantly higher than the neutral and ion temperatures because the rate of energy transfer from the electrons to ions and neutrals or from the plasma ionization source to the massive particles is slower than the transfer from the source to the electrons. As such, electron temperature is usually given in units of electron volts (eV) where  $1 \text{ eV} \approx 11600 \text{ K}$ .

Assuming that each segment of the plasma antenna is three meters long, the maximum duration for a VLF pulse to pass through that segment is 10 nanoseconds. To be a plasma antenna for VLF waves,  $\omega_{pe}$  must be considerably greater than  $1/10 \text{ ns} = 1 \text{ GHz}$ . From Equation 1.5,  $\omega_{pe} \propto \sqrt{n_e}$ , so electron density is the main driver for the plasma to act as a conductor. 1-GHz signal pulses passing into the plasma antenna would correspond to an electron density of at least  $10^{18} \text{ m}^{-3}$ . Potential parameters that could affect  $n_e$  are pressure in the plasma cell, discharge voltage, discharge pulse frequency, discharge pulse width, and gas selection.

### 1.3.3.4 *Plasma Breakdown & Quench Times*

Beyond having a high enough electron density in the plasma, the plasma must be ionized and recombined rapidly enough to gate the passing of the modulated input signal. As described in the previous subsection, the propagation delay of an EM wave through a three-meter antenna is 10 ns, so the pulse width must be shorter. For this example plasma antenna, the plasma cell conductivity must switch on and off in at most 10 ns.

Plasma quench time is governed by both plasma diffusion and ion-electron recombination, so input parameters to affect quench time are coupled. However, rapid

ionization of the plasma is also necessary, and there is typically an opposite tradeoff in the parameters that speed up recombination and ionization. Faster ionization and electrical breakdown occur at low pressures, but fast recovery via plasma recombination requires higher pressure, so faster recombination rates while retaining fast ionization likely necessitates higher breakdown voltages. Nanosecond, high-voltage pulses can be applied to electrodes to initiate a breakdown on the nanosecond time scale, but that time will also depend on the electron-neutral collision frequency, electron temperature, and gas. To date, turn-on and turn-off times on the order of 10s of nanoseconds have yet to be demonstrated by researchers.

#### **1.4 Research Goals**

The main challenge in demonstrating an operational, segmented plasma antenna is to accurately tune the plasma such that it can support the process shown in Figure 1.12. Properly controlling the plasma conductivity as well as achieving a high enough plasma frequency will be crucial in the plasma antenna's implementation.

As mentioned previously, switching the plasma on and off is analogous to bringing the plasma above and below a critical level of conductivity that is required to carry the current. This level of conductivity is determined by the plasma frequency, which is in turn determined by the electron number density of the plasma at a given moment. However, to date, there have not been any direct, time-resolved measurements of electron density and electron temperature for low-pressure ( $\approx 1$  Torr), nanosecond pulsed argon discharges. There have only been a limited number of pulsed plasma dynamics experiments and theoretical models to simulate nanosecond pulsed operation and to determine the time evolution of plasma parameters during a pulse period [7, 30]. Therefore, more research must be done on pulsed plasmas to tailor a given plasma to an antenna design.

The current understanding of the physics behind pulsed plasmas and the time-evolution of their behavior can be further explored through the two main questions of this dissertation:

**1. What drives the rapid ionization and recombination of pulsed plasmas, and what is necessary for these processes to happen on the nanosecond timescale?**

- (a) Determine a measurable parameter to define the ionization and recombination time of the plasma.
- (b) Quantify the plasma's ionization and recombination time to determine if the plasma can be turned on and off fast enough to be used as a VLF plasma antenna.

**2. How do pulser operating conditions and pressure affect the electron temperature, electron density, and plasma frequency of a pulsed plasma?**

- (a) Obtain time-resolved electron temperature and electron number density measurements for a low-pressure, argon pulsed plasma.
- (b) Can a plasma be tuned with the correct on and off conductivity to use in a VLF plasma antenna?

1.4.1 Dissertation Overview

The remainder of this dissertation details the experimental, modeling, and analytical effort needed to answer the two research questions above. Chapter 2 presents the full experimental setup used for testing. Chapter 3 details the diagnostics system that was designed and implemented to collect time-resolved data from the generated plasma. Chapter 4 discusses plasma equilibrium models and the PrismSPECT model that was used to translate the collected, time-resolved spectroscopy into time-resolved electron temperature and electron density measurements. Chapter 5 examines the results from steady-state plasma discharges while Chapter 6 examines the results from nanosecond-pulsed plasma discharges and aims to answer the research questions presented previously. Chapter 7 summarizes the contributions of this dissertation and recommends improvements and future work.

## **CHAPTER 2**

### **EXPERIMENTAL SETUP**

A prototype plasma cell and corresponding vacuum components were designed and manufactured to be the main proof-of-concept testbed for this project before implementing the full plasma antenna. The experimental setup of the plasma cell was based on the work of Chan and Singletary, both of whom individually worked with optical diagnostics on a tabletop plasma cell [31, 32]. Chan conducted an experimental study on the effect of pulse repetition rate and pressure on the rise time of an argon pulsed plasma with spectroscopic and photodiode data. He also used optical emission spectroscopy techniques with Boltzmann plots to estimate time-averaged electron temperature and density values for a pulsed plasma. Singletary expanded on Chan's work by recording light curves at a range of pressures and ionizing voltages to determine optimal discharge conditions for the fastest rise time. Instead of using Boltzmann plots, Singletary estimated time-averaged electron temperature and density of steady, DC plasma and nanosecond-pulsed plasma by comparing the measured plasma spectral emission lines to PrismSpect software-simulated lines.

All experiments in this dissertation were performed in a custom plasma cell at the Georgia Institute of Technology's High-Power Electric Propulsion Laboratory (HPEPL). The setup is shown in Figure 2.1.

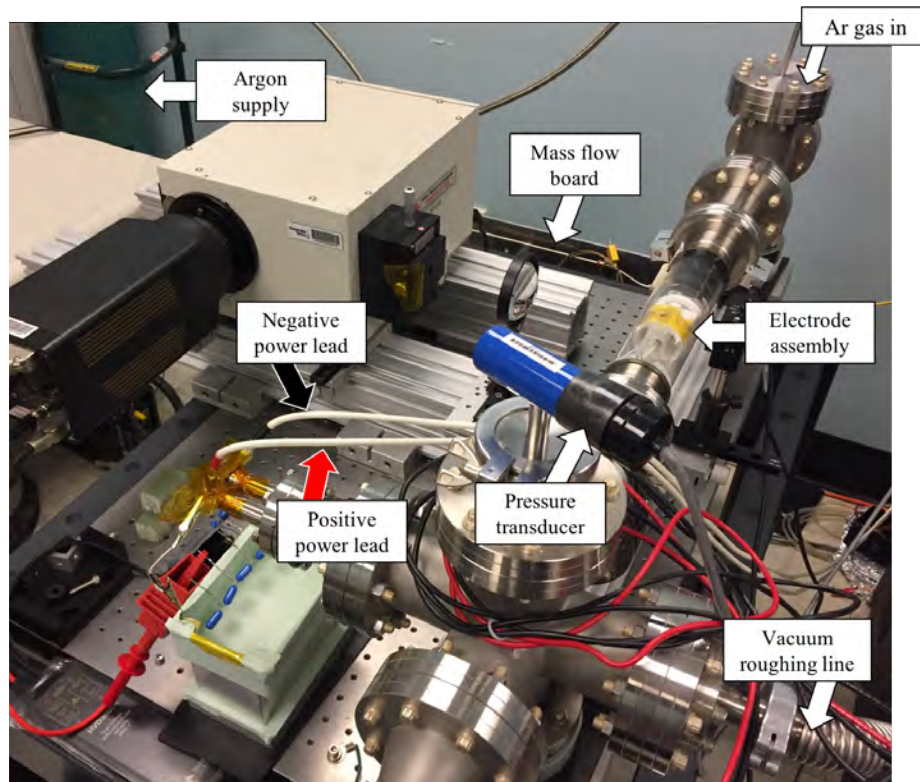


Figure 2.1: Experimental setup with plasma cell, electrodes, and vacuum system.

## 2.1 Plasma Cell

The Pyrex plasma cell was handblown at the Scientific Glassblowing Laboratory in Georgia Tech's Chemistry Department. It had a 2.25-inch outer diameter and was 9-inches long with glass-to-steel ISO-type flanges on either end (Figure 2.2). This type of flange greatly reduced the stress applied to the glass and the time needed during repeated assembly and disassembly of the plasma cell [31, 32]. The cell was attached to a 6-way and 4-way cross with 4.5-inch ConFlat (CF) flanges, through which all the electrical connections were fed. The experimental setup was placed on a 3 ft  $\times$  4 ft vibration-isolated optical table from Thorlabs.

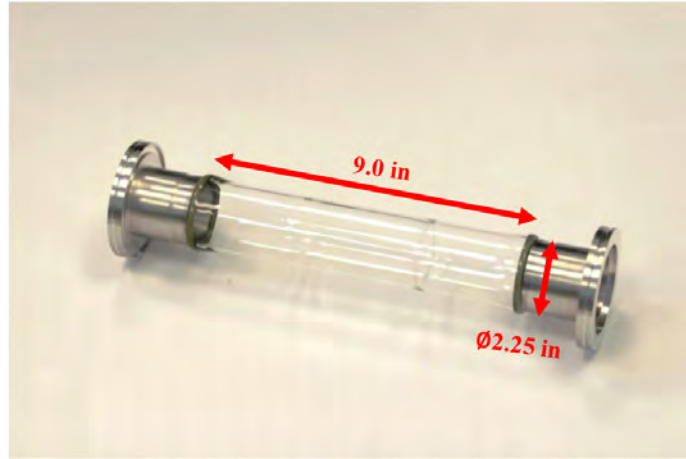


Figure 2.2: Glass plasma tube with ISO-type flanges, modified from [31].

### 2.1.1 Plasma

Two plasma discharges – a steady-state plasma and a nanosecond-pulsed plasma – were generated within the plasma cell. A voltage breakdown-generated plasma was selected over other types of plasmas because of the need to precisely control input parameters and input energy. A radio-frequency (RF) plasma, for example, utilizes the same electron cascade process as a DC glow discharge and is capable of producing a more spatially-uniform and homogeneous plasma, but the noise from the RF generator as well as the uncertainty in timing the RF wave generation to RF plasma creation makes a RF plasma unsuitable for investigating transient, nanosecond, time-resolved plasma dynamics [33, 34].

Argon was selected as the working gas for the plasma because it was an inert gas and had a low breakdown voltage ( $\sim 200$  V at 1 Torr for a 1-cm electrode gap from Figure 1.7). Similarly, 1-Torr argon was chosen as the base test pressure because it corresponded to a minimal breakdown voltage for this experimental setup, which allowed for a greater range of discharge voltage test conditions.

### 2.1.2 Electrodes

The electrodes used in this dissertation were fashioned from 5/32" x 1/2" domed anodized aluminum rivets that were threaded into rectangular Macor ceramic plates (1.6" x 1" x 0.25" thick) and set 1 cm apart in a Macor mount with four 1/16" diameter alumina ceramic rods. The electrode assembly, as seen in Figure 2.3, was painted with Ceramabond 569 to lock the assembly together and to cover any exposed metal components as well as to provide additional insulation protection to the assembly. Slots were designed in the support structure to fit the high-voltage 22-AWG Cicoil wire, and one side of the support structure included a mount for a Langmuir probe that was used in early verification testing.

A set of serrated and needle-like electrodes, shown in Figures 2.4 and 2.5, were also designed for testing. The serrated electrodes were machined from 316 stainless steel to have a 1/2" square cross-section. The serration was due to four 90° steps, each 1/16" tall. The needle-like electrodes were machined from a 316 stainless steel rod to have a diameter of 5/32" and a point 1/8" tall. Although neither of these electrode geometries were used for testing since the target plasma properties were fully achieved with the domed electrodes, investigating the effects of electrode geometry on plasma parameters would be interesting for future work.

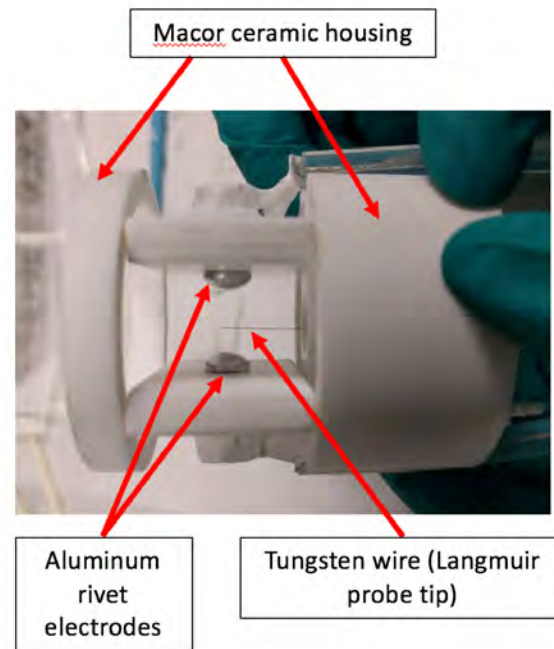


Figure 2.3: Rivet electrodes in its Macor housing.

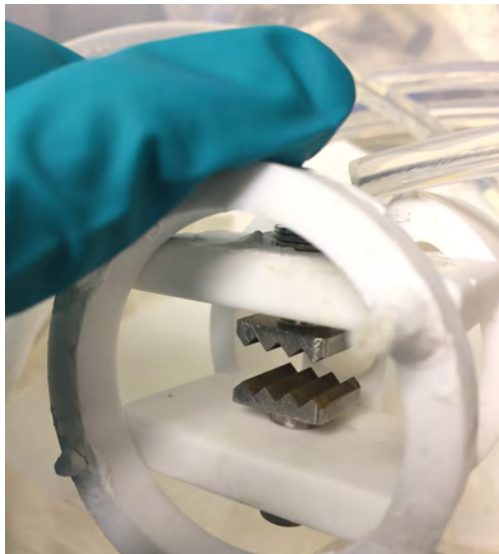


Figure 2.4: Serrated electrodes in its Macor housing.



Figure 2.5: Needle electrode & supporting threaded rod.

## 2.2 Vacuum System

A simple vacuum and mass flow system was implemented to evacuate the plasma cell and maintain the test cell at desired test pressures. Pressure in the plasma cell was monitored by

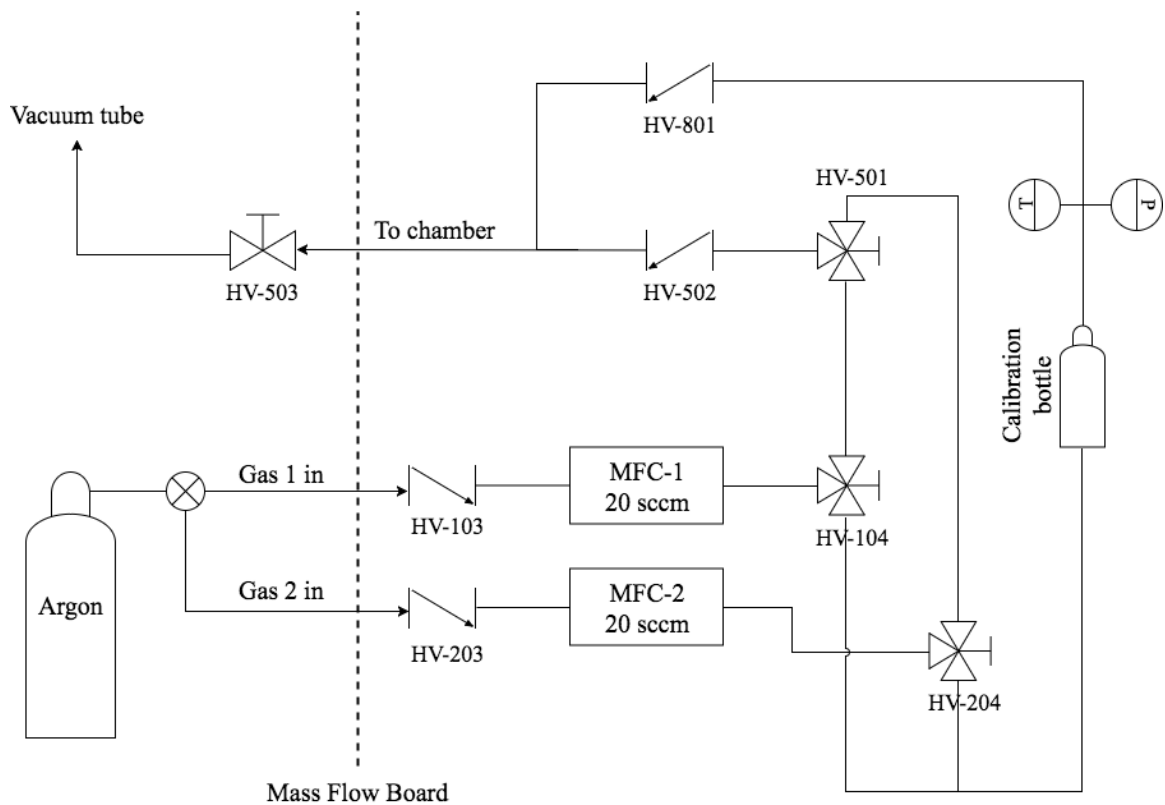


Figure 2.6: Flow schematic for argon flow into the plasma cell.

a Kurt J. Lesker 375 Series Controller and a 275 Pirani gauge, which had a pressure range of  $10^{-4}$ –1000 Torr  $N_2$ . At the beginning of a test, the gate valve of an Alcatel Adixen Pascal 2021 rotary vane vacuum pump was fully opened to bring the cell pressure to about 50 mTorr. After turning on the mass flow system, one of the following two pressure control systems was implemented.

### 2.2.1 Mass Flow System

An argon-calibrated 247D MKS Mass Flow Controller and a 200-sccm flow meter controlled ultra-high purity (99.999%) argon flow into the plasma cell. Figure 2.6 shows the flow schematic for the experimental setup.

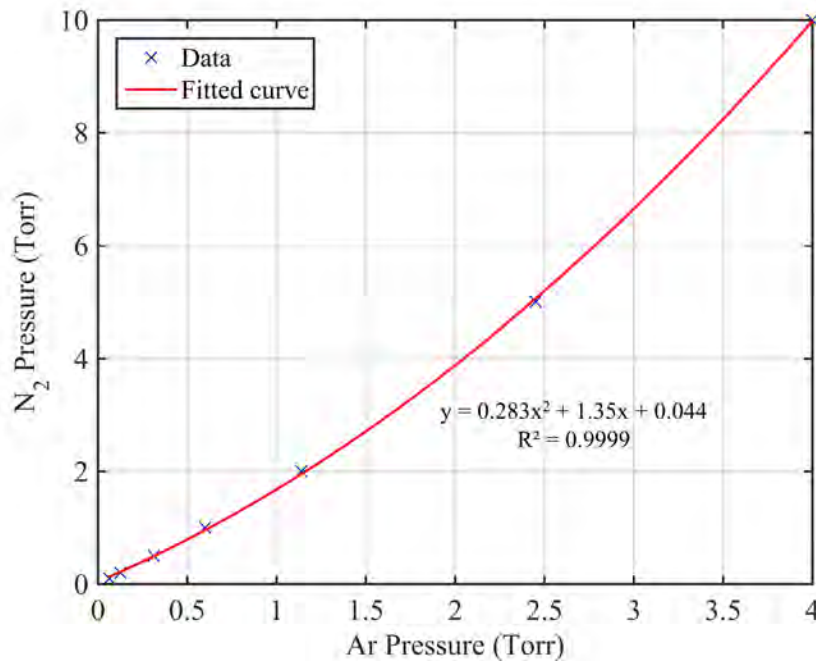


Figure 2.7: Conversion from desired argon gas pressure to displayed nitrogen gas pressure on the Lesker pressure controller. Fit line from a 2nd order polynomial fit with  $R^2 = 0.99$ .

## 2.2.2 Pressure Control System

The plasma cell's operating pressure in argon was converted to nitrogen pressure using an experimentally-based pressure conversion chart from Lesker as shown in Figure 2.7, which encompassed the 1-3 Torr argon pressure range used during testing.

### 2.2.2.1 Manual Pressure Control

The first type of pressure control was adjusting the roughing pump gate valve and mass flow controller (MFC) until the KJLC pressure controller displayed the desired N<sub>2</sub>-converted target test pressure. Any drifts greater than 5% of the desired target pressure during testing would require an adjustment of the gate valve position or the mass flow. If the vacuum pump's valve was being used as the control, some delicacy was required as the relationship between valve position and cell pressure was extremely non-linear and prone to hysteresis. Instead of using the KJLC-indicated pressure as direct feedback for the valve position,

very small adjustments were made 10 seconds apart, giving the pressure reading enough time to respond to the new valve position. A similar wait time was necessary if manually modifying the MFC to set cell pressure, but this method allowed for much more precise control than adjusting the gate valve.

#### *2.2.2.2 Automated Pressure Control*

A second type of automated pressure control was later implemented to mitigate the  $\pm 10\%$  chamber pressure overshoot/undershoot problems observed when adjusting the valve or MFC. By automating the pressure system using feedback loops and utilizing the remote-control capabilities of the MFC, pressure could be maintained more consistently. After setting the vacuum pump gate valve in a certain position, the chamber pressure was continuously fed into the MFC, which increased or decreased argon flow into the plasma cell depending on the current pressure reading relative to the target pressure.

After the vacuum pump was turned on, an initial flow value was set on the MFC by an Arduino microcontroller (seen in Figure 2.8). The Arduino received a pressure reading from the KJLC and updated the initial flow value by an amount proportional to the difference between the current and desired pressure. For instance, if the chamber pressure was too low, the flow increased to raise pressure. The updated flow value was then converted into a control voltage that was fed by the Arduino to the MFC. In addition to the Arduino, a simple low-pass filter circuit was used to send a constant, low-voltage turn-on signal to the MFC. The higher-voltage signal corresponding to the flow value did not require the low-pass filter and was directly connected to the MFC. With proper testing and calibration, this pressure control system mitigated pressure oscillations as well as severe over- and undershooting of the desired pressure.

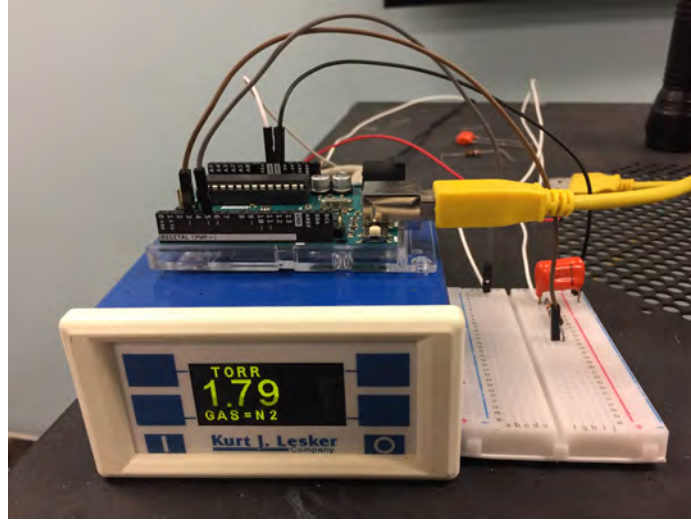


Figure 2.8: Automated pressure control system with KJLC, Arduino board, and low-pass filter holding pressure at 1-Torr argon (1.79-Torr nitrogen).

### 2.3 Power

Two different power supplies were used for experimental testing - one to initiate a steady-state plasma and the other to initiate the nanosecond-pulsed plasma. Although only one power supply could be connected to the chamber at any given time, the connections were identical. Alligator-terminated leads from a power supply were attached to the air-side power flange of the vacuum chamber. Positive and negative lengths of high-voltage, 22-AWG Cicoil wire connected the vacuum-side of the power flange to the respective positive and negative electrodes in the test cell.

A Lambda GEN600-2.6 power supply was used to generate the steady-state plasma. A custom FID pulser (FPG 1-50NM100A) capable of pulsing up to 50 kHz and supplying 500-1000 V pulses with a full-width, half-max (FWHM) defined pulse width of 5-100 ns [35] was originally proposed for generating nanosecond-pulsed plasma. This was because the pulse frequency was high enough and the pulse width short enough for the FID pulser to generate a demonstration plasma for the plasma antenna. However, from Singletary's pressure sweep [32] and initial testing of nanosecond-pulsed plasmas, there were concerns that the pulser output voltage would be too low for meaningful voltage and pressure sweeps

for time-resolved testing.

Instead of the FID pulser, an Eagle Harbor Technologies NSP-120-20F nanosecond pulser (NSP) was used to generate the nanosecond-pulsed plasma. This unit was capable of pulsing up to 10 kHz and supplying up to 20 kV. However, the minimum pulse width of the pulser was 20 ns, so the initially-proposed goal of having a plasma that was created and quenched in 10 ns needed to be revised to at least 20 ns. While a plasma generated with a 20-ns voltage pulse would necessitate a longer plasma antenna segment than one that was generated with a 10-ns voltage pulse due to the naturally longer lifetime of the plasma, the longer pulse width would still provide valuable insight into how a nanosecond-pulsed plasma is affected by operating conditions such as pressure and discharge voltage. Furthermore, the time-resolved measurements would still help determine if the plasma at a test operating condition could be used as a proof-of-concept demonstration for a VLF plasma antenna. Understanding the trends that result from using the 20-ns voltage pulse will guide what conditions should be used with a shorter voltage pulse if a shorter plasma antenna than what can be created with a 20-ns plasma is desired.

The capabilities of the NSP thus drove the test matrix, to be discussed in Chapter 6. While the pulse width was fixed at 20 ns, the discharge voltage and pulse repetition frequency could be individually adjusted. The full operating test space of the NSP is shown in Figure 2.9 and suggests there should be no issues with using the max 20-kV output of the NSP at 20 ns except at the highest pulse frequencies [36]. However, it is important to note that the maximum discharge voltage available is not only power-limited but also load-driven, so the output voltage waveform must be measured. This will be further discussed in the following chapter.

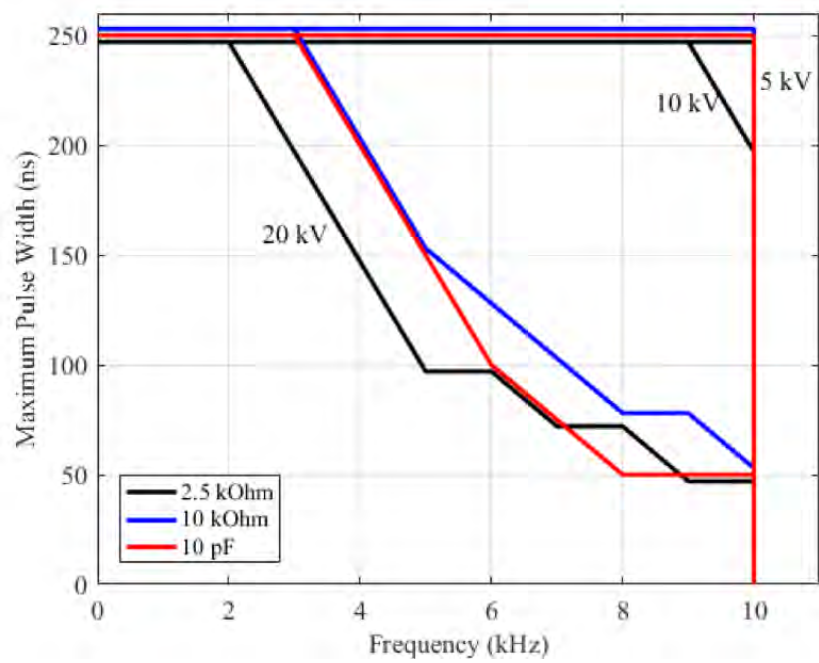


Figure 2.9: Available operating parameter space for the NSP-120-20F at different load types [36].

## **CHAPTER 3**

### **DIAGNOSTICS**

Two sets of diagnostic tools were implemented to take plasma measurements from the prototype plasma cell described in Chapter 2 – one for time-averaged measurements of steady-state plasmas and one for time-resolved measurements of pulsed nanosecond plasmas. A large part of this research dealt with the design and implementation of a new plasma diagnostics system that could temporally sweep and obtain nanosecond, time-resolved measurements of the plasma. Results from this non-invasive technique that determined electron number density and electron temperature would verify if the generated plasma could be used for a VLF plasma antenna.

#### **3.1 Steady-State Diagnostics**

Plasma measurements were taken with an optical emission spectroscopy (OES). Coupling the emission spectra with a collisional-radiative simulation described in Chapter 4 led to electron density and temperature values.

##### 3.1.1 Time-Averaged Optical Emission Spectroscopy

An HR4000 OceanOptics spectrometer was used to gather time-averaged (on the order of hundreds of milliseconds) optical emission data for the steady-state plasma. The HR4000 was responsive from 200-1100 nm and uses a 3648-element linear CCD array detector. Figure 3.1 shows the optical elements inside the spectrometer. For data collection, 20 scans of the plasma emission were taken and averaged along with 20 dark scans with the iris closed to subtract out any stray electrical noise. The integration time of the spectrometer was dependent on the intensity of the plasma emission and varied from 100-300 ms.

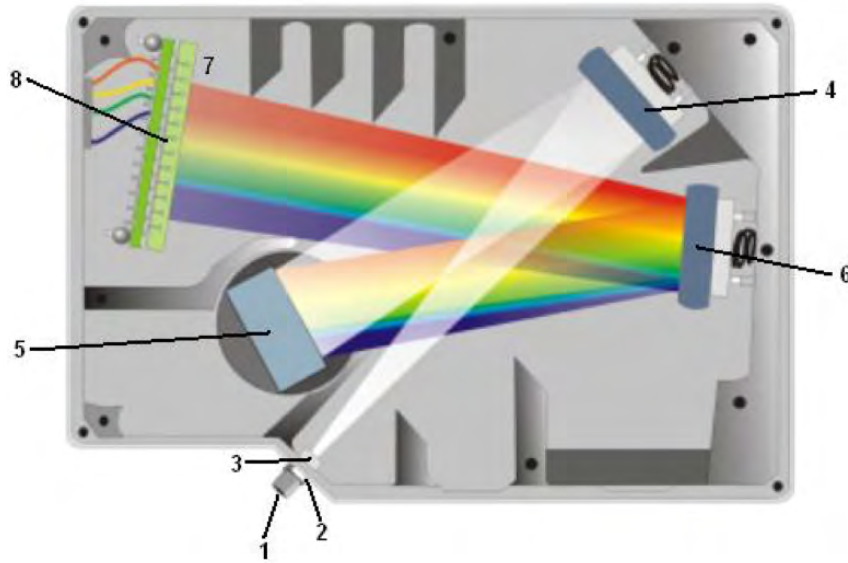


Figure 3.1: HR4000 spectrometer with components: 1. SMA Connector; 2. slit; 3. filter; 4. collimating mirror; 5. grating; 6. focusing mirror; 7. L2 detector collection lens; 8. CCD detector [37].

#### 3.1.1.1 Wavelength Calibration

The spectrometer was calibrated for wavelength and light intensity before each test. A wavelength calibration was performed by shining an Ocean Optics HG-1 Mercury-Argon light source through the plasma cell and having the HR4000 fiber optics cable mounted to an iris on the opposite side of the cell. A dark spectrum with 20 scans was first taken with the iris closed; the iris was then opened for a light spectrum of 20 scans. The corresponding spectra were analyzed with a custom MATLAB script that compared the wavelength peaks from the spectrometer to the known mercury and argon peaks from the NIST atomic database [38]. A third-order polynomial was fitted to the spectrometer-collected versus known wavelengths curve based on the OceanOptics calibration procedure [37]. That polynomial was then applied to all wavelength data taken on a given test day to correct the spectrometer data.

### 3.1.1.2 Intensity Calibration

An intensity calibration was performed with a StellarNet SL1-CAL 2800-K tungsten lamp. After 20 minutes of warming up to temperature, the tungsten lamp was placed on the opposite side of the cell, similar to the setup for the wavelength calibration. A dark spectrum of 20 scans was taken with the iris closed; the iris was then opened for a light spectrum of 20 scans. The spectra were analyzed with a custom MATLAB script that compared the overall light intensity curve from the spectrometer to the calibrated intensity data provided by StellarNet. The wavelengths for the measured intensity data were first corrected with the wavelength calibration from that day, followed by the intensity correction factor.

## 3.2 Time-Resolved Diagnostics

In order to gain insight into the ionization, recombination, and conductivity physics of nanosecond-pulsed plasmas, it was necessary to obtain time-resolved measurements of plasma properties such as electron temperature, electron density, and plasma frequency.

There are several measurement techniques to obtain time-resolved plasma parameters from a pulsed nanosecond plasma: Langmuir probes, optical emission spectroscopy (OES), laser diode spectroscopy, and Thomson scattering [6]. Of these four main diagnostics, Thomson scattering has the advantage of giving direct insight into plasma properties with excellent spatial and temporal resolution. It is a non-invasive measurement, interpreting the results is straightforward, and it does not depend on the plasma being in equilibrium [6]. Thomson scattering has been used in time-resolved measurements of nanosecond-pulsed argon and helium discharges, but it requires extensive specialized equipment and a hot (e.g.,  $T_e > 2$  eV), dense plasma. Thomson scattering is not a viable option if the electron density in the plasma is too low (e.g., below  $10^{13}$  cm<sup>-3</sup>) as the signal from the scattered electrons will be too weak [4, 6, 39]. While the plasma generated for each cell of the

plasma antenna will most likely have  $n_e \sim \mathcal{O}(10^{14} \text{ cm}^{-3})$  and  $T_e \sim \mathcal{O}(1 \text{ eV})$ , which is just within the range of Thomson scattering, the necessary laser equipment was not accessible within the timeframe of this project.

Langmuir probes are easy to build and implement but difficult to analyze. The calculated electron density and electron temperature values depend heavily on the interpretation of the Langmuir probe data, so this technique presents high uncertainty and does not provide sufficient verification that a given plasma is suitable for use in a VLF plasma antenna [40]. Langmuir probes are also intrusive diagnostic tools, so the insertion of the tungsten wire into the plasma could alter the plasma properties it is trying to measure. This intrusiveness is non-ideal when attempting to tune a plasma as precisely as will be needed for the antenna.

Several groups have used tunable diode laser absorption spectroscopy (TDLAS) to get time-resolved temperature and number density measurements in a pulsed argon plasma from the absorption spectra. However, most of those measurements were taken on a specific metastable argon species, and a detailed model was used to estimate or calculate electron temperature and electron number density [33, 41–43]. TDLAS is an accurate diagnostic when looking at specific species' or molecule's densities and gas temperatures but not as useful for  $n_e$  or  $T_e$  measurements [3, 33].

The last option is using optical emission spectroscopy (OES) to measure the effective electron temperature and emission spectra with Stark broadening and then solve the energy balance and Boltzmann equations to calculate the time evolution of plasma density values [7, 44]. Spectroscopy is a very established diagnostic tool that does not require much equipment, and line ratio techniques can determine  $n_e$  and  $T_e$ , but there is more uncertainty in the measured quantities due to the inexact determination of spectral peaks [33].

With the current resources and predicted plasma operating regime, OES was selected as the main diagnostic tool. Coupling OES with data from simulation-generated spectra has been shown to be a viable diagnostic for obtaining electron temperature and electron

density, but using a spectrometer like the HR4000 is orders of magnitude too slow to capture the rapid physics in a nanosecond pulsed discharge. Therefore, diagnostics with a much faster response time (on the nanosecond or picosecond time scale) must be implemented. This section details the diagnostic tools used to obtain such time-resolved plasma measurements.

### 3.2.1 PI-MAX ICCD Camera

PI-MAX made by Princeton Instruments is a first-generation, intensified-CCD (ICCD) camera (512 x 512 pixels) that was used to collect photons from the plasma cell. The PI-MAX camera uses a proximity-focused microchannel plate (MCP) image intensifier fiber-optically coupled to a CCD array. It is capable of a 4-ns gate, so PI-MAX can capture the various events of interest (i.e., ionization, “steady-state”, and recombination) in the pulsed plasma discharge. The PI-MAX can also take broadband plasma emission images as a visual reference of how the plasma looks at different operating points.

ICCD cameras work especially well in low-light conditions because of the photon amplification process seen in Figure 3.2 [45]. Photons entering the camera strike the photocathode and release electrons. When the intensifier is gated on, electrons are accelerated to the MCP and strike the channel walls, which generates even more electrons and results in electron gain (which can be adjusted by the MCP voltage). The electrons then strike the phosphor-fluorescent screen, which releases more photons than had originally struck the photocathode due to the electron gain. Those multiplied photons then produce charge on the pixels they strike on the CCD surface. Utilizing the intensifier tube results in a stronger signal and lower noise compared to non-intensified CCD cameras.

However, fiber-optic-coupled ICCD cameras such as the PI-MAX have a few disadvantages compared to CCD cameras – they are easily damaged with high-intensity light conditions and have lower spatial resolutions. Fortunately, high-intensity light was not a concern for the plasma emissions that were imaged by the ICCD. While there may

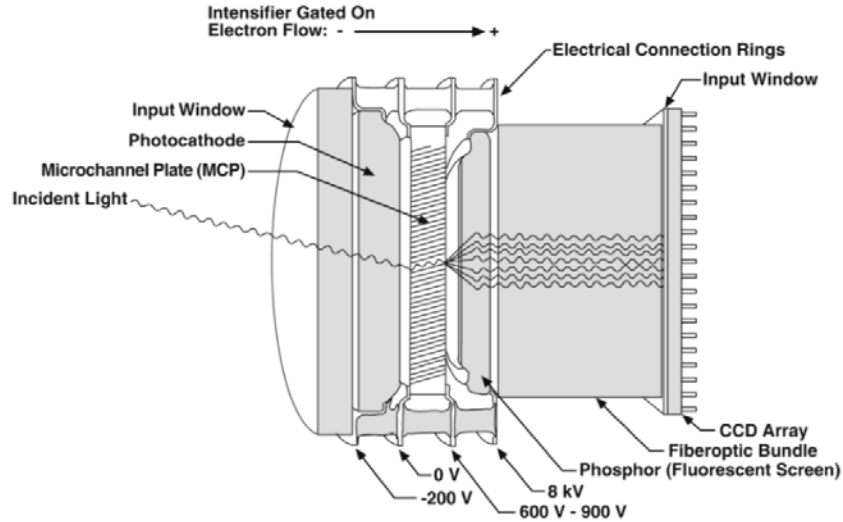


Figure 3.2: Major components of the intensifier-CCD, pulled from PI-MAX manual [45].

be some optical aberration (i.e., distortion or vignetting) and systematic image error (i.e., honeycomb patterning) to the image, the main purpose of the ICCD camera is for spectroscopy, not imaging, so the effects of those distortions were mitigated [46]. A larger issue is that the PI-MAX is fiber-optic coupled, so the intensifier is a fixed structure whose parts cannot be swapped. Since the photocathode and P43 phosphor coating on the PI-MAX intensifier have a sharp quantum efficiency cutoff (shown in Figure 3.3), and the photocathode and intensifier cannot be changed, the measurable plasma light wavelength was limited to 350-750 nm, which reduced the argon neutral and ion peaks that could be seen [45]. There is also a 2-ms phosphor decay associated with the P43, so there must be at least a 2-ms delay between individual frames or there will be ghost images from previous exposures. This timed delay could be directly addressed in the time synchronization of the entire system, discussed in Section 3.3.

To capture the nanosecond-pulsed plasma, the PI-MAX needed to gate at least twice as fast as the discharge pulse width. The image intensifiers and gate pulse generator in PI-MAX made it possible to have an optical gate time  $\leq 10$  ns [45]. While some PI-MAX cameras offer a 500-ps gating option if faster snapshots are required, the one that was used for this experiment did not have the “fast gate” board installed. While faster gating would

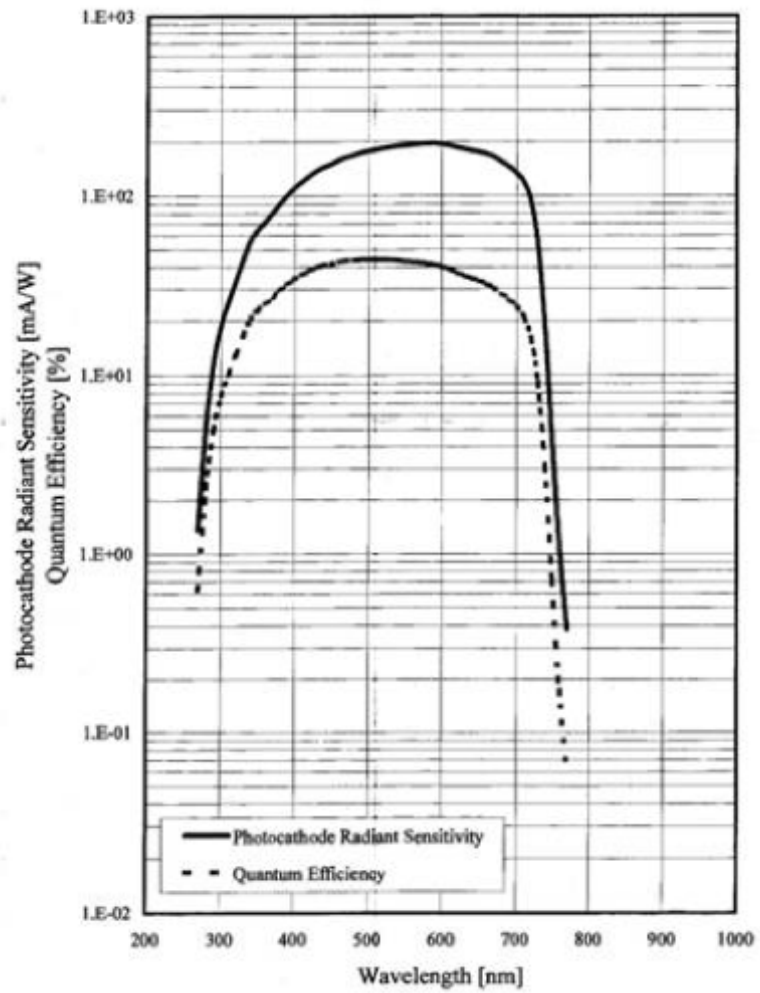
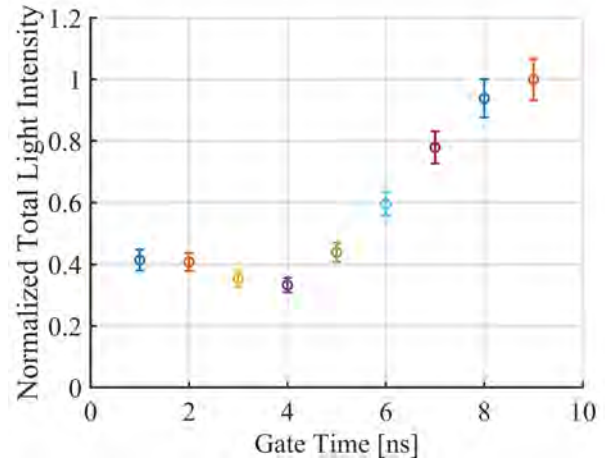
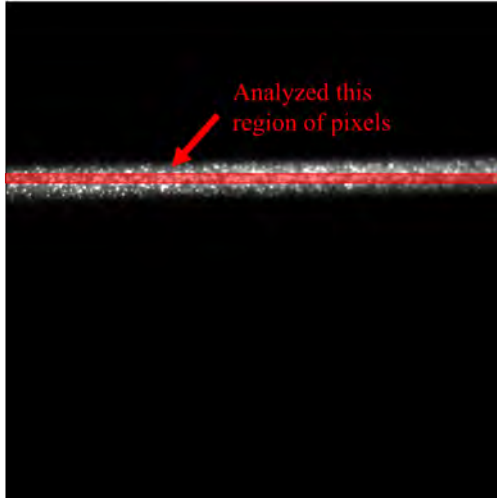


Figure 3.3: Spectral response characteristics for PI-MAX photocathode [45].



(a) Image of pulsed laser at 6-ns gate time.

(b) Normalized light intensity vs. gate time.

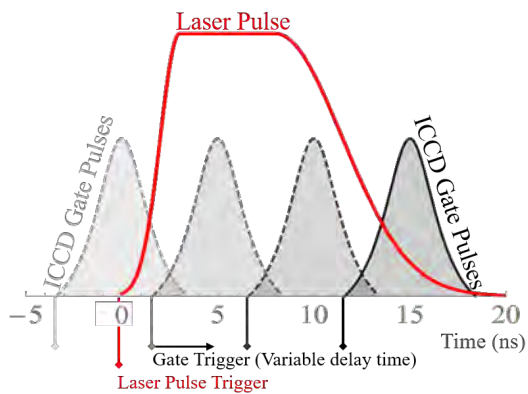
Figure 3.4: Identifying the fastest PI-MAX gating capabilities by measuring a pulsed laser intensity as a function of gate times.

be preferable to capture finer details of the pulsed plasma, a tradeoff between fast gating and good image quality (or low noise) needed to be made – fast gating naturally means fewer photons will reach the detector, so the resulting signal will be weaker.

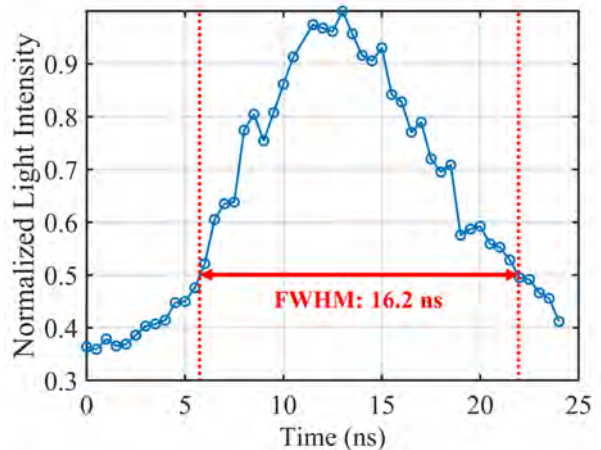
### 3.2.1.1 Gating Characteristics

As verification of the PI-MAX gate capabilities, a table-top experiment was conducted where the PI-MAX camera was pointed at a pulsed 532-nm laser, and the fastest gate time achievable with the camera was determined. Through a series of tests, the gate time of the camera was decreased in increments of 1 ns. 50 images at each gate width was taken, and those images were processed for a total intensity value across a rectangular region (as seen in Figure 3.4a). The results over nine different gate times, from 1-10 ns are represented in Figure 3.4b. As expected, there was a linear decrease in measured intensity as the gate time of the PI-MAX was dropped. However, taking into account the error bars, there was an intensity plateau from 1-4 ns, indicating that the camera could not gate faster than 4 ns.

A second set of tests were taken to verify that the PI-MAX gated in 4 ns. Using the same pulsed laser, the camera was set at a 4-ns gate time, and the delay generator controlling the



(a) Changing timing delay to sweep across laser pulse with 4-ns gate time.



(b) Normalized light intensity vs. delay time.

Figure 3.5: Verifying PI-MAX 4-ns gate time by sweeping gated intensity across laser pulse.

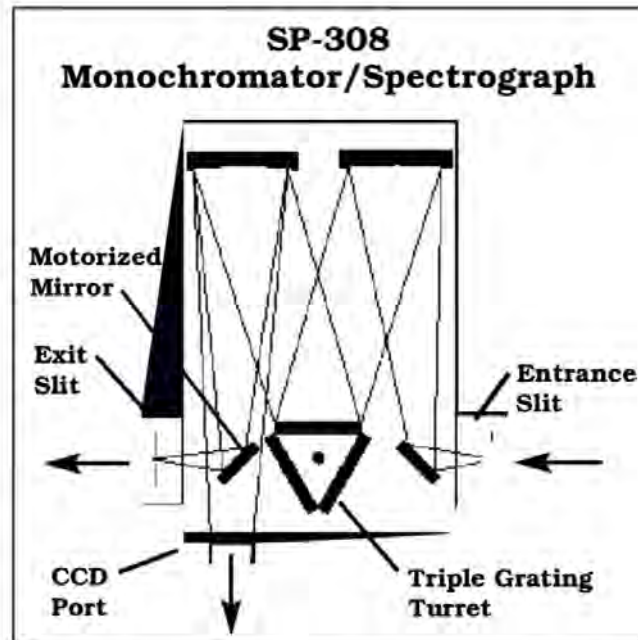
timing of the camera gating relative to the laser pulse was adjusted so the camera image of the laser line could barely be seen. As diagramed in Figure 3.5a, the delay generator was increased in 500-ps increments to sweep across the laser pulse. One image at each timing delay was taken, and all those images were processed over a rectangular region. The FWHM of the resulting timing curve was calculated (shown in Figure 3.5b), and Equation 3.1 was used to experimentally verify  $t_{gate}$ , the gate time of the PI-MAX 4 ns gate condition:

$$t_{gate} = t_{FWHM} - t_{pulse} \quad (3.1)$$

where  $t_{FWHM}$  is the FWHM of the laser pulse and  $t_{pulse}$  is the width of laser pulse. Due to jitter in the laser, the width of the laser pulse varied from 11.7 ns–12.9 ns, as measured from a 400-MHz avalanche photodiode (ThorLabs APD430A2). Using Equation 3.1 with  $t_{FWHM} = 16.2$  ns gave an experimentally determined PI-MAX gate time of  $3.9 \text{ ns} \pm 0.6 \text{ ns}$ .

### 3.2.2 Spectrograph

Acton SP-308 (of the SP-300i family) by Princeton Instruments is a triple-grating spectrograph that is mounted behind the ICCD detector. It has a focal length of 0.300 m,



Monochromator/Spectrograph with dual exit ports (1=monochromator, 1=spectrograph) and motorized mirror for rapid, computer controlled exit port selection.

Figure 3.6: Internal components of the Acton SP-308 spectrograph; pulled from SP-300i manual [47].

an overall spectral range of 185 nm-1100 nm, a resolution of 0.1 nm at 435.8 nm, and an accuracy of  $\pm 0.2$  nm. The three different gratings on the SP-308 are interchangeable on a turret inside the spectrograph and may be swapped for other gratings. All emission spectra were taken with a 600 gpm grating blazed at 500 nm. Figure 3.6 shows the spectrograph's internal schematic. The slit width of the SP-308 is adjustable from 0.010-3.000 mm, so the amount of light entering the spectrograph can change [47]. Through trial and error, the sharpest spectral peaks were measured with a slit width of 50  $\mu\text{m}$ .

The complete ICCD-spectrograph assembly, with necessary electrical and data connections, is shown in Figure 3.7. Both the PI-MAX camera and Acton spectrometer were fully controlled by the WinSpec software.

At its fastest, this ICCD-spectrograph assembly showed the full emission spectra of a

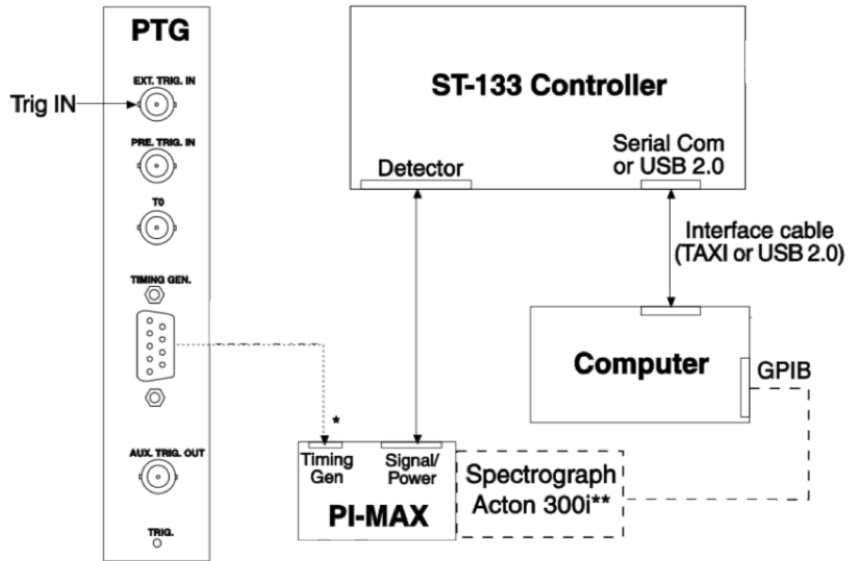


Figure 3.7: Schematic of PI-MAX camera connected with Acton SP-300i spectrograph for OES; adapted from PI-MAX manual [45].

given plasma averaged over  $\approx 4$  ns. At the same plasma conditions, the ICCD trigger was incrementally delayed to capture the full spectra a given time  $t$  later. This will be further discussed in Section 3.3. For every emission spectra, a line ratio analysis with spectral modeling software, to be detailed in Chapters 4 and 6, was conducted to determine  $n_e$  and  $T_e$  at that given instant in time. Doing this analysis over the entire plasma turn-on to turn-off duration provided the time-resolved electron temperature and density for a given set of operational parameters.

### 3.2.2.1 First Light

First light for the PI-MAX/SP-308 assembly was gathered with the calibrated OceanOptics HG-1 mercury-argon light source. A sample test utilizing the 600 groove/mm grating centered at a wavelength of 720 nm was taken in shutter mode with a 200-ms exposure time to the full CCD chip. Figure 3.8a illustrates the strong mercury-argon lines in the range of  $720 \text{ nm} \pm 30 \text{ nm}$ , and Figure 3.8b displays the visual representation of the diffracted bands of light in the spectrograph taken in PI-MAX's "imaging" mode.

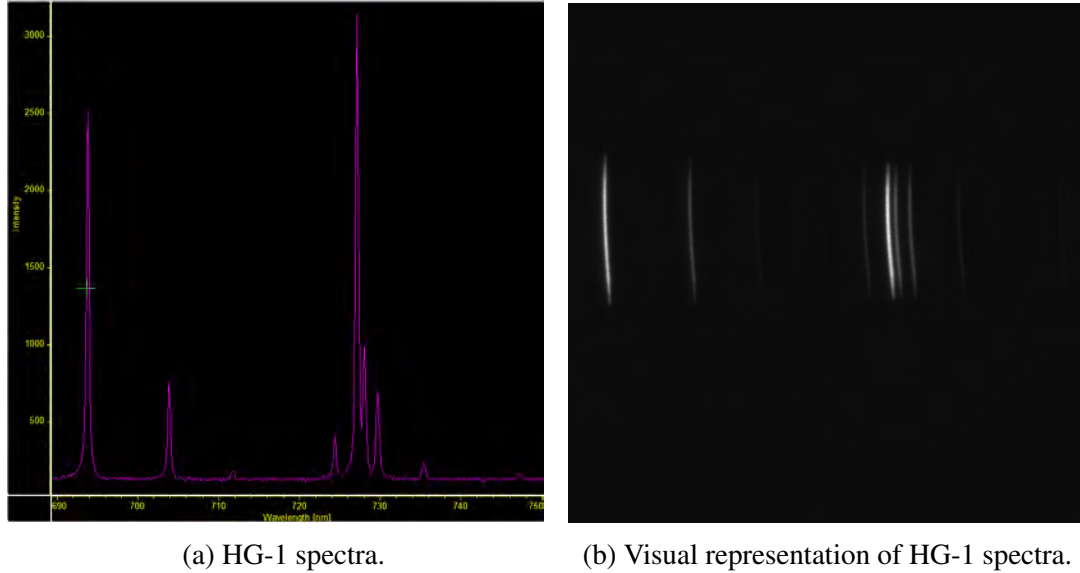


Figure 3.8: Uncalibrated HG-1 spectra taken in “spectroscopy” and “imaging” mode with a 600 groove/mm grating centered at 720 nm and an exposure time of 200 ms for first light verification.

### 3.2.2.2 Wavelength Calibration

The wavelength calibration for the ICCD/spectrograph assembly was more involved than that for the HR4000 spectrometer. Each grating in the SP-308 needed to be independently calibrated per the Spectrograph Calibration chapter in Princeton Instrument’s WinSpec manual and used the HG-1 mercury-argon lamp as the light source [48]. The first step calibrated the spectrograph’s offset to ensure there was no systematic shift in the spectrograph’s measured wavelength compared to the actual wavelength. This was done by “zeroing” the SP-308 wavelengths to a reference wavelength. However, other wavelengths could still be improperly calibrated, which was when the adjust calibration must be completed. Just as  $b$  represented the offset term in the general linear equation  $y = mx + b$ ,  $m$  needed to be calibrated so all other wavelengths seen by SP-308 was also the correct wavelength. The last in the calibration sequence was dispersion, where the proper focal length, inclusion angle, and detector angle were calculated so any peaks that show up on the far left or far right side of the spectrograph’s field of view were still accurately calibrated. The calibration parameters that were used in SP-308 for all testing

are shown in Table 3.1. After the SP-308 calibration, an overall wavelength calibration was conducted using the same procedure as described in Section 3.1.1.1.

Table 3.1: Wavelength calibration parameters used for the SP-308 spectrometer during nanosecond-pulsed plasma testing.

<b>Offset</b>	
Reference Wavelength	0
Offset Value	5.90047
<b>Adjust</b>	
Reference Wavelength	579.066
Adjust Value	-0.0001197
<b>Dispersion</b>	
Focal Length (mm)	236.8
Inclusion Angle	27.55
Detector Angle	-2.37
Lower Reference Wavelength	435.833
Higher Reference Wavelength	579.066

### 3.2.2.3 Intensity Calibration

The intensity calibration took place after the wavelength calibration and was identical to the procedure described in Section 3.1.1.2 for the HR4000 spectrometer. The same 2800-K tungsten lamp was used as the reference intensity light, and the measured light and dark spectra were post-processed in MATLAB to give an intensity correction factor for each wavelength.

### 3.2.2.4 Step & Glue

Because the field of view of the three gratings in the SP-308 was at most 60 nm, a single spectrograph snapshot could not capture the entire spectral range of interest (350-750 nm). Therefore, a built-in stitching function known as “Step and Glue” was used. By giving WinSpec control over the turret movement in the spectrometer, the process of collecting a continuous spectrum that encompasses the full spectral range of the detector can be

automated. The software takes an exposure at a given wavelength range, and while the shutter is closed, moves the grating to the next position.

The step and glue data collection range was specified from 250-900 nm with a 10 nm overlap, which was then averaged for a smooth transition from one exposure to the next per the algorithm specified in the WinSpec manual [48]. The final glued spectra was comprised of 13 individual exposures.

While the wavelength calibration does not depend on the speed of the stepper motor responsible for rotating the grating from one position to the next, it does depend on the position of the grating. For best results, each position of the grating requires its own wavelength and intensity calibration. Even if the spectrometer has a good calibration at a given set of wavelengths, moving the center wavelength by moving the grating position changes the grating angle and the resultant dispersion properties. Similarly, there should be a separate intensity calibration done at each step and glue grating position.

Unfortunately, WinSpec is an older software and does not facilitate multiple calibrations during the step and glue process. That feature was implemented in Princeton Instruments' newest LightField software. As a result, the SP-308 had only a single calibration over the entire step and glue spectral range of 200-900 nm, and any potential artifacts were addressed in post-processing and data analysis. For example, spectral peaks that showed up on the edges of the spectrograph's field of view for a given grating position were given greater tolerances in the peak matching analysis process than peaks that appeared in the center.

### 3.2.3 Photodiode

A fast photodiode was used to determine the nanosecond-pulsed plasma's ionization and recombination time and to provide optical information about the repeatability of a pulsed plasma. A fast, low-light capable, ultra-low noise avalanche photodetector (ThorLabs APD430A2) was used to monitor the plasma and track its optical output over time. The

photodiode was connected to an oscilloscope to generate a voltage trace that corresponded to optical light emissions over the lifetime of the plasma.

The three main points of interest for a photodiode trace were rise time, maximum output, and fall time. Maximum light output from a plasma typically corresponded to greatest ionization and therefore the greatest electron density. Rise time was the time it took the gas discharge to rise from 10% maximum light output or electron density to 50% maximum value. Fall time was the exact reverse, the time to go from 50% to 10% maximum amplitude.

This technique is well-established: Schwirzke et al. used a fast photodiode to measure the delay between the initiation of a voltage waveform and the formation of pulsed plasma [49], and Chan and Singletary used the APD430A2 photodiode in similar experimental setups to investigate the pulse repetition rate on plasma rise time for a nanosecond-pulsed argon plasma [31, 32]. This experiment utilized the photodiode trace to determine not only plasma rise and fall time but also as additional verification that the generated pulsed plasma was repeatable. Like the spectral emission lines, the photodiode traces were tracked over several lifetimes of the pulsed plasma. Differences in the traces provided qualitative information about how the plasma changed with each pulse and if the assumption that the plasma generated per pulse is nearly identical is valid.

### **3.3 Timing Synchronization**

For collecting time-resolved data, proper timing synchronization among the pulser, ICCD-spectrometer assembly, and photodiode was extremely important. Figure 3.9 shows the timing synchronization setup used.

#### 3.3.1 Pulse Delay Generator

A Model 577 pulse delay generator from Berkeley Nucleonics Corporation was used as the master clock, and a representative timing diagram is shown in Figure 3.10. A 500-ns

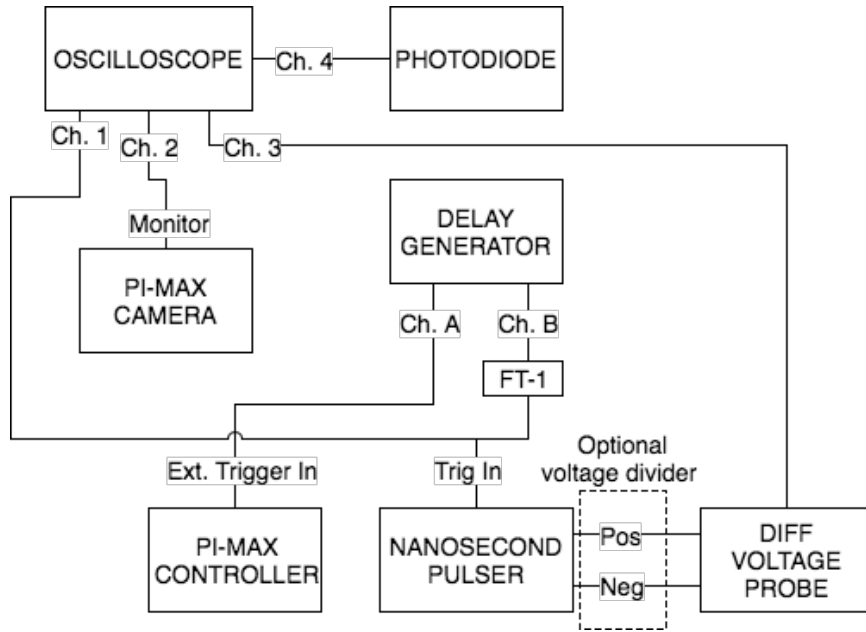


Figure 3.9: Timing synchronization setup for PI-MAX camera, spectrometer, nanosecond pulser, and photodiode.

pulse was sent to trigger the NSP as soon as the delay generator began running. The NSP continuously pulsed at  $T_0$  set by the delay generator. Another 300-ns pulse was sent to trigger the PI-MAX camera with a certain time delay  $t_{delay}$  from NSP trigger pulse. There was an inherent, constant PI-MAX time offset before the 4-ns gating signal was triggered. By forcing both the pulser and camera to trigger off the same master clock,  $t_{delay}$  could sweep across the voltage pulse to capture light emissions at different parts of the plasma evolution and thus collect time-resolved data of the plasma independent of the NSP.

### 3.3.2 Nanosecond Pulser

The pulse from the delay generator to externally trigger the NSP was not directly received by the NSP but rather by the Eagle Harbor Fiber Transmitter (FT-1). The FT-1 had a fiber optic output and a 50 $\Omega$ -terminated BNC input that required a smooth, 5-V input trigger signal, which was provided by the Model 577 [36]. From the specifications of the FT-1, the input to output time delay was approximately 30 ns but was also dependent on the length of the fiber optics cable. However, the exact delay from pulse generator trigger to NSP voltage

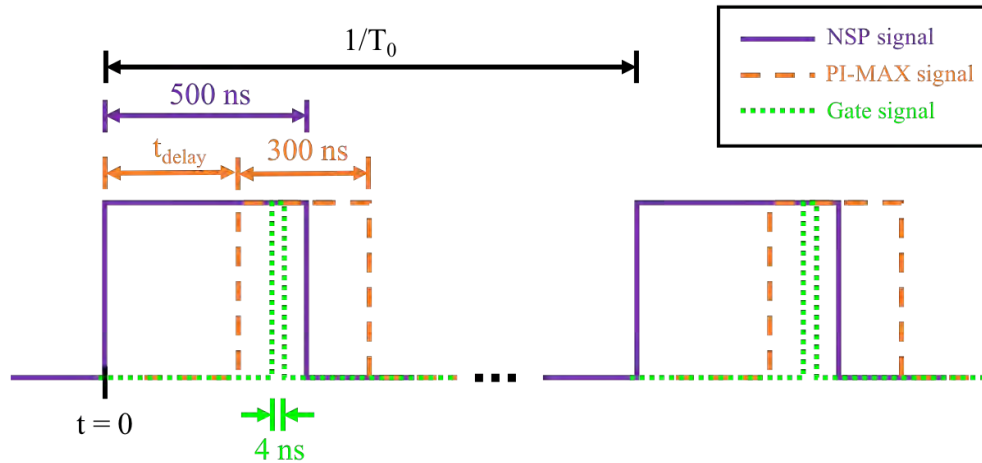


Figure 3.10: Representative timing relationship of delay generator, pulser, and PI-MAX-SP-308 assembly.

output was not important because  $t_{delay}$  of the PI-MAX was based on the measured voltage waveform, which incorporated all delays. Note that while the NSP's pulse frequency was controlled by the pulse generator, the pulse width and voltage discharge were manually set on the NSP front panel by the user.

### 3.3.2.1 Voltage Measurements

Voltage was directly measured from the pulser using a HVD3605A high-voltage differential probe from Teledyne Lecroy connected to a Teledyne Lecroy HDO6104A oscilloscope. Because the NSP was outputting voltages greater than 6 kV, which exceeded the maximum-rated voltage for the differential probe, a resistor voltage divider was implemented. Schematically shown in Figure 3.11 and experimentally shown in Figure 3.12, the final resistive voltage divider was constructed from 5 x 1000  $\Omega$  HVR RT series resistors (the first attempted voltage divider is detailed in the following paragraphs). These non-inductive, ceramic composite resistors were specifically chosen for the resistive voltage divider because of their ability to handle high-voltage pulses with low performance degradation and thermal stress [50].

Taking into account the NSP internal series resistance of 1170  $\Omega$ , a single resistor gave

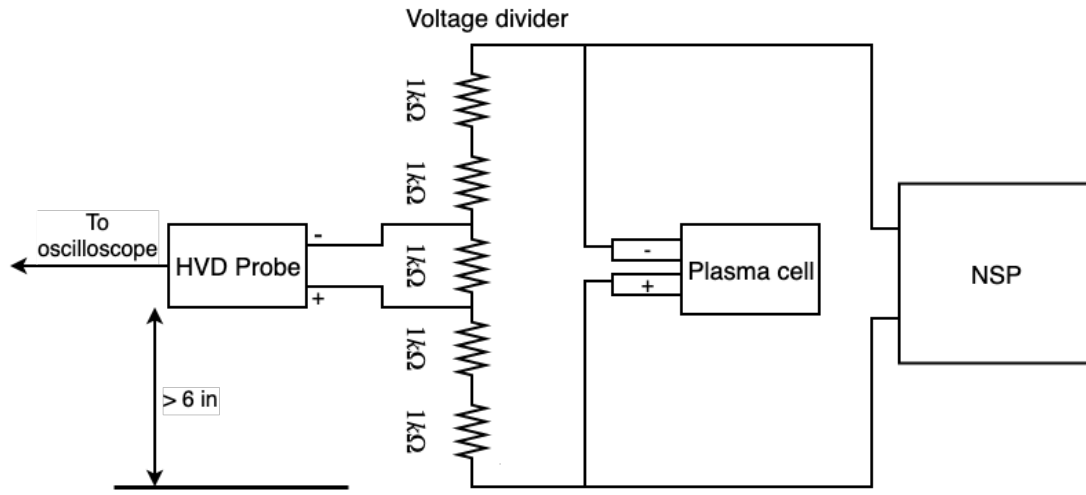


Figure 3.11: Electrical schematic of voltage divider for measuring NSP waveform, adapted from [50].

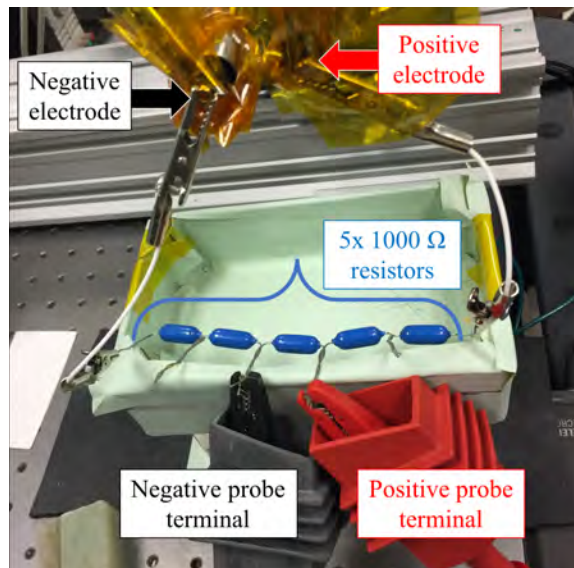


Figure 3.12: Experimental setup of the resistive voltage divider and high-voltage differential probe.

a nominal voltage division of 1:6.183. However, the probe-measured voltage across the middle resistor was approximately a 1:15 voltage division. This was due to the short 20-ns pulse width and the plasma cell load connected to the NSP pulling the actual outputted voltage down. As the NSP pulse width was increased, the voltage division was approximately a 1:12 voltage division – closer to the ideal 1:6.183; independent of the plasma cell load, a 20-ns pulse width was not enough time for the NSP to fully reach its targeted discharge voltage. Because of the research goals, the NSP pulse width could not be increased, so the actual range of output voltages that could be achieved with the NSP was smaller than 1–20 kV. While not ideal, trends in plasma properties could still be extracted from this decreased range.

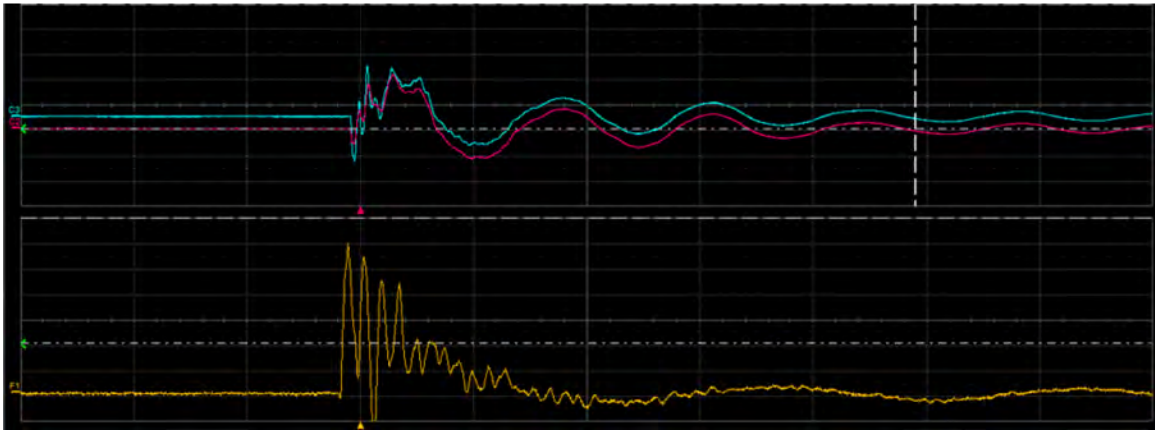
### *3.3.2.2 Mitigating Voltage Reflections*

As seen in Figure 3.13, an important part of obtaining accurate voltage measurements was minimizing the ringing and noise prevalent for high-voltage pulses. Figure 3.13a shows an example waveform of one of the first NSP voltage measurements taken. The NSP was set to 500 V, and the only load was an initial resistive voltage divider built with 10 x 100  $\Omega$  TNP10 Ohmite resistors (nominal voltage division of 1:11.17 taking into account the NSP internal resistance). Two passive probes (blue and magenta traces in the upper window) were used for the measurement; the voltage difference is shown in orange in the lower window. The clear voltage reflections in the measurement made it difficult to characterize the voltage pulse and therefore could not be used for nanosecond plasma testing.

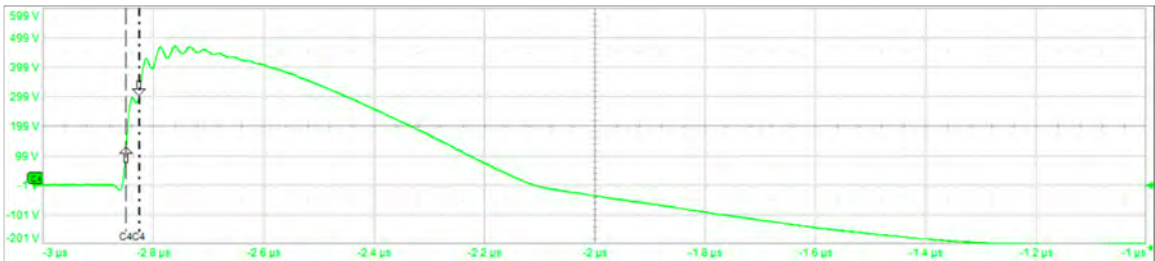
To minimize stray capacitive coupling, the power leads, voltage divider, and probes were lifted off the metal optical table by at least 6 inches. The NSP output cable length was “short” such that the propagation time of a signal through the cable was short compared to the signal’s rise time, and all diagnostics and leads were laid out so no cables crossed or looped around each other. A high-voltage differential probe instead of two passive probes was used, and the resulting measured waveform from these modifications

(without the voltage divider load) is seen in Figure 3.13b. This waveform had significantly fewer reflections after the pulse, but there was still noise on the rising edge of the pulse. This noise can be more clearly seen in Figure 3.13c, which now includes the 11.17:1 voltage divider.

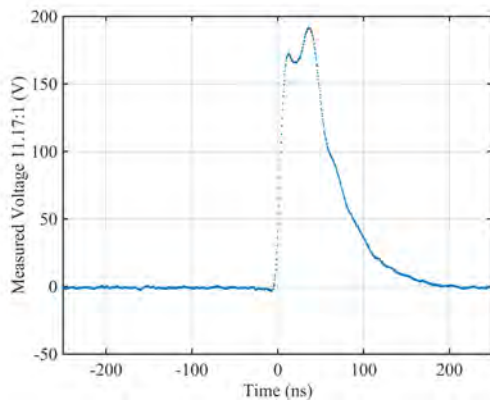
The last impactful modification was to build a low-inductive, thermally stable voltage divider. The 10 x 100  $\Omega$  Ohmite resistors were replaced with 5 x 1000  $\Omega$  HVR RT resistors – the voltage divider detailed in 3.3.2.1. The resulting voltage waveform is shown in Figure 3.13d, and this voltage pulse measurement was deemed clean enough to be used for testing. A more complete list of NSP ringing mitigations is detailed in Appendix E.



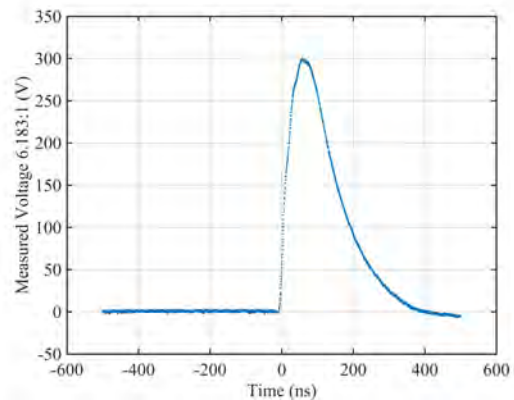
(a) Initial NSP voltage measurement, without any ringing mitigations, taken with two passive probes and a 10:1 resistive divider load. NSP set to 500 V, 20 ns; traces with 200 ns/div, 100 V/div (upper), and 20 V/div (lower).



(b) NSP voltage measurement (without resistive voltage divider) taken with a high-voltage differential probe after minimizing stray capacitive coupling in experimental setup. NSP set to 500 V, 20 ns; trace with 200 ns/div, 100 V/div.



(c) NSP voltage measurement with 11.17:1 resistive voltage divider. NSP set to 2 kV, 20 ns.



(d) NSP voltage measurement with final 6.183:1 resistive voltage divider. NSP set to 2 kV, 20 ns.

Figure 3.13: Evolution of measured NSP voltage waveforms by implementing ringing and voltage reflection mitigation strategies.

## CHAPTER 4

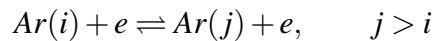
### SPECTRAL ANALYSIS

To translate the time-resolved spectral measurements into useful, time-resolved plasma properties such as electron density, electron temperature, and plasma conductivity, the population densities of the plasma must first be calculated with a valid model. Then, in conjunction with a spectral analysis method, the experimental  $n_e$  and  $T_e$  may be determined. This chapter discusses plasma equilibrium models and spectral profile fits and explains why an intensity line ratio analysis coupled with a collisional-radiative simulation software was used.

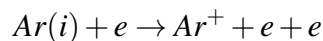
#### 4.1 Equilibrium Plasma Models

There are a large number of elementary processes that take place in a plasma and change the distribution of atoms and ions in a given energy state, and the importance of a given process depends on the model that is used to analyze the plasma. A selection of processes for an argon plasma is detailed below.

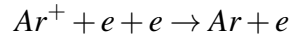
1. Electron-impact (collisional) excitation and de-excitation



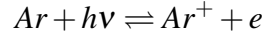
2. Electron-impact (collisional) ionization



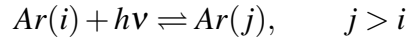
### 3. Three-body recombination



### 4. Photoionization and radiative recombination



### 5. Photoexcitation and spontaneous/stimulated emission



#### 4.1.1 Complete Thermodynamic Equilibrium

All particles (electrons, ions, and neutrals) in a plasma in complete thermodynamic equilibrium (CTE) have the same temperature such that  $T_i = T_e = T_g = T$ , and each velocity follows a Maxwell-Boltzmann distribution [1, 2]:

$$f_M(\mathbf{v}) = n \left( \frac{m}{2\pi k_B T} \right)^{3/2} \exp \left( -\frac{m(v_x^2 + v_y^2 + v_z^2)}{2k_B T} \right) \quad (4.1)$$

where  $f_M(\mathbf{v})d\mathbf{v}$  is the number of particles per volume with velocities between  $\mathbf{v}$  and  $d\mathbf{v}$ ,  $k_B = 1.38 \times 10^{-23}$  J/K is the Boltzmann constant, and  $n$  is the particle number density. In an equilibrium state, the distribution functions of the particles are not affected or altered by particle collisions.

#### 4.1.2 Local Thermodynamic Equilibrium

While it is extremely uncommon for a laboratory plasma to be in CTE, it can be in local thermal equilibrium (LTE). The plasma temperature and density may vary in space and

time, but there is a good approximation of equilibrium in a local neighborhood, and the particle distribution function at a given instant in time and point in space is described by the Maxwell-Boltzmann distribution function [1].

Derived from the first law of thermodynamics and statistical mechanics relations,  $n_a$  and  $n_b$  (i.e., the number density of particles in LTE with energies  $E_a$  and  $E_b$ , respectively) can be related by [1, 2, 51]:

$$\frac{n_a}{n_b} = \frac{g_a}{g_b} \exp\left(-\frac{E_a - E_b}{kT}\right) \quad (4.2)$$

where  $g_a$  and  $g_b$  are statistical weights (degeneracy factors) associated with  $E_a$  and  $E_b$ .

From the Boltzmann population ratio, the degree of ionization in a plasma at LTE at some temperature can be calculated without knowing the specific details of the ionization process by the Saha equation [2]:

$$\frac{n_e n_i}{n_n} = \frac{2Z_i}{Z_n a_0^3} \left(\frac{kT}{4\pi E_H}\right)^{3/2} \exp\left(-\frac{E_\infty}{kT}\right) \quad (4.3)$$

where  $n_n$  is the neutral atom density,  $Z_i$  and  $Z_n$  are partition functions,  $a_0 = \frac{4\pi\epsilon_0 h^2}{m_e e^2}$  is the Bohr radius,  $h$  is Plank's constant,  $E_H$  is the ionization energy for hydrogen, and  $E_\infty$  is the ionization energy of the atom.

The Saha equation describes the densities of particles in different states of ionization and thus the plasma composition, but it does not hold when the plasma departs from LTE, such as for low-density plasmas.

#### 4.1.2.1 Validity Conditions

The main conditions that must be met for LTE are listed below [51, 52]:

1. The velocity distribution of free electrons in the plasma is Maxwellian, and the plasma is characterized by the corresponding electron temperature  $T_e$ .

2. For all levels, including the ground state, electron-collisional rates for a given transition dominate the corresponding radiative rates.
3. Equilibrium times (i.e., the time it takes for ions to equilibrate after colliding with free electrons) in transient plasmas are short enough compared to any large changes to  $T_e$ , so a near LTE state can be established at any time. Therefore, a plasma with slow ionization and recombination rates but rapidly varying electron temperature cannot be considered as LTE.

Using the above conditions, Griem proposed a widely accepted criterion that was later modified by Numano to give the critical electron number density in  $\text{cm}^{-3}$  for LTE [51–53]:

$$n_e^* \approx 9.3 \times 10^{17} \left( \frac{E_{12}}{E_1^H} \right) \left( \frac{E_1^H}{kT_e} \right)^{1/2} \quad (4.4)$$

$E_{12}$  is the ionization energy of a given atom from ground state to the first ionized state in eV,  $E_1^H$  is the first ionization energy of hydrogen in eV,  $k$  is the Boltzmann constant in eV/K, and  $T_e$  is the predicted electron temperature in K.

#### 4.1.3 Coronal Approximation

While LTE assumes that collisional effects completely dominate radiative ones, plasmas that are described by the coronal model, like plasmas in the solar corona, are optically thin and have a low enough  $n_e$  and a high enough  $T_e$  that radiative decay rates dominate over collisional decay rates. Out of the processes listed in Section 4.1, three-body recombination, photoionization, photoexcitation, and stimulated emission are negligible. As a result, the balance in coronal approximation is between electron impact excitation and ionization and radiative de-excitation and recombination [32, 52, 54]. The coronal model is typically valid when  $n_e < 10^{10}/\text{cm}^3$ .

## 4.2 Collisional-Radiative Model

For plasmas that cannot be described by LTE or the coronal approximation, a more general method is needed to describe the plasma population and determine  $T_e$  and  $n_e$ . In collisional-radiative models (CRMs), densities of the excited states are purely determined by collisional and radiative processes, some of which are listed in Section 4.1, and the balanced rate equations are functions of plasma parameters such as  $n_0$ ,  $n_i$ ,  $n_e$ , and  $T_e$  [55]. CRMs have the advantage of being applicable to not only equilibrium plasmas but also ionizing and recombining plasmas – no specific equilibrium is assumed [54]. However, most CRMs do assume a Maxwellian electron velocity distribution, which is true for most strongly, medium, and weakly ionized plasmas and not true for typical gas discharges [55–57].

CRMs solve coupled differential equations that describe the densities of an excited state  $j$  in the plasma with collisional and radiative processes [55]:

$$\frac{\partial n(j)}{\partial t} + \nabla \cdot (n(j)\omega_p) = \left( \frac{\partial n(j)}{\partial t} \right)_{c,r} \quad (4.5)$$

All changes in excited-state population density due to collisional ( $c$ ) and radiative ( $r$ ) processes are encompassed on the right-hand side of the equation. The density of the ground state ( $j = 1$ ) can be approximated by the ideal gas law since the effect of collisional and radiative processes on argon atom density  $n_0$  is negligible [54, 57]:

$$n(1) = \frac{p}{kT_g}$$

where  $p$  is the gas pressure and  $T_g$  is the gas temperature.

The populating and depopulating processes typically change the densities of the excited states significantly larger than the time derivative and the convective and diffusive transport

terms. Therefore, the following assumptions can be made to simplify Equation 4.5:

$$\frac{\partial n(j)}{\partial t} = 0; \quad \nabla \cdot (n(j)\omega_j) = 0$$

What remains is to solve this set of coupled linear rate equations describing electronic transitions due to collisional and radiative processes and calculate  $n_e$  and  $T_e$ .

More detailed discussions and reviews of CRMs and the major collisional and radiative processes for different argon excited states are found in the literature [44, 51, 54–61].

### 4.3 Spectral Line Fits

With OES,  $n_e$  can be directly determined from peaks of the measured spectra. However, as seen in Figure 4.1, the accuracy of this method is highly dependent on how well a given fit profile (i.e., Gaussian, Lorentzian, single-Voigt, etc.) matches the data profile for a peak [33, 62]. For the best representation of the measured spectra, different line width broadening effects need to be considered and included in the fit.

One of the broadening effects that is commonly analyzed for spectral lines of plasmas is Stark broadening. This type of pressure broadening is caused by the Stark effect, when spectral lines are split and wavelength-shifted due to an external electric field caused by the charged particles in the plasma. The electrons and ions in a plasma perturb a radiating particle and broaden the spectral lines through an impact approximation or a quasi-static approximation [51, 63].

Stark broadening analysis is a technique often used to calculate  $n_e$  for a plasma by primarily looking at how Stark broadening affects the  $H_\alpha$  and  $H_\beta$  Balmer lines – those line broadenings are obvious, and tabulated experimental data regarding those transitions are well-established in literature [44, 64, 65]. For experiments with pure argon gas flows, there are minute amounts of impurities in the discharge from  $H_2O$  in the vacuum chamber walls that are enough for H atom emission lines to appear in the spectra, so a Stark broadening

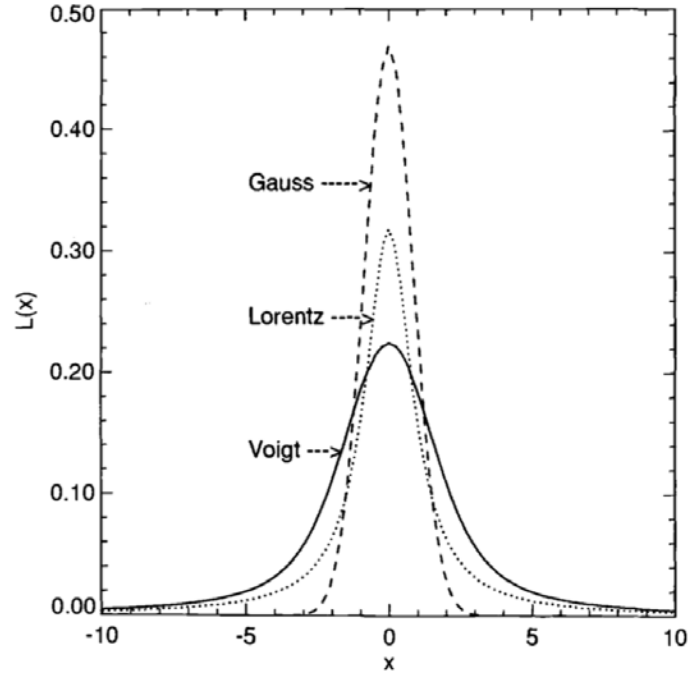


Figure 4.1: Comparison of a normalized Gaussian and Lorentzian profile with equal FWMW = 2 and a Voigt profile from the convolution of the Gaussian and Lorentzian, pulled from [51].

analysis may still be done on the hydrogen to characterize the plasma.

While much less obvious, Stark broadening for specific argon transitions have also been done, but those methods are only valid at high electron densities ( $> 10^{13} \text{ cm}^{-3}$ ) [58, 65, 66]. Below those densities, other broadenings may dominate such as:

- Doppler broadening: the broadening of spectral lines due to the random motion of atoms in a source that gives a Gaussian profile [63]
- Instrumental broadening: the systematic broadening of lines from a spectrometer that gives an approximately Gaussian profile [64]
- van der Waals and resonance broadenings: collisions between radiating and perturbing particles of the same species results in a Lorentzian profile [62]

Due to these broadening effects, creating the appropriate fit for experimental spectral data and calculating  $n_e$  for the plasma becomes complicated.

#### 4.4 Line Ratio Analysis

An alternative analysis for determining  $n_e$  and  $T_e$  is to take ratios of spectral line intensities. This method removes the difficult task of accurately determining all the line broadening parameters and only involves intensity ratios of different wavelengths. Calculated  $n_e$  and  $T_e$  values from the line ratio analysis have been similar to those calculated directly from a spectral line fit [44, 58].

Under CTE or LTE, the intensity ratio between two spectral lines directly gives the electron temperature of the plasma [7, 67]:

$$\frac{I_1}{I_2} = \frac{A_1 g_1 \lambda_2}{A_2 g_2 \lambda_1} \exp\left(-\frac{E_1 - E_2}{kT_e}\right) \quad (4.6)$$

where  $I$  is the relative or absolute intensity from an emission spectral line. Relative intensity is typically used to avoid the necessity of a lengthy absolute calibration. Equation 4.6 is a function of tabulated Einstein coefficients ( $A$ ) and tabulated multiplicity ( $g$ ), the wavelengths ( $\lambda$ ), the energy associated with the line ( $E$ ), and the electron temperature ( $T_e$ ).

Rearranging Equation 4.6 gives:

$$\ln \frac{I_1 A_2 g_2 \lambda_1}{I_2 A_1 g_1 \lambda_2} = -\frac{1}{kT_e} (E_1 - E_2) \quad (4.7)$$

The slope of the semi-log plot of Equation 4.7 is exactly  $-\Delta E/T_e$  where  $T_e$  is the electron temperature in eV. Electron temperature of the plasma can therefore be directly calculated from experimental spectral lines using the Boltzmann relations. However, as previously indicated, using the Boltzmann plot for calculations requires the plasma to be in CTE or LTE [68]. If the plasma is in partial LTE or is in non-equilibrium, correction factors must be added to the Boltzmann equation, or a different model like a CRM must be used. From a CRM, theoretical spectral line intensities can be calculated as a function of plasma

parameters, and the measured spectral intensity line ratios can be matched to the calculated line ratios to determine the experimental  $n_e$  and  $T_e$  [56].

Using Equation 4.4 and  $E_{12} = 15.76$  eV for argon,  $n_e^* \approx \mathcal{O}(10^{19})$  cm<sup>-3</sup> for LTE to be valid. Based on similar plasmas in literature and the target electron density needed for the VLF plasma antenna [31, 32], the experimental electron density was predicted to be  $\mathcal{O}(10^{10} - 10^{12})$  cm<sup>-3</sup>  $\ll n_e^*$ . LTE thus does not apply to this plasma, but  $n_e$  is also too high for the coronal model to be used, so this plasma must be analyzed with a CRM. For these experiments, the intensity ratio of emission lines from the ICCD-spectrometer measurements were matched to results generated from the collisional-radiative spectra simulation software PrismSPECT.

#### 4.5 PrismSPECT

PrismSPECT is commercially available software that uses a CRM and user-based inputs such as gas mixture, background gas pressure, plasma geometry, and electron temperature to generate theoretical emission spectra for LTE and non-LTE plasmas. As part of its CRM, PrismSPECT takes into account the following atomic processes: collisional ionization, recombination, excitation and de-excitation, photoionization and stimulated recombination, photoexcitation and stimulated emission, spontaneous decay, radiative recombination, autoionization, and electron capture [69]. It also includes Doppler and Stark broadening in its generated spectra line profiles and can model plasmas with non-Maxwellian electron distributions. The theoretical spectra were used to obtain the “ideal”  $n_e$  and  $T_e$  values, which were used to anchor the experimental line ratio values. By comparing the simulated emission spectra to the measured spectra, the electron temperature and electron density of the experimental plasma cell could be found.

Because each generated spectra was compared to a measured, pulsed plasma spectra averaged over the gate time of 4 ns, the PrismSPECT simulations were chosen to be steady-state. A zero-width, optically thin (i.e., the mean free path is greater than the

characteristic plasma dimension), non-LTE plasma was assumed, so photoionization, stimulated recombination, photoexcitation, and stimulated emission were neglected [52]. As suggested in literature, the simulations used a single-temperature Maxwellian electron distribution [52, 56]. The density model was calculated by fixing an argon pressure in the plasma cell, assuming the ideal gas law, and allowing the gas temperature to respond within the set volume of the plasma cell. PrismSPECT included a variety of spectra modeling modes, but low-temperature spectroscopy was used since the other modes were more useful for hot plasmas such as those seen in fusion reactor experiments. Results from each simulation included the generated emission spectra, ion population, and line intensities for user-selected wavelengths.

**CHAPTER 5**  
**TIME-AVERAGED PLASMA DISCHARGE**

A series of steady-state plasma tests and time-averaged pulsed plasma tests were conducted to gain experience with the PrismSPECT software and to verify the usability of the experimental setup and line ratio analysis before tackling the intricacies of time-synchronizing the equipment. This chapter discusses the generation of a steady-state argon plasma discharge and a pulsed argon plasma discharge at 1-Torr argon and corresponding results from the HR4000 spectrometer. The following chapter details the setup and results from the time-resolved, nanosecond-pulsed plasma tests. A summary of the different test setups that were conducted and their purposes are shown in Table 5.1.

<b>Test Group</b>	<b>Type of plasma</b>	<b>Pulser</b>	<b>Spectrometer</b>	<b>Spectra Measurement</b>
A	Steady-state	N/A	HR4000	Time-averaged
B	Nanosecond-pulsed	FID	HR4000	Time-averaged
C	Nanosecond-pulsed	Eagle Harbor	PI-MAX/SP-308	Time-resolved

(a) Description of test groups.

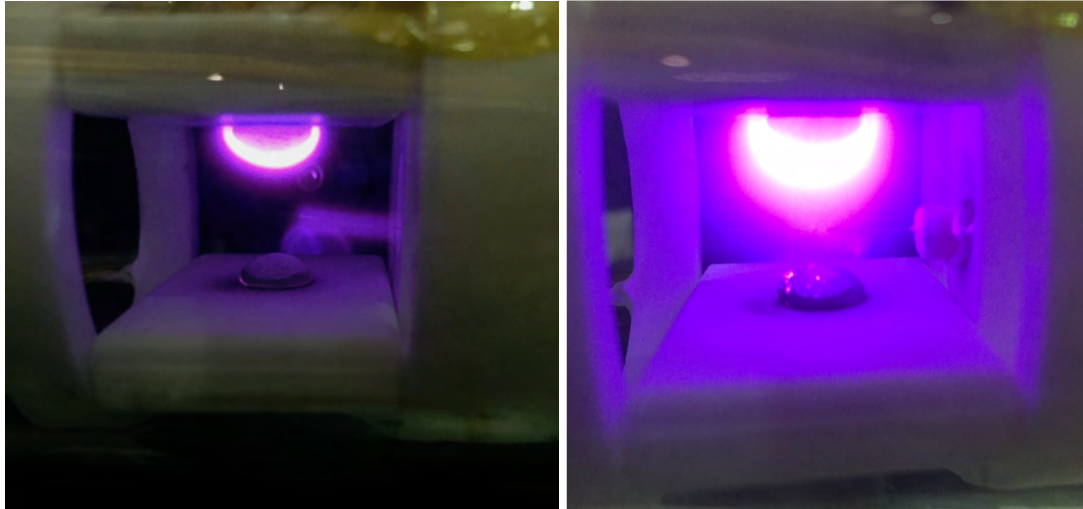
<b>Test Group</b>	<b>Purpose</b>
A	PrismSPECT experience; verify line ratio analysis
B	Pulser experience; verify line ratio analysis for pulsed plasmas
C	Time-resolved data on nanosecond-pulsed plasmas

(b) Purpose of test groups

Table 5.1: Summary of the three main test groups.

### 5.1 Steady-State Plasma Discharge

For steady-state plasma tests (Test Group A in Table 5.1), the Lambda power supply was varied from an initial plasma generation voltage of  $\sim 275$  V to 600 V. An argon discharge at two different voltages can be seen in Figure 5.1. Note the more confined plasma glow for



(a) 1 Torr, 287 V, 0.006 A.

(b) 1 Torr, 530 V, 0.011 A.

Figure 5.1: DC argon plasmas at two different operating conditions.

the lower discharge voltage condition compared to the larger, brighter glow of the 530-V discharge.

### 5.1.1 OES Analysis Overview

OES was used for the steady-state plasma discharges, and the experimentally-determined line ratios for Ar I (neutral argon) and Ar II (argon ions with +1 charge) lines were compared to PrismSPECT simulations, similar to the experiments and analysis conducted by Singletary [32]. Figure 5.2 represents a sample argon spectra from the HR4000 spectrometer at 450-V discharge and 100-ms integration time.

Strong Ar I and Ar II lines in the OES-obtained spectra were selected for intensity line ratio calculations. Because the HR4000 spectrometer had a wavelength resolution of 0.75 nm FWHM [37], Ar I and Ar II lines at least 2 nm away from other peaks in the NIST database were chosen to prevent overlapping peaks, where multiple line intensities would be incorrectly summed as a single intensity. Table 5.2 lists the selected spectral lines for line ratio calculations of the steady-state plasma. The relative intensity of a wavelength is defined by NIST as a qualitative description of what the emission spectrum

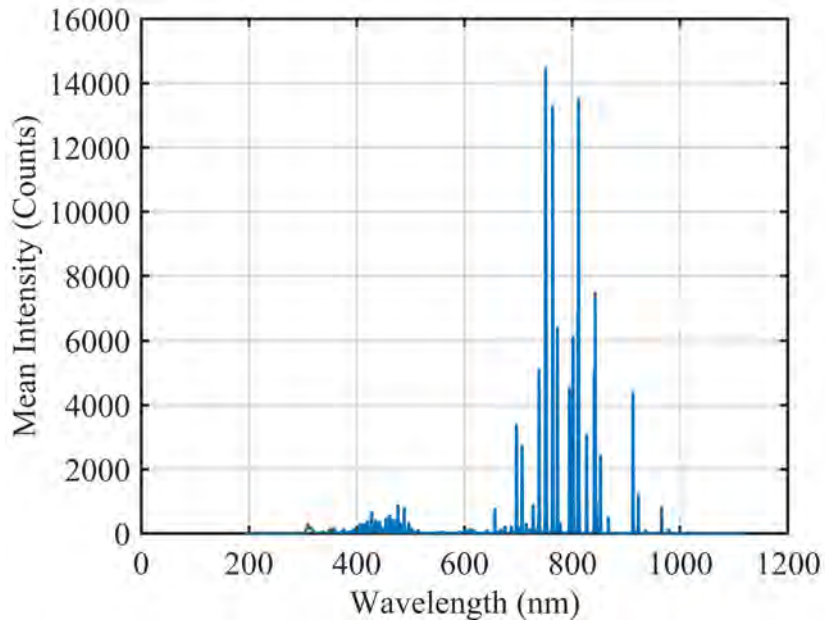


Figure 5.2: Argon emission spectra at 450 V, 1 Torr.

of the wavelength looks like compared to other wavelengths [38]. The larger the relative intensity value, the stronger that line is for the given emission spectrum.

Table 5.2: Selected argon emission spectral lines for line ratio calculations of steady-state plasma [32].

Species	Vacuum Wavelength (nm)	Relative Intensity
Ar I	738.6014	10000
Ar I	763.7208	25000
Ar I	912.5471	35000
Ar II	454.6326	1738
Ar II	465.9205	1445
Ar II	476.6197	2344

#### 5.1.1.1 Experimental Intensities

While it was less crucial that a spectral profile and all its broadening correction terms exactly fit the measured data points, an appropriate peak finder was still necessary. After subtracting out the mean dark spectrum from the mean data spectrum in a given test and

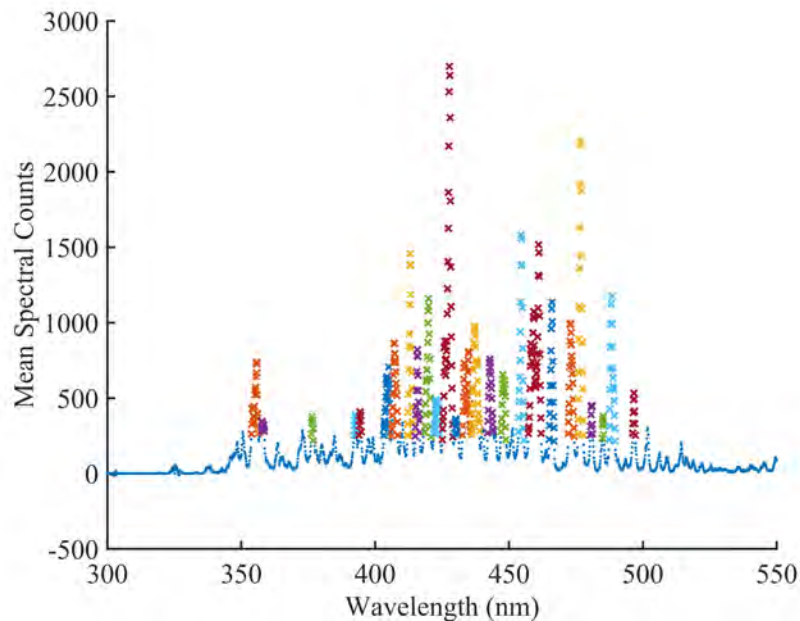
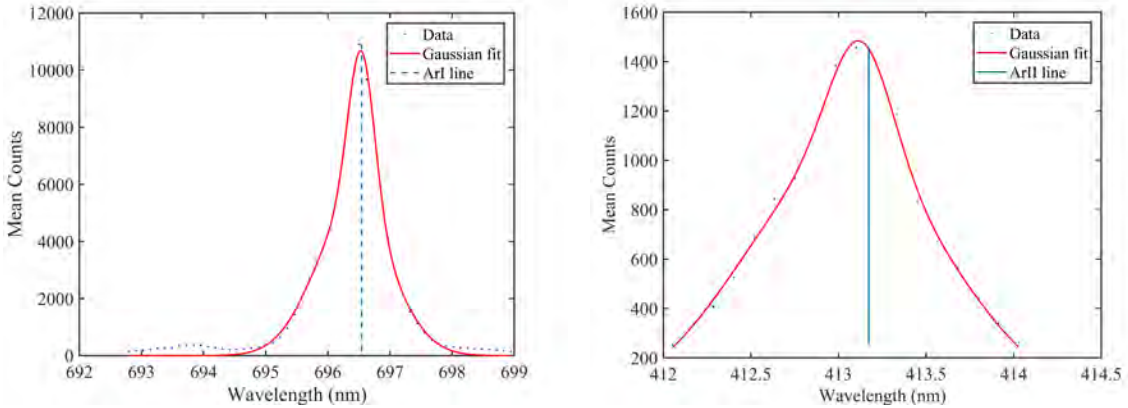


Figure 5.3: Separate peaks (of mostly Ar II lines) shown in a sample argon test spectra from 300-550 nm.

applying the wavelength and intensity corrections per Sections 3.1.1.1 and 3.1.1.2, a MATLAB code was used to find all the peaks (i.e., a cluster of five or more points with intensities  $> 85\%$  of the mean) in the spectrum. This custom, peak-finding code prevented any stray, high-intensity points from being identified as a peak. As seen in Figure 5.3, each color of an almost vertical line of x's corresponds to a peak. Each individual peak was then fitted with a Gaussian curve, and the maximum intensity for that given peak was determined. Figure 5.4 shows two sample peaks with appropriate Gaussian fits whose center corresponds to a strong argon neutral and a strong argon ion line. Using the Ar II line as an example, the experimental intensity corresponding to the NIST-approved 413.2 nm line is the data intensity value interpolated at the Gaussian center of 413.1 nm. Additional details about the data processing can be found in Appendix C.

### 5.1.2 PrismSPECT Simulations

PrismSPECT simulations were run at 1-Torr argon and with an electron temperature range from 0.1-4 eV. Two sets of PrismSPECT simulations were run when calculating line ratios



(a) Gaussian fit ( $\mu = 696.54$  nm) of Ar I 696.5 nm line. (b) Gaussian fit ( $\mu = 413.13$  nm) of Ar II 413.2 nm line.

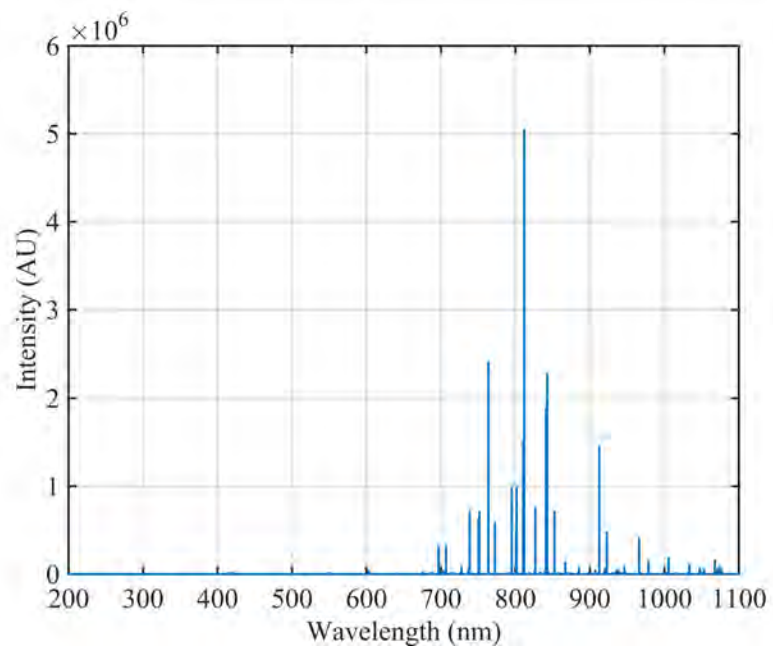
Figure 5.4: Finding best Gaussian fits to data (from a double Gaussian MATLAB fit) by comparing Gaussian center to NIST Ar I and Ar II emission wavelengths.

for each experimental plasma. The first simulation covered a wide range of electron temperatures at low resolution (0.1 eV). The second simulation ran with the same input parameters but covered a narrower range of electron temperatures, as determined by the first runs, at a higher resolution (0.01 eV) for a more precise line ratio match.

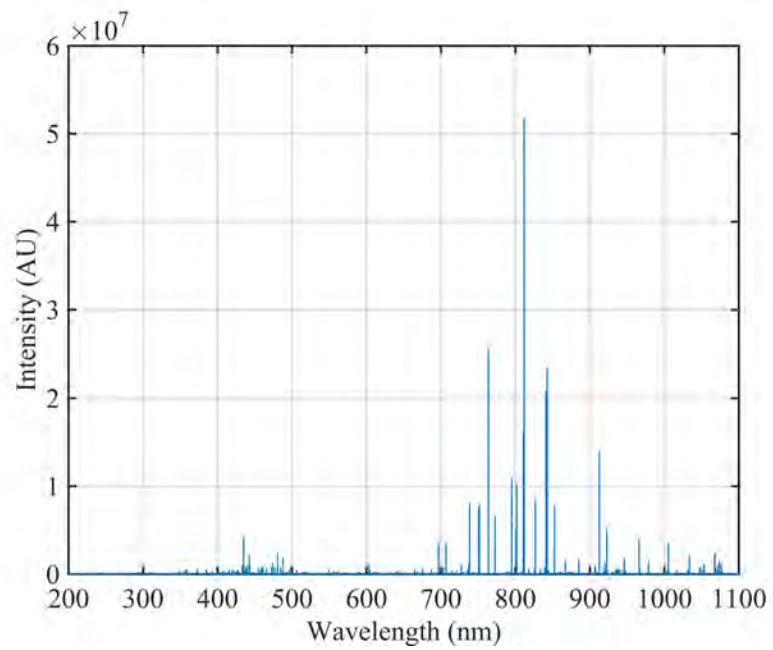
As seen in Figure 5.5, sweeping input  $T_e$  values in PrismSPECT yielded different output plasma emission spectra. The 1.5-eV spectra had significantly more and stronger emission lines in the 200-400 nm range, which indicated a higher population of argon ions in the plasma. The 1-eV spectra was dominated by neutral argon species whose emission lines were centered around 800 nm. Figure 5.6 shows how the argon neutral and ion populations change as a function of electron temperature. As expected, the neutral population gave way to higher Ar+1, +2, and +3 ions as  $T_e$  increased. Similarly, PrismSPECT calculated electron density as a function of electron temperature (Figure 5.7), which rapidly increased until it equilibrated  $\sim 5 \times 10^{14} \text{ cm}^{-3}$ .

### 5.1.3 Line Ratio Comparison

The wavelengths in Table 5.2 were used for line ratio calculations, and the specific line ratio wavelengths (an Ar I line with an Ar II line) were chosen based on ratios that were



(a) 1-eV emission spectra.



(b) 1.5-eV emission spectra.

Figure 5.5: Simulated argon emission spectra from PrismSPECT for two different electron temperature plasmas at 1 Torr.

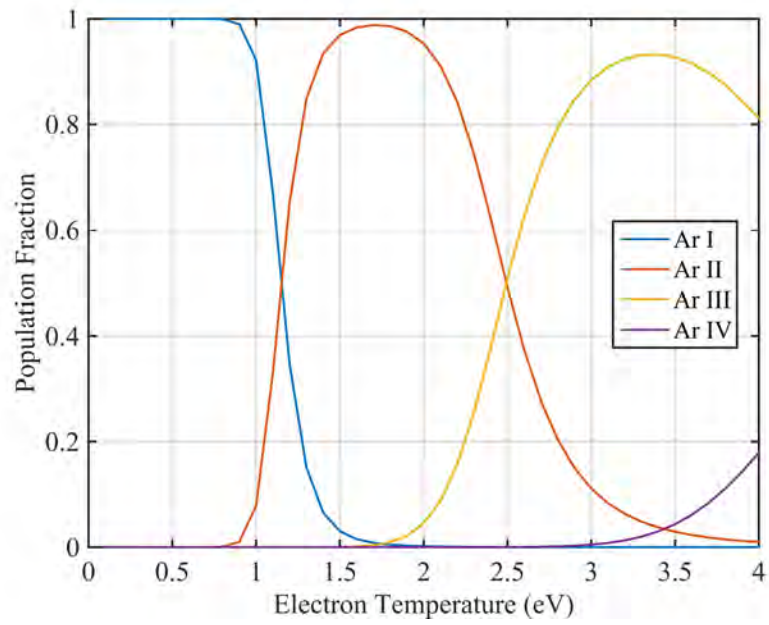


Figure 5.6: Evolution of argon neutral and ion population with electron temperature in PrismSPECT at 1 Torr.

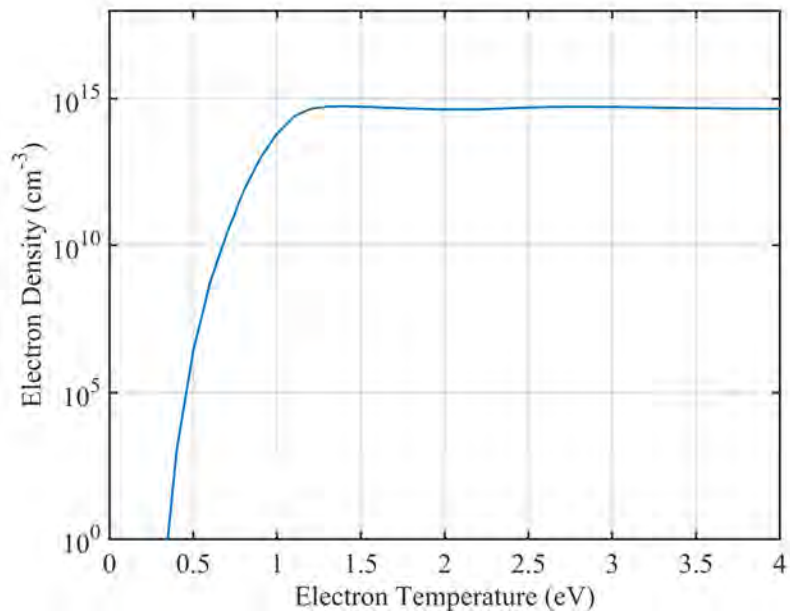


Figure 5.7: Plasma electron density as a function of electron temperature in PrismSPECT at 1 Torr.

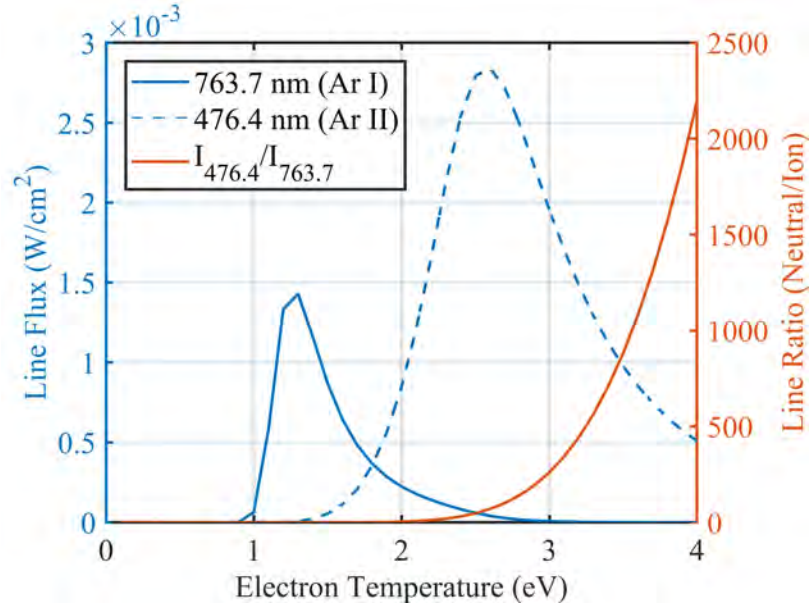
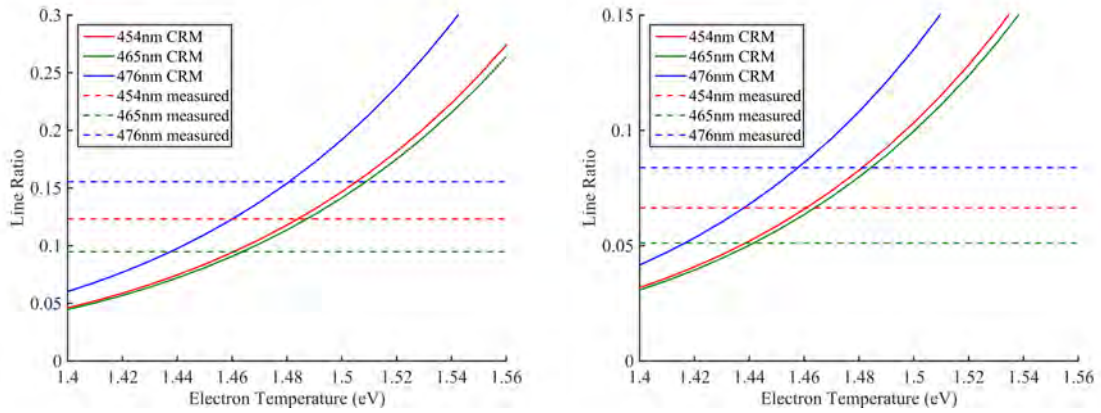


Figure 5.8: PrismSPECT simulated emission line intensity and line ratio as a function of electron temperature at 1 Torr.

most sensitive to electron temperature. PrismSPECT had a built-in line intensity viewer that tracked a wavelength's emission line as the plasma simulation inputs were varied as well as a built-in intensity ratio tracker. Figure 5.8 shows the PrismSPECT evolution of two selected lines and their intensity ratio as electron temperature is varied. Multiple line ratios from OES data were calculated and compared to those from PrismSPECT to determine an averaged electron temperature and electron density for the experimental plasma.

For example, two line ratio analyses were conducted for a 450-V discharge test. Figure 5.9 shows each of the experimental intensity line ratios (dotted lines) plotted against the PrismSPECT simulation sweep (solid lines). The 763.72 nm line was not used since it was not picked up as a strong line in the OES data. The average of the two line ratio results yielded  $T_e = 1.46 \text{ eV} \pm 0.014 \text{ eV}$  and an average electron density of  $5.46 \times 10^{14} \text{ cm}^{-3} \pm 2.80 \times 10^{12} \text{ cm}^{-3}$ . The results trended with those from Singletary [32], and the low variation indicated good consistency between different chosen wavelengths and between the experimental and PrismSPECT line ratio calculations.

Due to uncertainties in the line-fitting procedure (5% – 10%), instrument broadening



(a) Ratios of Ar II lines to 738.6 nm Ar I line. (b) Ratios of Ar II lines to 912.5 nm Ar I line.

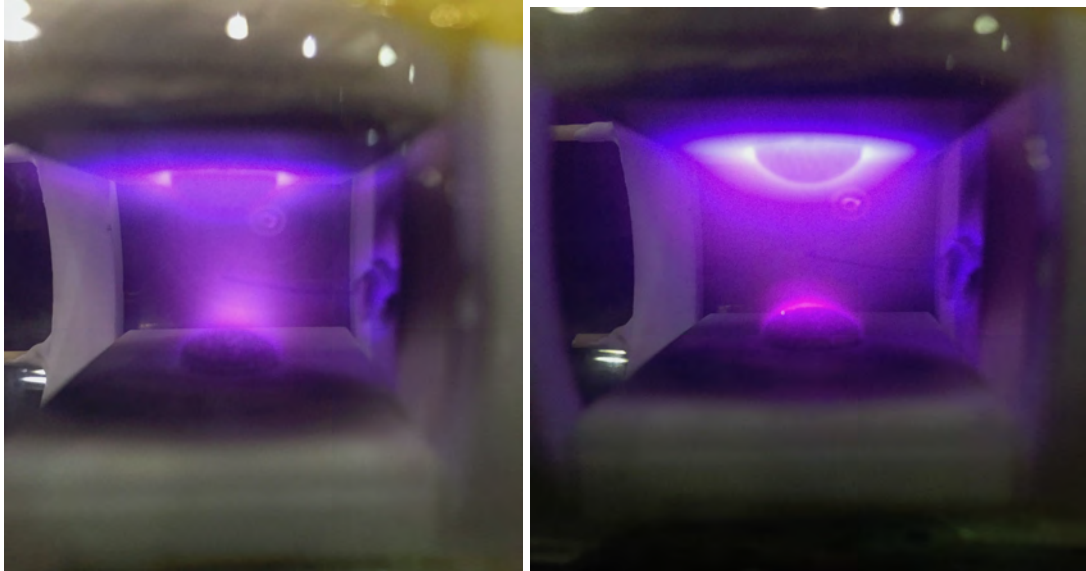
Figure 5.9: Line ratio comparisons between steady-state experimental data and PrismSPECT simulations to calculate electron temperature.

(1%), CRM rate coefficients ( $\sim 10\%$ ), and density of the ground-state argon, line ratio methods could have uncertainties as high as  $35\% - 50\%$  for  $n_e$  and  $40\% - 50\%$  for  $T_e$  [44, 56, 58]. Uncertainties from the PrismSPECT line ratio analysis were predicted to be lower. PrismSPECT's energy level structure and oscillator strengths come directly from NIST experimental data, so the simulated intensities of strong transitions for LTE and near-LTE plasmas may be  $< 1\%$  [69]. While the uncertainty increases for non-LTE plasmas, having a significantly less uncertain model for the theoretical intensity drops the uncertainty in line-ratio-calculated  $n_e$  and  $T_e$ . A more detailed breakdown of uncertainties is described in Section 6.5.5.

## 5.2 Pulsed-Plasma Discharge

The following sections discuss the time-averaged (not time-resolved) results of the pulsed plasma discharge from OES (Test Group B in Table 5.1). As described in Section 2.3, the FID was used to generate this series of nanosecond-pulsed plasma tests, and its output voltage was set to 500 or 1000 V at a pulse width of 5 ns and a pulse frequency of 10 or 50 kHz. The resulting pulsed, argon discharge was no longer confined to a glow around a single electrode but instead spanned across the two electrodes in a plasma column. Figure

5.10 illustrates the plasmas created at a discharge voltage of 1 kV and pulsed with a pulse width of 5 ns and a repetition frequency of 10 kHz and 50 kHz. Note that the 50-kHz plasma has a much stronger glow around the positive (upper) electrode, and the 50-kHz plasma takes up more volume between the electrodes than the 10-kHz plasma.



(a) 1 Torr, 1000 V, 5 ns, 10 kHz.

(b) 1 Torr, 1000 V, 5 ns, 50 kHz.

Figure 5.10: Pulsed argon plasma discharge “column” across two electrodes 1 cm apart at two pulse repetition frequencies.

### 5.2.1 OES Analysis Overview

OES data was taken with the HR4000 spectrometer for these nanosecond pulsed discharges. However, the integration time (150-300 ms) of the spectrometer was significantly greater than 5 ns, so the emission spectra did not represent a time-resolved spectra/pulse. The spectra, and therefore the plasma parameters obtained from the spectra, were averaged over 30000-60000 pulses per scan. It was assumed that the average plasma parameters from a spectral scan was also representative of the parameters over a single pulse. Figure 5.11 illustrates the averaged spectra at 300-ms integration time over 20 scans for the test conditions of Figure 5.10.

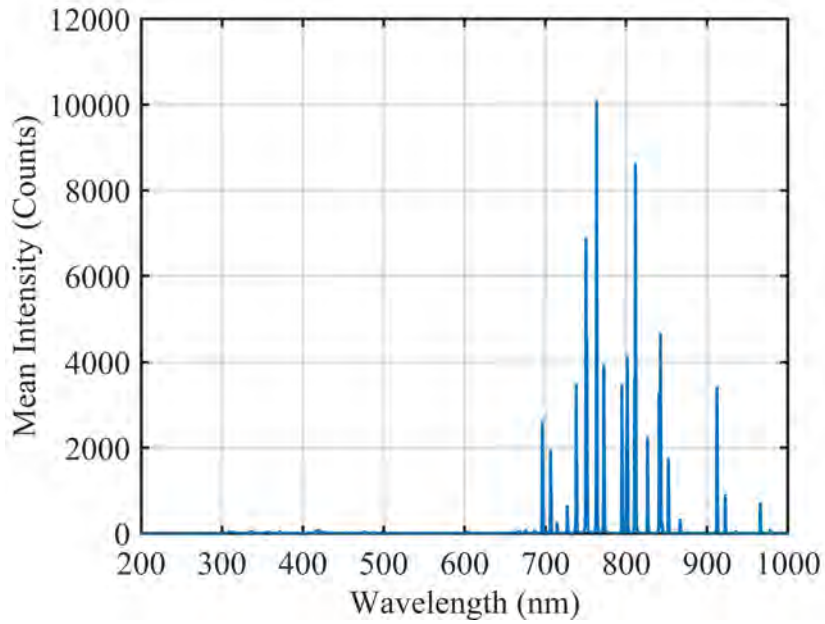
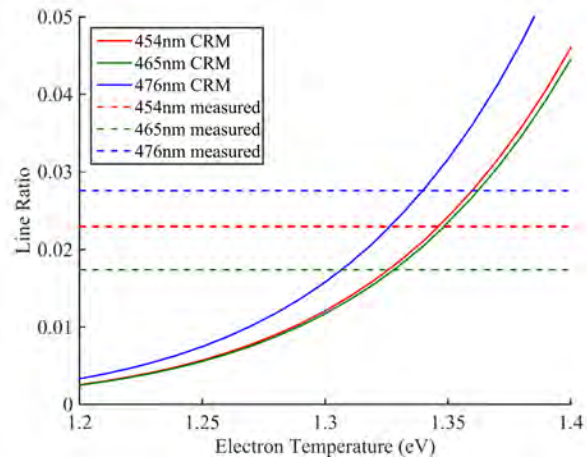


Figure 5.11: Pulsed argon emission spectra at 1000 V, 5 ns, 10 kHz and taken at 300-ms integration time.

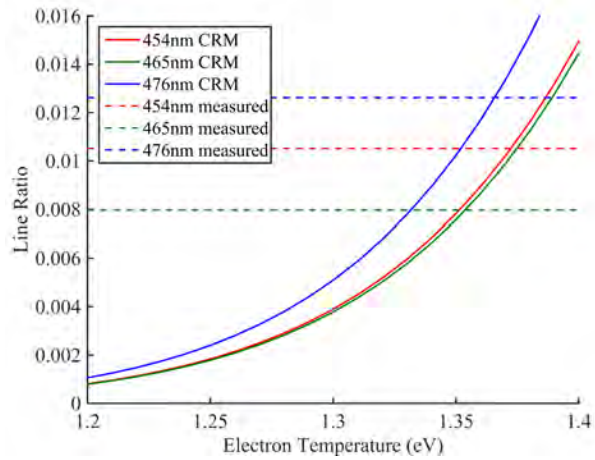
### 5.2.2 Line Ratio Comparison

Three line ratios analyses were conducted, and comparison of the experimental plasma with the simulated PrismSPECT results indicated  $n_e = 1.31 \text{ eV} \pm 0.062 \text{ eV}$  and an average electron density of  $5.34 \times 10^{14} \text{ cm}^{-3} \pm 3.23 \times 10^{13} \text{ cm}^{-3}$ . Figure 5.12 shows the three experimental intensity line ratios plotted against the PrismSPECT simulation sweep. The low variation in electron temperature again indicated that comparing the experimentally calculated OES line ratios to the simulation-generated PrismSPECT line ratios was consistent across selected wavelengths.

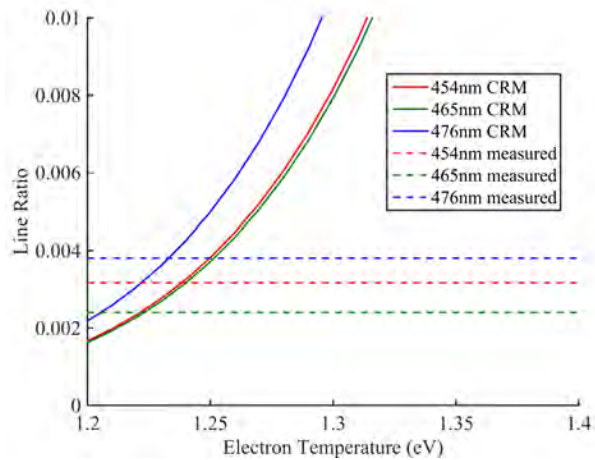
Table 5.3 summarizes the measured electron temperature and electron density values for the selected steady-state and pulsed plasma tests. Surprisingly, increasing to 50 kHz in pulse repetition frequency did not have a large effect on either  $T_e$  or  $n_e$  per line ratio calculations, but this could be primarily due to the fact that both 10 kHz and 50 kHz spectra were averaged over 100s of milliseconds, so any spectral differences on the nanosecond scale were averaged out.



(a) Ratios of Ar II lines to 738.6 nm Ar I line.



(b) Ratios of Ar II lines to 763.7 nm Ar I line.



(c) Ratios of Ar II lines to 912.5 nm Ar I line.

Figure 5.12: Line ratio comparisons between pulsed experimental data and PrismSPECT simulations to calculate electron temperature.

Table 5.3: Summary of time-averaged electron temperature and electron density measurements for different pulsed plasma conditions using OES line ratio calculations.

<b>Analysis</b>	<b>Plasma Conditions</b>	<b>Average <math>T_e</math> (eV)</b>	<b>Average <math>n_e</math> (<math>\text{cm}^{-3}</math>)</b>
Line ratio	450 V Steady	1.46	$5.46 \times 10^{14}$
Line ratio	1000 V, 5 ns, 10 kHz	1.27	$5.17 \times 10^{14}$
Line ratio	1000 V, 5 ns, 50 kHz	1.31	$5.34 \times 10^{14}$

## CHAPTER 6

### NANOSECOND-PULSED PLASMA DISCHARGE

This chapter presents the main bulk of the research for this dissertation. It details the series of nanosecond-pulsed plasma tests that were conducted (Test Group C in Table 5.1), how the time evolution of electron temperature and electron density changed with operating conditions, and the uncertainties that were associated with the results.

#### 6.1 Experimental Parameters

The main experimental parameters modified to see how plasma behavior, electron number density, and electron temperature responded are described below, and Table 6.1 summarizes the range of test values for each experimental parameter:

1. *Pressure*: Pressure affects both ionization and recombination rates, so an ideal pressure range is low enough for argon neutrals to be ionized at a reasonable breakdown voltage but high enough to facilitate rapid recombination.
2. *Discharge Voltage*: Discharge voltage impacts the type and shape of plasma generated.
3. *Repetition Frequency*: The frequency of the pulser affects ionization and recombination times as well as the species generated within the plasma.

Table 6.1: Range of values tested for experimental parameters.

<b>Pressure (Torr)</b>	<b>Discharge Voltage (kV)</b>	<b>Pulser Frequency (kHz)</b>
1-3	8-20	0.5-8

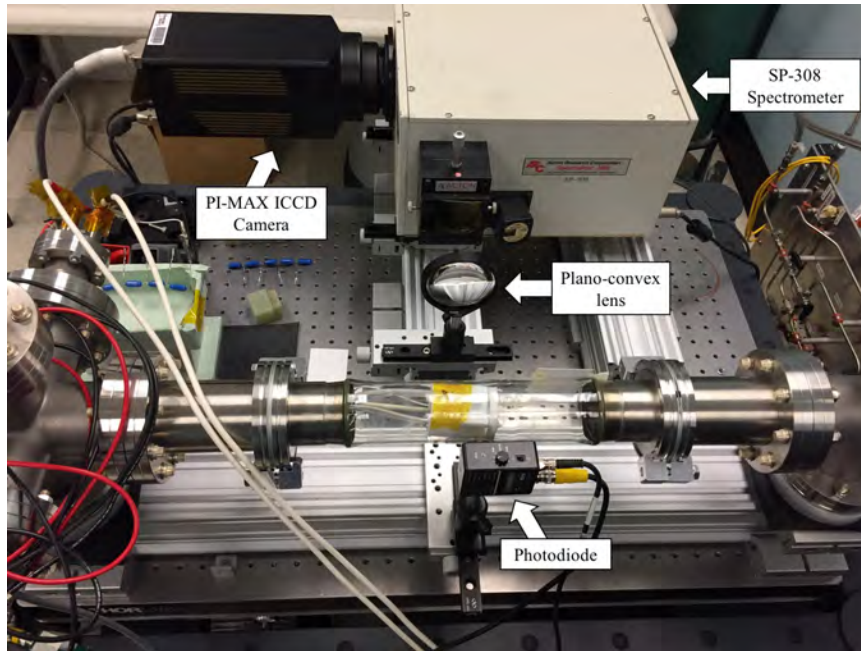


Figure 6.1: Complete experimental setup with all diagnostics and time-synchronization equipment.

## 6.2 Experimental Overview

### 6.2.1 Optical Setup

A large concern when setting up this experiment was ensuring that there would be enough emission light getting to the ICCD/spectrometer assembly at the 4-ns gate time, even with a maximum gain of 255. This concern was mitigated through a combination of hardware setup and camera functionality. As seen in Figure 6.1, a large, N-BK7 plano-convex lens ( $\varnothing 75.0$  mm,  $f = 85.0$  mm) was placed in between the plasma cell and the camera/spectrometer assembly to gather and focus a greater amount of emitted light into the spectrometer. Optical rails and carriages were installed for faster and more precise alignment of the plasma cell, lens, ICCD/spectrometer assembly, and photodiode.

The lens significantly boosted emission intensities seen by the spectrometer, such that peaks were easily seen with a 100-ns gate time. The last adjustments needed to drop the camera gate time to 4 ns involved changing the way an exposure was taken. Initially, the

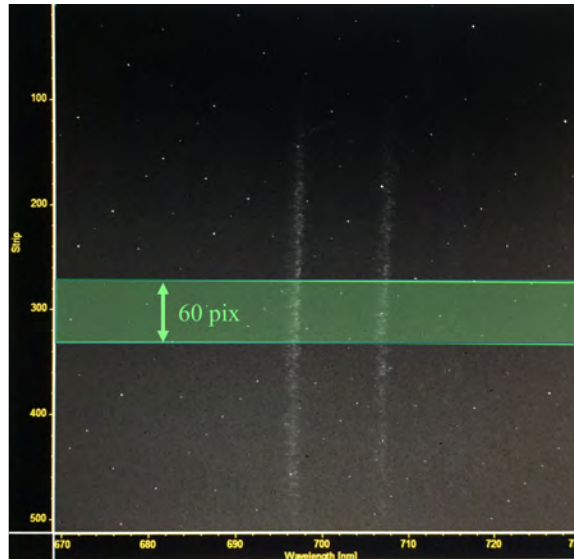


Figure 6.2: Example ROI with a 60 pixel bin height.

camera was commanded to take 20 spectra for every desired delay time. This meant that there would be a single exposure for every camera gate command, and the gate command would be repeated 20 times. However, at low gate times such as 4 ns, the intensity counts for the emission spectra were so low that all but two or three strong neutral peaks were indistinguishable from the noise.

The first adjustment was to set a region of interest (ROI) instead of using the full 512 x 512 CCD array on the PI-MAX. The pixels were binned in the y-direction to improve signal-to-noise ratio (SNR). By utilizing the Easy Bin option in WinSpec, a chip-wide ROI was defined as seen in Figure 6.2. This generated a single spectrum with much higher intensity readouts per wavelength and more clearly defined peaks than before.

In addition to the normal spectrometer software calibration described in Section 3.2.2.2, a ROI offset also needed to be defined. This offset ensured that the user-requested wavelength remained in the center of the ROI and in the center of the full x-axis of the emitted spectra graph [48].

The second adjustment was to command the PI-MAX to open multiple times during an acquisition before the spectrum was read out. By setting 20 gates/exposure, the PI-MAX

opened its gate 20 times, each corresponding to a trigger pulse from the delay generator to maintain time synchronicity, and the signal from each gate was combined onto the single outputted exposure. This method gave higher intensity counts and a lower SNR and allowed Ar I and Ar II peaks to be clearly seen, even at a 4-ns gate time.

Using these two software functionalities to boost intensities required verifying the assumption that the ICCD-spectrometer assembly was capturing the same time in the voltage pulse and same plasma with every gate. A series of tests at different operating conditions was conducted, and the NSP voltage waveform, PI-MAX gate monitoring signal, and photodiode signal were monitored by the oscilloscope. Figure 6.3 shows the results of an example test where 20 spectra, each with 20 gates/exposure were taken for a 16 kV, 4 kHz plasma at 1 Torr. While the oscilloscope was only fast enough to capture 34 of the 400 gates, Figure 6.3 indicates that the measured voltage pulse, plasma light emission as measured by the photodiode, and 4-ns gate window were all consistent and repeatable. Thus, it was reasonable to assume that the voltage waveform was identical from pulse to pulse and that the camera gated at the same time window for every pulse. It was also reasonable to assume that the plasma, as analyzed by total light emission intensity, was the same for every voltage pulse and spectral shot. Thus, the camera gated at approximately the same voltage pulse position for the 20 gates/exposure, and the voltage pulses and therefore the plasma were approximately identical through the duration of a test.

### 6.2.2 Test Matrix

Table 6.2 shows the full test matrix that was conducted to investigate the effects of the parameters listed in Section 6.1 on plasma properties. There were a total of 12 groups in the test matrix, and 3-5 files per group. The delay times for each operating condition were swept from the onset of a photodiode signal to  $\sim 20$  ns past the end of the voltage pulse unless otherwise noted. The delay time difference between two consecutive gates was 2 ns

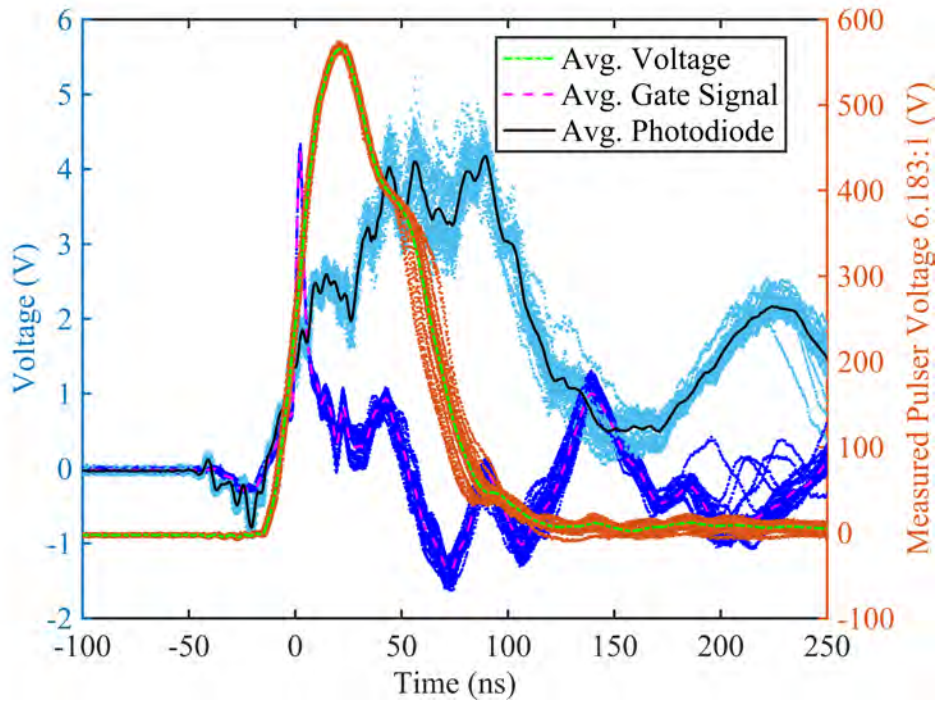


Figure 6.3: Measured voltage waveform, photodiode, and 4-ns camera gate monitoring signal over 34 gates with their respective averaged values.

for the first 80% of the sweep and 4 ns for the last 20%.

Table 6.2: Complete nanosecond-pulsed plasma test matrix.

	<b>Pressure</b> <b>Ar (Torr)</b>	<b>Discharge</b> <b>Voltage (kV)</b>	<b>Pulser Freq</b> <b>(kHz)</b>
<b>Frequency study at 1 Torr, 10 kV</b> (Group 1)	1.000	10	1
			0.5
			2
			4
			8
<b>Frequency study at 1 Torr, 8 kV</b> (Group 2)	1.000	8	1
			0.5
			2
			4
			8
<b>Frequency study at 1 Torr, 14 kV</b> (Group 3)	1.000	14	1
			0.5
			2
			4

*Continued on next page*

Table 6.2 – Continued from previous page

	<b>Pressure Ar (Torr)</b>	<b>Discharge Voltage (kV)</b>	<b>Pulser Freq (kHz)</b>
			8
<b>Discharge voltage study at 1 Torr, 1 kHz</b> (Group 4)	1.000	8	1
		12	
		16	
		20	
<b>Discharge voltage study at 1 Torr, 2 kHz</b> (Group 5)	1.000	8	2
		12	
		16	
		20	
<b>Discharge voltage study at 1 Torr, 4 kHz</b> (Group 6)	1.000	8	4
		12	
		16	
		20	
<b>Pressure study at 10 kV, 1 kHz</b> (Group 7)	1.000	10	1
	2.000		
	3.000		
<b>Pressure study at 10 kV, 4 kHz</b> (Group 8)	1.000	10	4
	2.000		
	3.000		
<b>Pressure study at 14 kV, 1 kHz</b> (Group 9)	1.000	14	1
	2.000		
	3.000		
<b>Pressure study at 14 kV, 4 kHz</b> (Group 10)	1.000	14	4
	2.000		
	3.000		
<b>Pressure study at 20 kV, 1 kHz</b> (Group 11)	1.000	20	1
	2.000		
	3.000		
<b>Pressure study at 20 kV, 4 kHz</b> (Group 12)	1.000	20	4
	2.000		
	3.000		

### 6.2.3 NSP Voltage Waveforms

Figure 6.4 shows sample waveforms from the six different discharge voltage conditions that were used for nanosecond pulsed plasma testing. Each set of discharge voltage waveform

Table 6.3: Voltage waveform properties for nanosecond pulsed plasma generation.

<b>Discharge Voltage (kV)</b>	<b>Measured Voltage (kV)</b>	<b>% Difference</b>	<b>Rise Time (ns)</b>	<b>Fall Time (ns)</b>
8	2.20	72.5%	27.6	306.0
10	2.73	72.7%	26.0	169.2
12	2.99	75.1%	24.8	98.8
14	3.31	76.4%	23.6	80.4
16	3.68	77%	22.8	43.2
20	4.37	78.1%	22.8	38.0

corresponded to 60-74 gates. While the rise time of all sets of voltage waveforms were consistent, the fall times were heavily dependent on the voltage. Lower voltages (8 kV and 10 kV) had longer fall times. The 14 kV condition seemed to be the bounding case. Table 6.3 lists the desired NSP voltage, actual outputted voltage, and rise and fall times of the voltage pulse, as defined traditionally as the interval between 10% and 90% of the peak amplitude [7].

The long RC time decay at lower voltages could be because the energy that was going into the plasma cell load first charged the capacitance of the load and then drained away through the NSP’s internal resistors after the pulse. At higher voltages, the energy went directly into the plasma or was high enough that it caused a breakdown in the capacitance of the load. This could explain why the 14 kV condition seemed to generate the most “unstable” and flickering plasma. This discharge voltage was just high enough that the plasma cell capacitance was beginning to break down, but it was not yet consistent, so some voltage pulses were charging and discharging the plasma cell capacitance while others were going directly into the plasma. Note that increasing the discharge voltage brought fall times closer to the rise times, potentially because that capacitive discharge did not occur.

As discussed in Section 3.3.2.1, the voltage seen by the plasma cell load was not the same as what was requested from the NSP because of the short 20-ns pulse width and the resistive plasma cell load. However, there seemed to be a proportional difference in

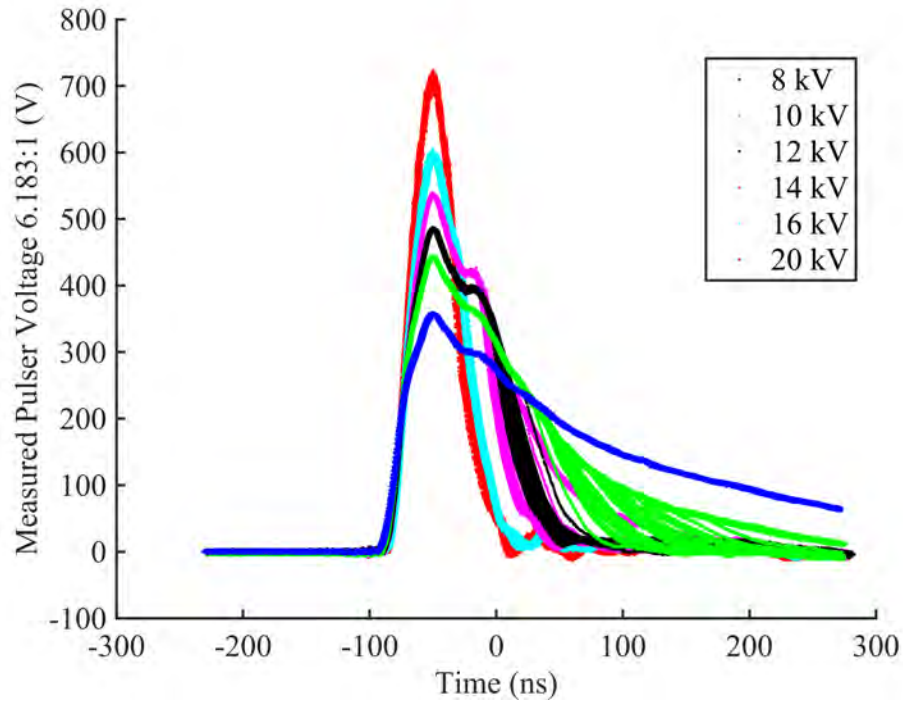


Figure 6.4: Comparison of low-voltage and high-voltage pulses on the NSP.

desired output to measured voltage, so meaningful trends could still be observed. Similarly, although the voltage pulse was set to 20 ns, the NSP only reached steady state for 5-8 ns, which was enough time for 1-2 emission spectra to be captured. While not ideal, the changes in plasma behavior, the ionization and quench times, and the effectiveness of using a given plasma for a VLF plasma antenna could still be established with these voltage pulses.

### 6.3 OES Analysis Overview

The Ar I and Ar II lines that were selected for line ratio calculations of the nanosecond-pulsed plasma are listed respectively in Table 6.4 and Table 6.5. The transitions for each wavelength are given as reference from [38] and are written as electron configuration, term, and angular momentum J. Those lines were limited by the PI-MAX usable wavelength range as well as the need to select lines that were at least 2 nm away from other peaks to minimize any peak matching errors. The PI-MAX gain was dropped at pressures greater

than 1-Torr argon to prevent oversaturation of the emission intensity. The peak finding procedure for the nanosecond pulsed plasma was similar to the one described in Section 5.1.1.1 and is further described in Appendix C.

Table 6.4: Selected argon neutral spectral lines for line ratio calculations of nanosecond pulsed plasma.

Ar I Air Wavelength (nm)	Relative Intensity	Transition [38]
696.5431	10000	$4p^2[1/2]1 \rightarrow 4s^2[3/2]2$
706.7218	10000	$4p^2[3/2]2 \rightarrow 4s^2[3/2]2$
727.2936	2000	$4p^2[1/2]1 \rightarrow 4s^2[3/2]1$
738.3980	10000	$4p^2[3/2]2 \rightarrow 4s^2[3/2]1$
750.3869	20000	$4p^2[1/2]0 \rightarrow 4s^2[1/2]1$

Table 6.5: Selected argon ion +1 emission spectral lines for line ratio calculations of nanosecond pulsed plasma.

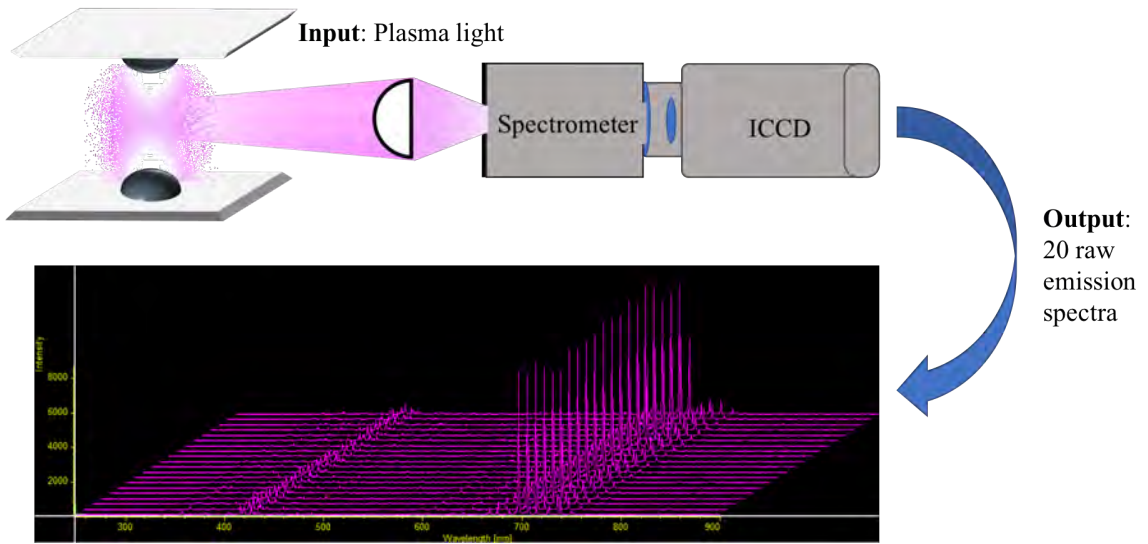
Ar II Air Wavelength (nm)	Relative Intensity	Transition [38]
404.2893	288	$4p^2D\ 3/2 \rightarrow 4s^2D\ 3/2$
407.2004	708	$4p^2D\ 5/2 \rightarrow 4s^2D\ 5/2$
413.1723	891	$4p^2P\ 1/2 \rightarrow 4s^2D\ 3/2$
427.7528	1995	$4p^2P\ 3/2 \rightarrow 4s^4P\ 3/2$
434.8064	1995	$4p^4D\ 7/2 \rightarrow 4s^4P\ 5/2$
440.0986	8710	$4p^4P\ 5/2 \rightarrow 3d^4D\ 7/2$
442.6001	1514	$4p^4D\ 5/2 \rightarrow 4s^4P\ 3/2$
454.5052	1738	$4p^2P\ 3/2 \rightarrow 4s^2P\ 3/2$
460.9567	2291	$4p^2F\ 7/2 \rightarrow 4s^2D\ 5/2$
465.7901	1445	$4p^2P\ 1/2 \rightarrow 4s^2P\ 3/2$
472.6868	23442	$4p^2D\ 3/2 \rightarrow 4s^2P\ 3/2$
476.4864	2344	$4p^2P\ 3/2 \rightarrow 4s^2P\ 1/2$
480.6020	1820	$4p^4P\ 5/2 \rightarrow 4s^4P\ 5/2$
487.9863	2239	$4p^2D\ 5/2 \rightarrow 4s^2P\ 3/2$
501.7163	7413	$4p^2F\ 5/2 \rightarrow 3d^2D\ 3/2$

Three PrismSPECT simulations were run, one at each test pressure of 1-Torr, 2-Torr, and 3-Torr argon. While each pressure simulation had a different electron temperature

range, they all ran with an electron temperature resolution of 0.005 eV.

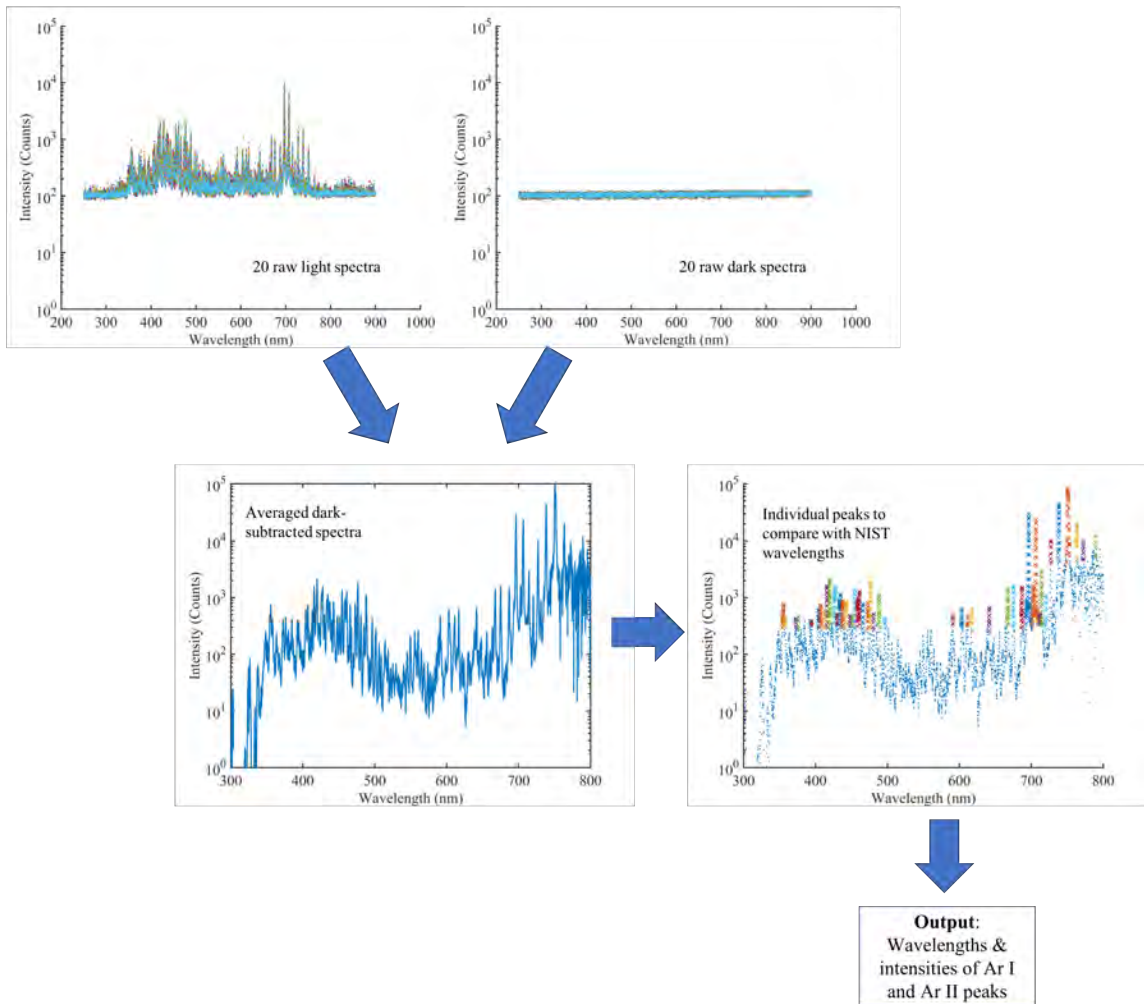
### 6.3.1 Process Diagram

Figure 6.5 illustrates the main data collection, data processing, and line ratio analysis steps that were used to obtain the final, time-resolved  $T_e$  and  $n_e$  measurements without discussing the details of each step.

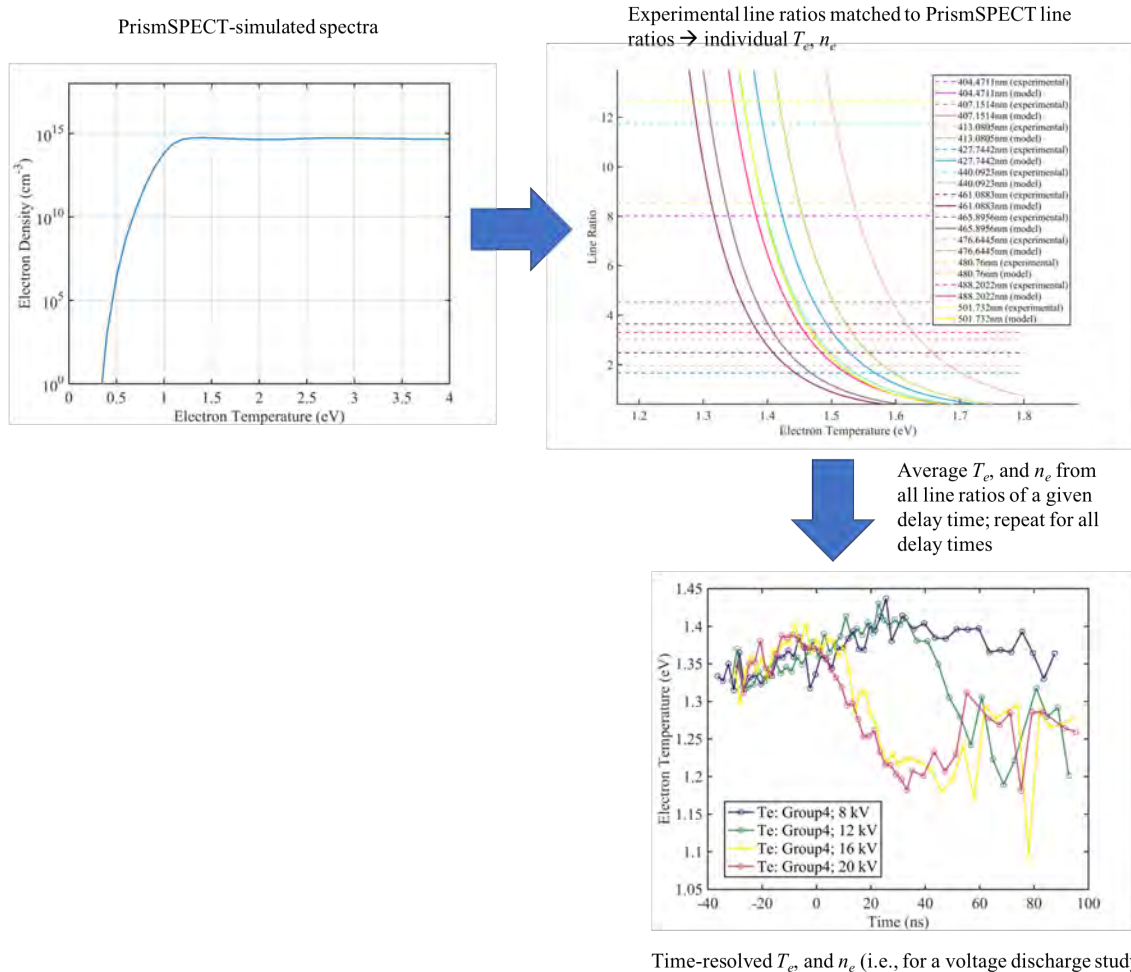


(a) Data acquisition of plasma light emissions for raw spectral data.

For a given time delay:



(b) Data processing of raw spectral data at each delay time for wavelengths and intensities at selected Ar I and Ar II spectral peaks (Tables 6.4 and 6.5).



(c) Comparing experimental line ratios to PrismSPECT-simulated line ratios to obtain time-resolved  $T_e$  and  $n_e$ .

Figure 6.5: Diagram of full process, from data collection to time-resolved  $T_e$  and  $n_e$  measurements.

## 6.4 Results

Images of the plasma at various discharge voltages, pulse frequencies, and pressures are shown in Figures 6.6-6.8. These pictures were all taken with a Nikon D90 at  $f/18$  aperture and  $1/30$  shutter speed. The biggest visual differences were that as discharge voltage and pulse frequency were increased, the plasma got visibly brighter, and the volume of plasma increased. This trend is also demonstrated by the maximum intensities in the emission

spectra shown in Figure 6.9. As expected, increasing discharge voltage increased light emissions because a greater population of neutrals could be excited or ionized. Similarly, increasing frequency effectively increased the duty cycle of the NSP, so in a given amount of time, there were more opportunities for the argon neutrals in the plasma cell to be excited and ionized.

Another big visible difference in plasma was that as pressure increased, the plasma became more focused (less volumetric and more like an arc discharge) between the two electrodes (shown in Figure 6.8). At 1-Torr argon, the plasma looked like a glow discharge primarily around the positive (bottom) electrode. At 2 Torr, the plasma started to bridge the gap to the negative electrode in a funnel shape. By 3 Torr, the plasma had formed a narrow and focused beam across the two electrodes. The wavelengths of the emission spectra corresponding to excited argon neutrals had a large boost in intensity as pressure increased due to the increased number of atoms available for excitation and ionization.

#### 6.4.1 Line Ratio Comparison

At each gated time delay, the wavelengths in Table 6.4 and 6.5 were used for line ratio calculations. Each Ar II wavelength that had a peak in that given emission spectrum was compared to each Ar I line. Each experimentally-determined  $T_e$  and  $n_e$  from the line ratios were averaged to calculate a representative  $T_e$  and  $n_e$  for a time delay at a plasma operating condition. Those averaged  $T_e$  and  $n_e$  values were compared to line ratios from PrismSPECT to create time-resolved graphs.

Figure 6.10 shows an example intensity line ratio (many ion lines to a single neutral line) plotted against the PrismSPECT simulation for a plasma at 16 kV, 1 Torr, 4 kHz at the time delay that corresponded to the maximum voltage pulse. The results indicated  $T_e = 1.46 \text{ eV} \pm 0.047 \text{ eV}$  and  $n_e = 5.43 \times 10^{14} \text{ cm}^{-3} \pm 1.00 \times 10^{13} \text{ cm}^{-3}$ . After taking into account all of the Ar I line ratios, this specific gate time had an average  $T_e = 1.45 \text{ eV} \pm 0.046 \text{ eV}$  and an average  $n_e = 5.43 \times 10^{14} \text{ cm}^{-3} \pm 8.00 \times 10^{12} \text{ cm}^{-3}$ . This low variation

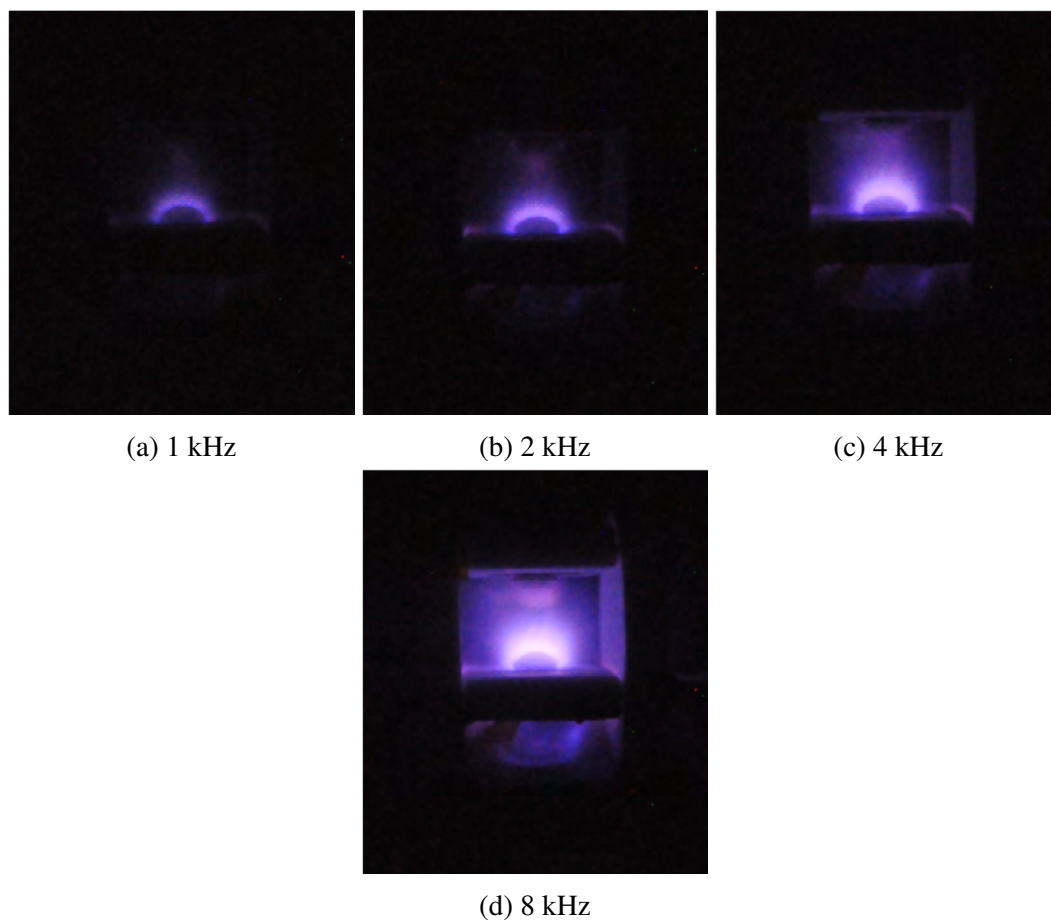


Figure 6.6: Pictures of nanosecond-pulsed plasma at different pulse frequencies, 10 kV, and 1 Torr.

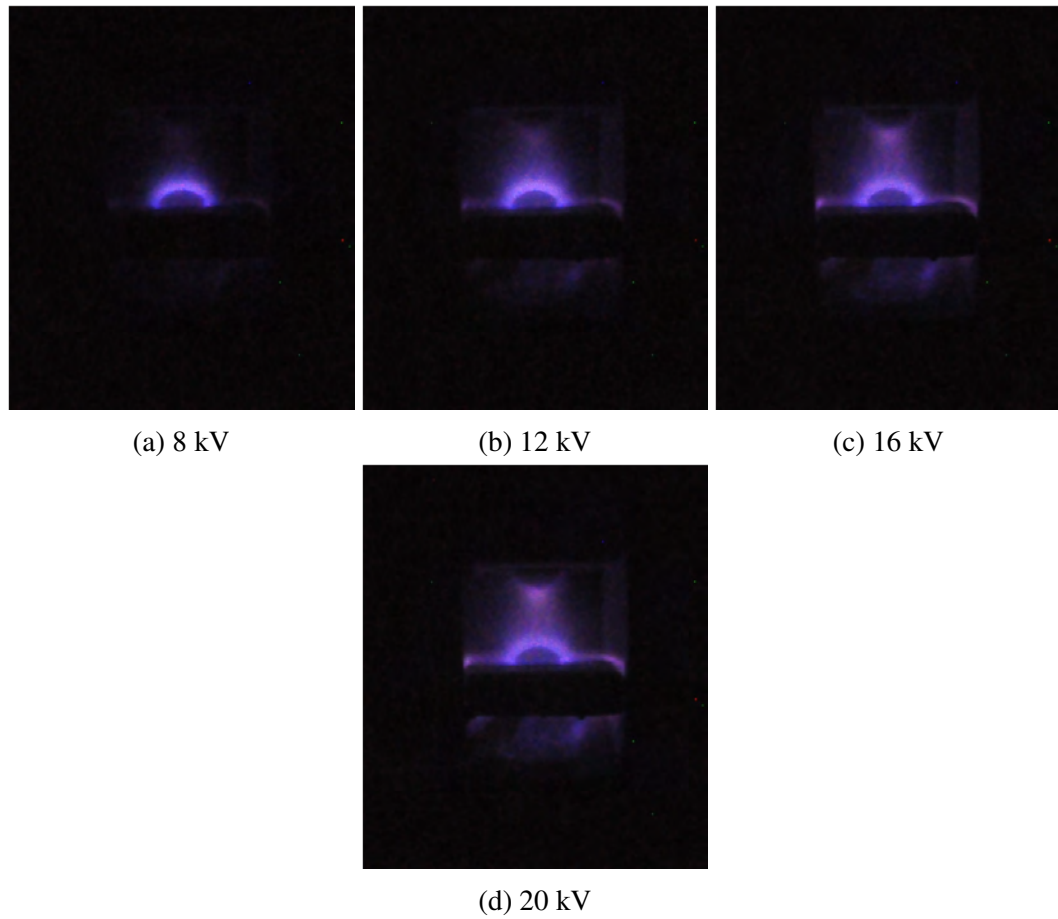


Figure 6.7: Pictures of nanosecond-pulsed plasma at different discharge voltages, 2 kHz, and 1 Torr.

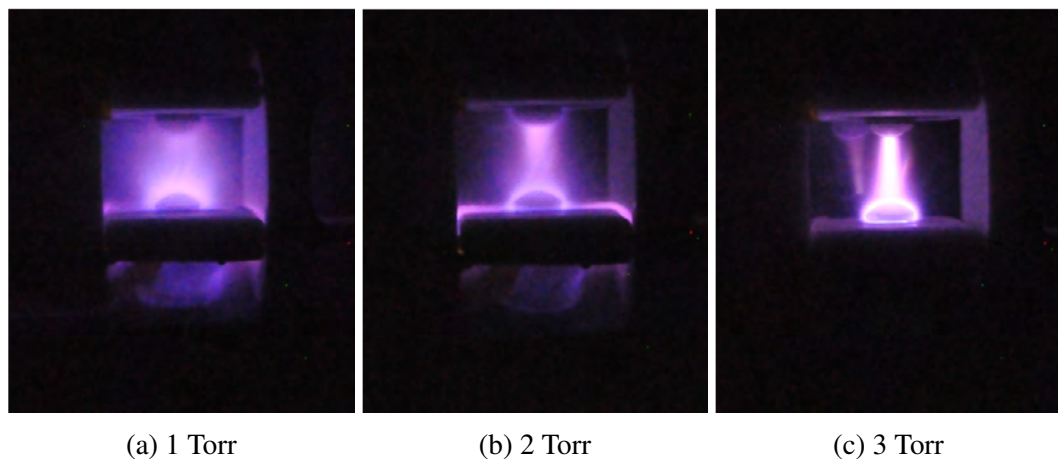
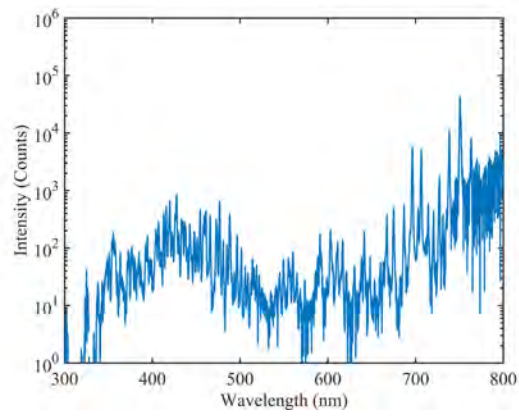
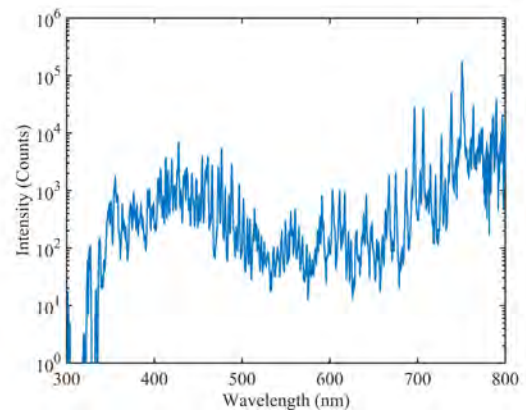


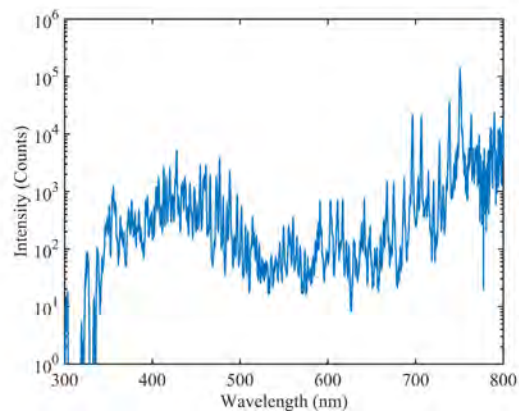
Figure 6.8: Pictures of nanosecond-pulsed plasma at different pressure conditions, 20 kV, and 4 kHz.



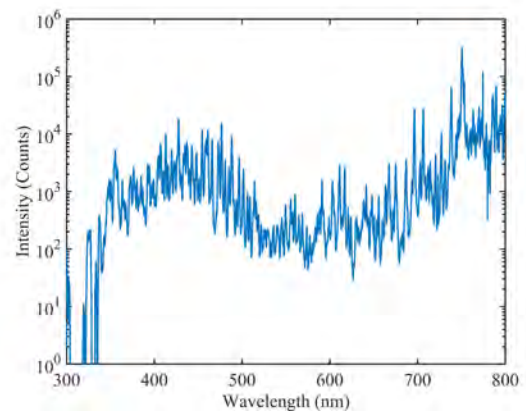
(a) 1 Torr, 8 kV, 1 kHz.



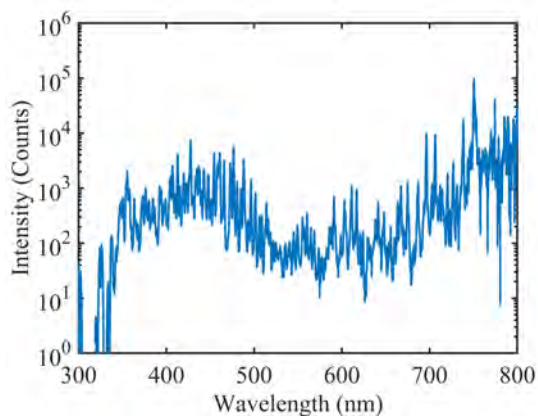
(b) 1 Torr, 20 kV, 1 kHz.



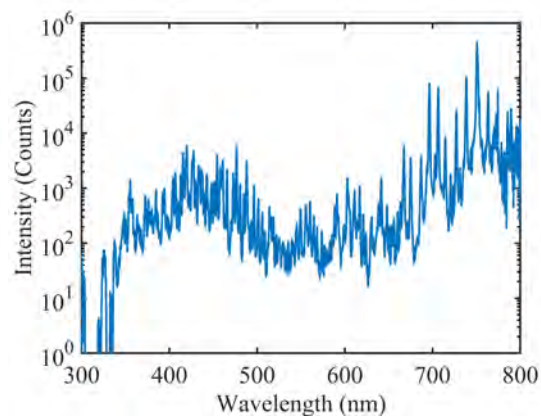
(c) 1 Torr, 16 kV, 1 kHz.



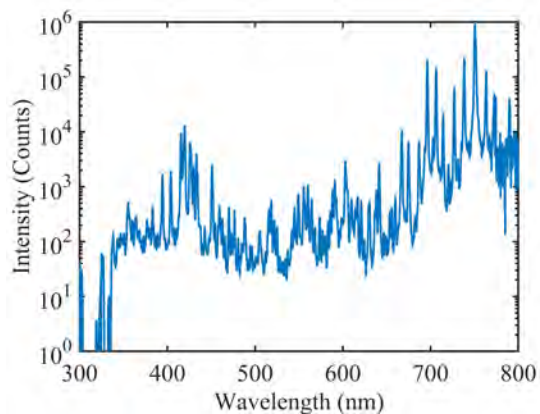
(d) 1 Torr, 16 kV, 4 kHz.



(e) 1 Torr, 10 kV, 4 kHz.



(f) 2 Torr, 10 kV, 4 kHz.



(g) 3 Torr, 10 kV, 4 kHz.

Figure 6.9: Emission spectra of nanosecond pulsed plasma at different operating conditions. Note the trend of increased intensities as discharge voltage and pulse frequency were increased. All spectra shown were taken at the gate time corresponding to maximum voltage pulse.

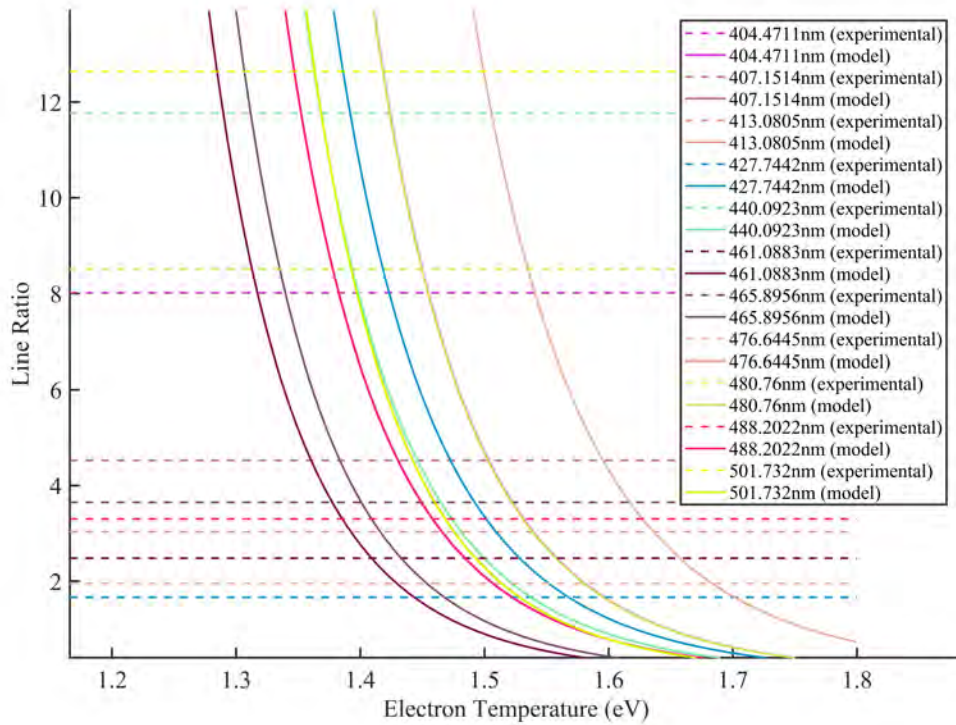


Figure 6.10: Example line ratio comparison (ratios of Ar I 696.53 nm to Ar II lines) of plasma at 16 kV, 1 Torr, 4 kHz at maximum voltage pulse.

in electron temperature and density demonstrated the good consistency between all the different chosen wavelengths. Further discussion about the uncertainty in this analysis is presented in Section 6.5.5.

The range of electron temperatures (1-2 eV) and densities ( $10^{14} - 10^{15} \text{ cm}^{-3}$ ) from all line ratio calculations of plasmas at different operating conditions corresponded well to experimentally-determined and modeled values of similar plasmas in literature [10, 44, 56, 58].

## 6.5 Time-Resolved Nanosecond Pulsed Plasma

Figures 6.11-6.22 show the time-resolved electron temperature, electron density, and plasma frequency of the nanosecond pulsed plasmas generated with operating conditions seen in Table 6.2. From the test matrix, the 1 kHz test in the 1 Torr, 10 kV frequency study

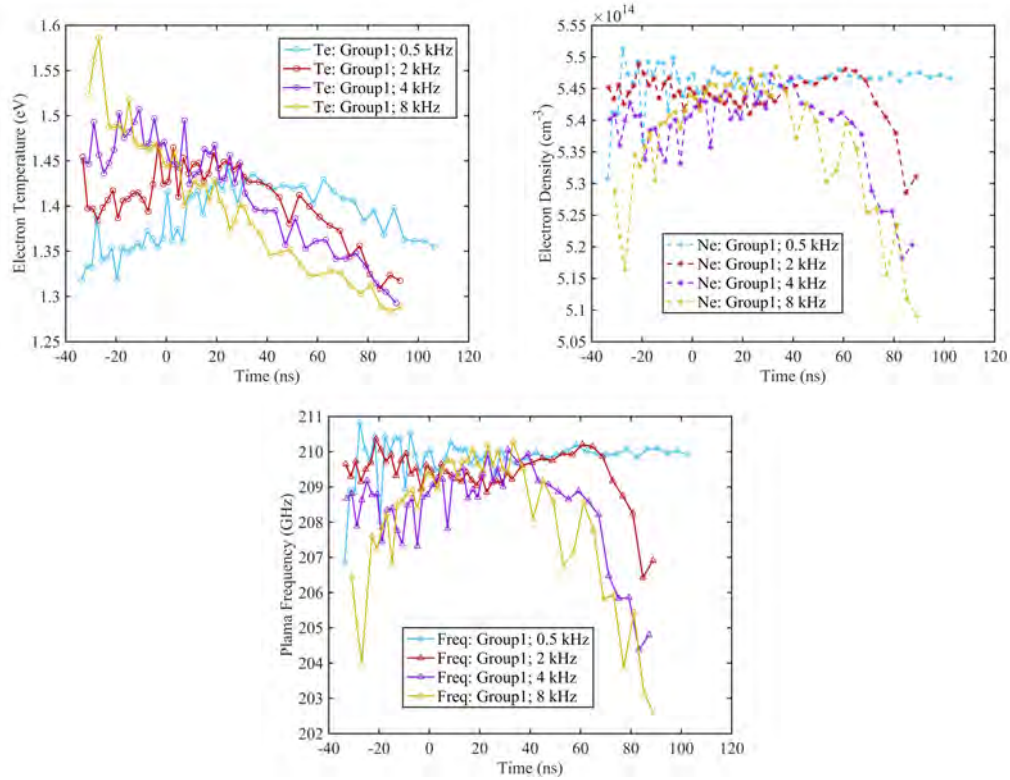


Figure 6.11: Time-resolved results of pulse frequency study at 1 Torr, 10 kV.

was not included in the time-resolved plots as the spectrometer reset its calibrations halfway through the test sequence, and this was not discovered until after the entirety of testing for this test condition had been completed. The 4 kHz and 8 kHz tests in the 1 Torr, 14 kV frequency study were not included as the plasma at those conditions was too unstable to obtain useful light emission spectra. For all the plots, the x-axis spans from 5% of the maximum voltage pulse on the rising edge to 15% of the maximum photodiode signal on the falling edge or to the last test taken. Time = 0 is defined as the time of the maximum voltage pulse.

### 6.5.1 Effects on Electron Temperature

As pulse frequency increased, the maximum  $T_e$  value was larger, and the time of that maximum  $T_e$  shifted leftwards in time (i.e.,  $T_e$  rose and decayed faster in time). For example, in Figure 6.11, the 500-Hz case took almost 40 ns past the peak voltage pulse to

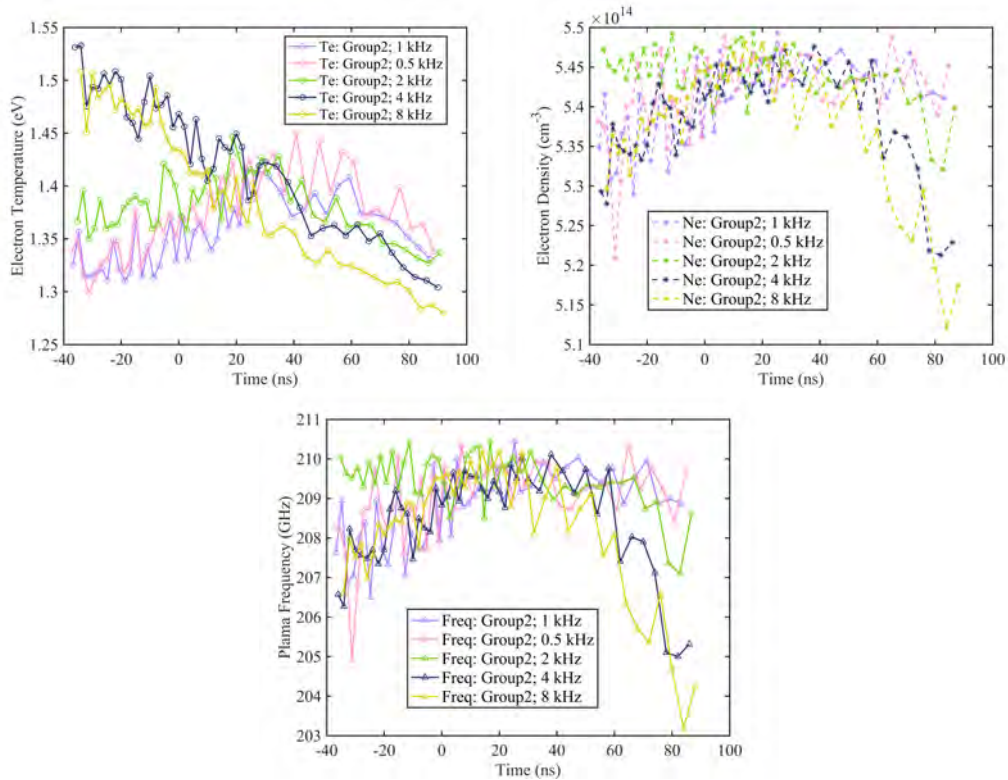


Figure 6.12: Time-resolved results of pulse frequency study at 1 Torr, 8 kV.

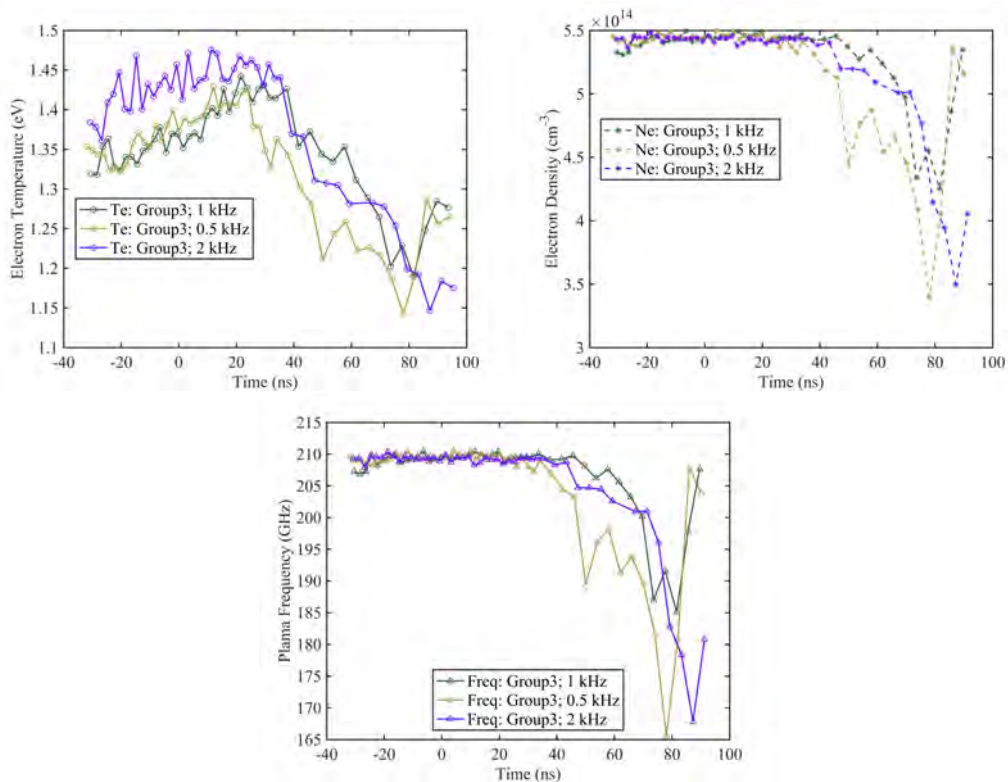


Figure 6.13: Time-resolved results of pulse frequency study at 1 Torr, 14 kV.

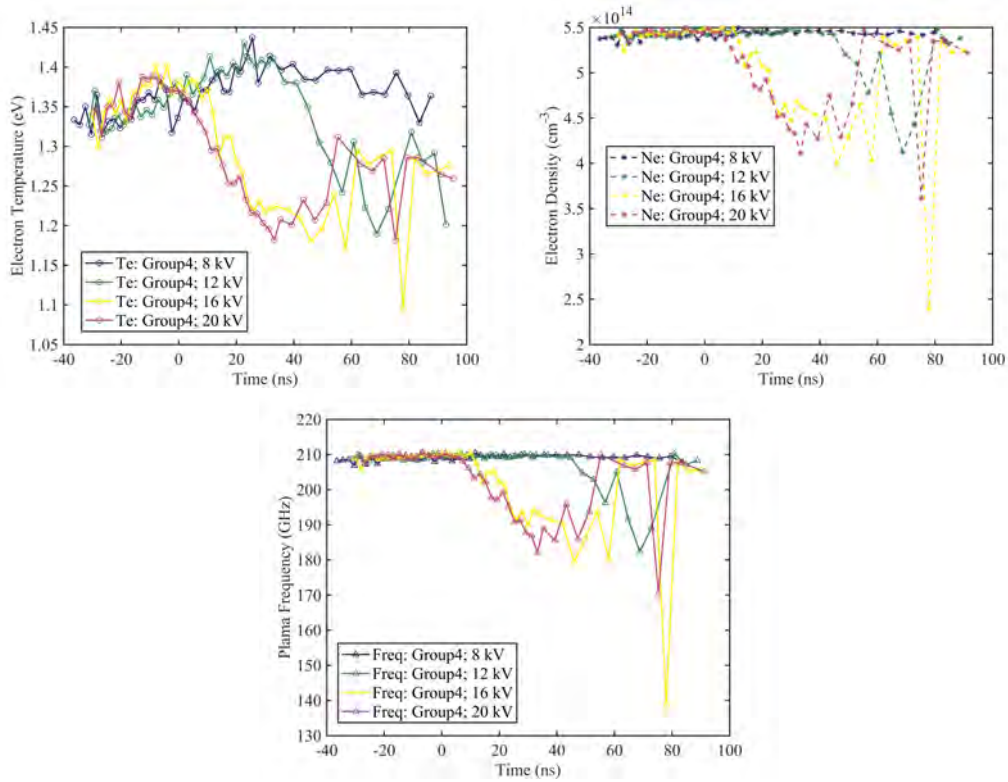


Figure 6.14: Time-resolved results of voltage study at 1 Torr, 1 kHz.

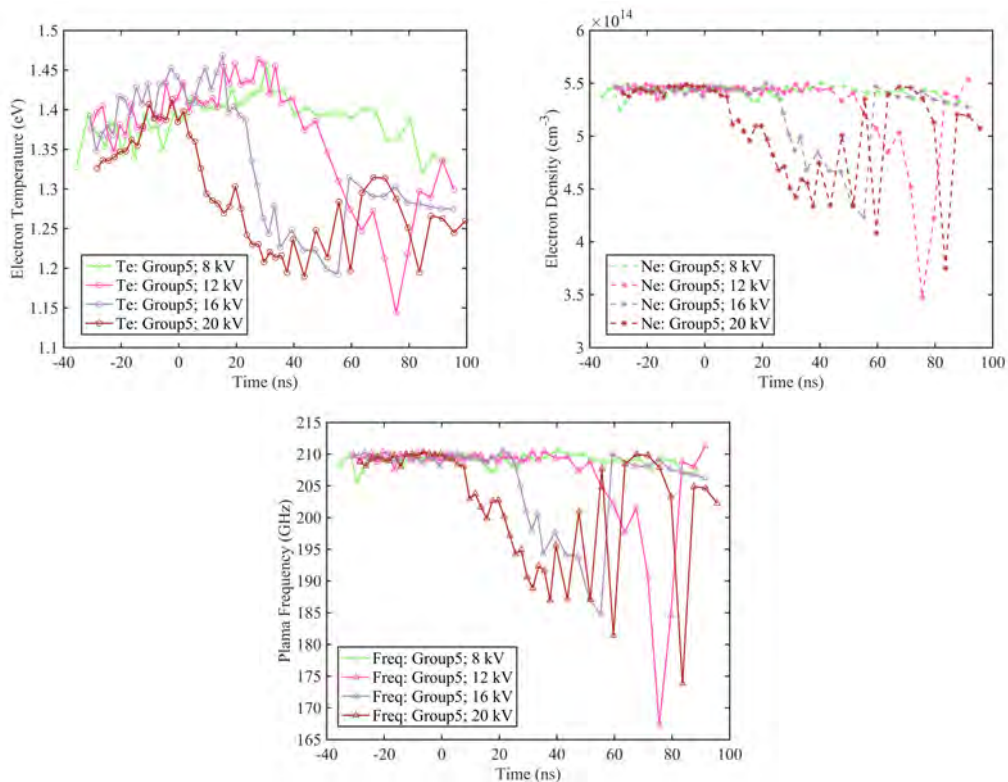


Figure 6.15: Time-resolved results of voltage study at 1 Torr, 2 kHz.

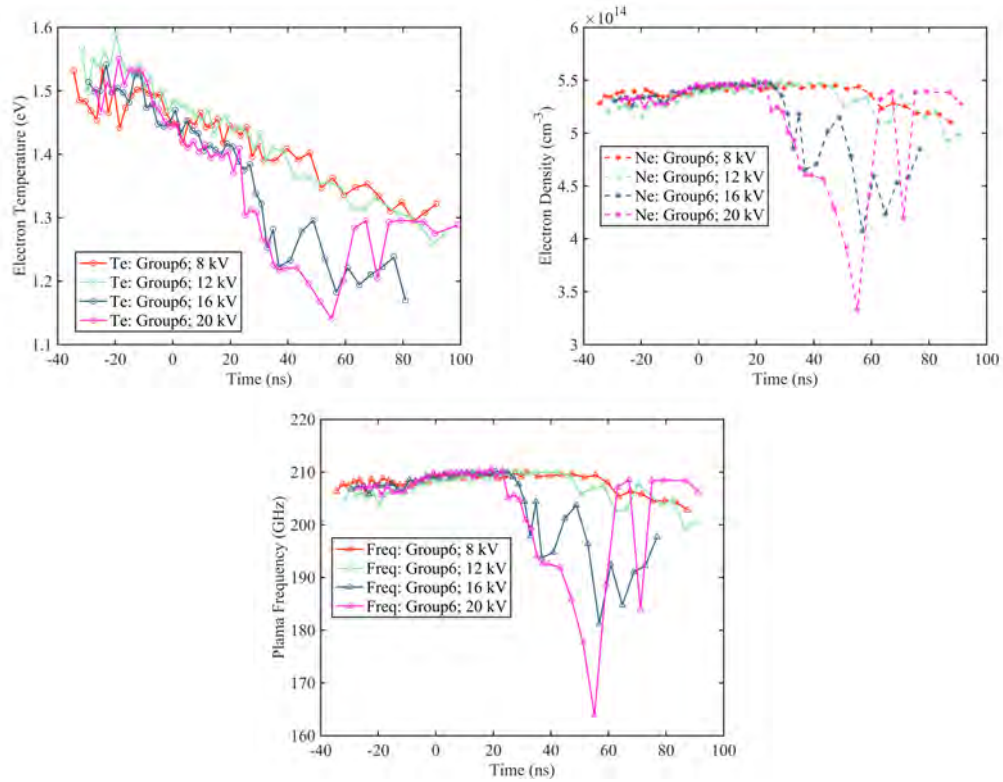


Figure 6.16: Time-resolved results of voltage study at 1 Torr, 4 kHz.

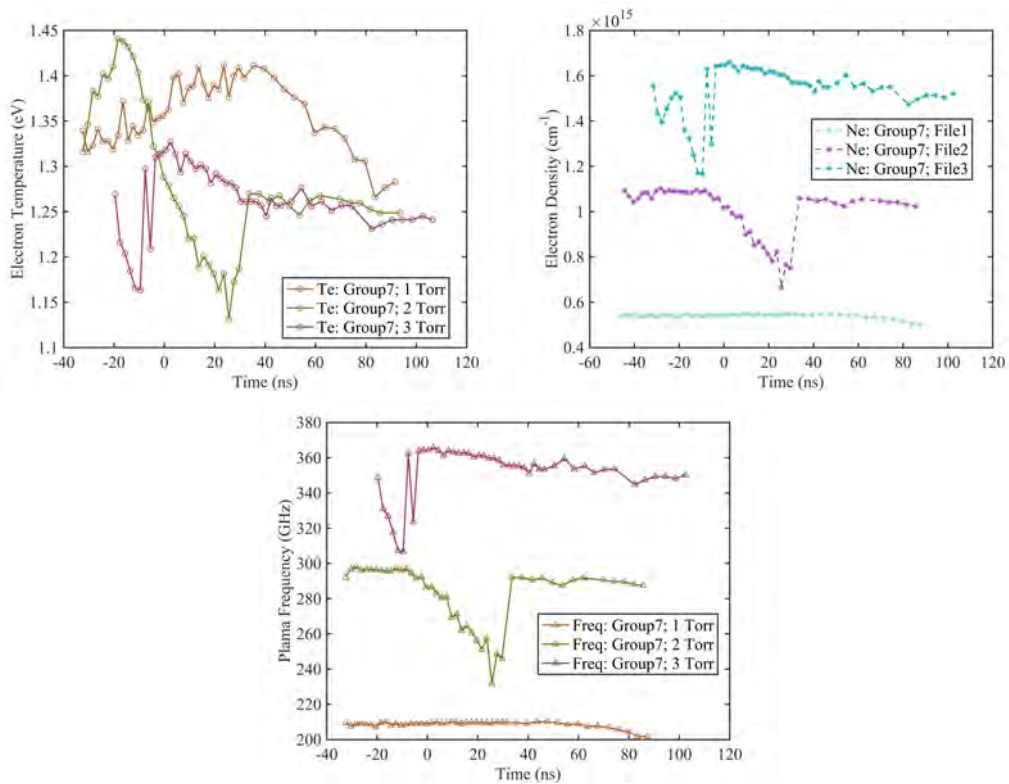


Figure 6.17: Time-resolved results of pressure study at 10 kV, 1 kHz

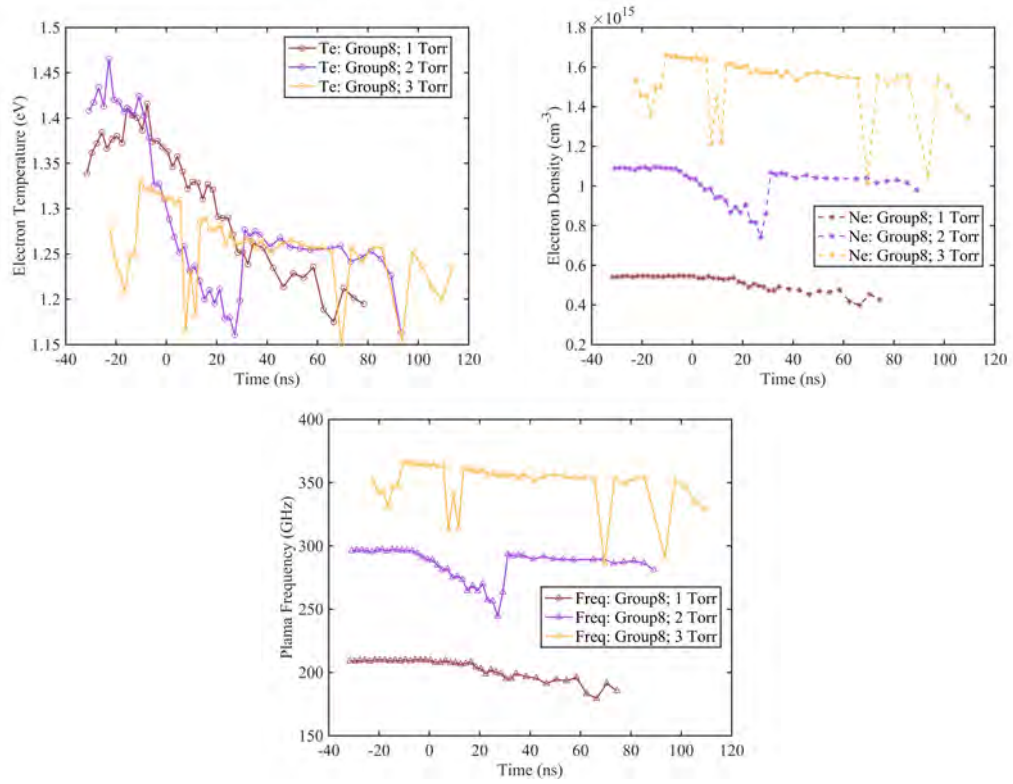


Figure 6.18: Time-resolved results of pressure study at 10 kV, 4 kHz

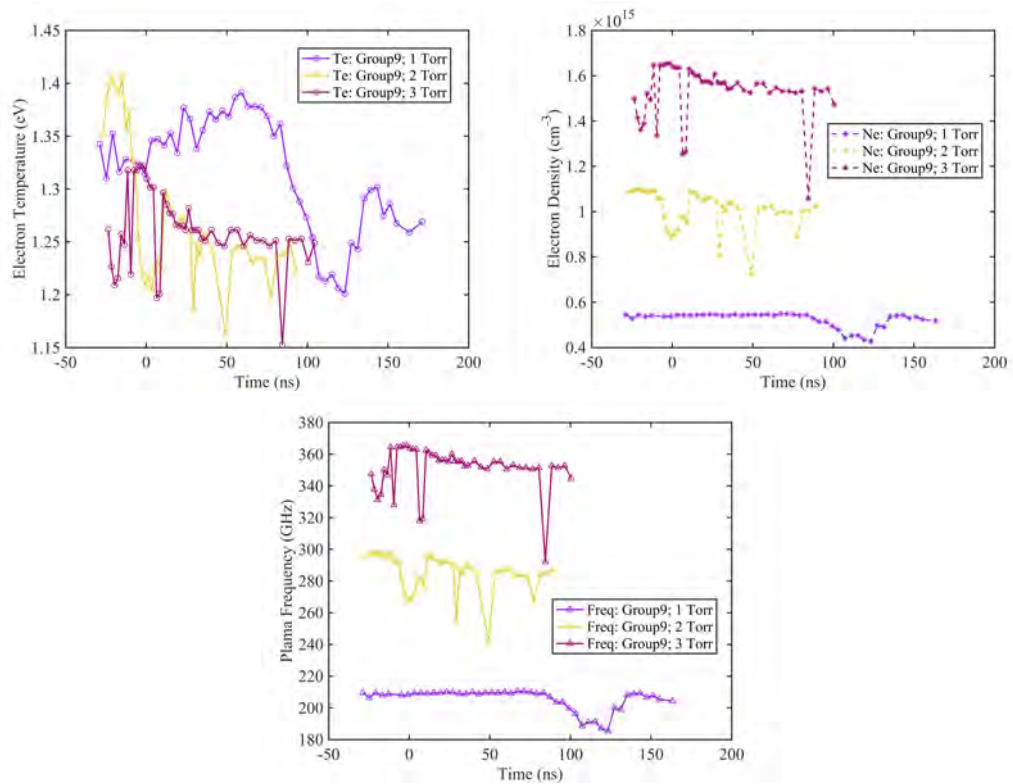


Figure 6.19: Time-resolved results of pressure study at 14 kV, 1 kHz

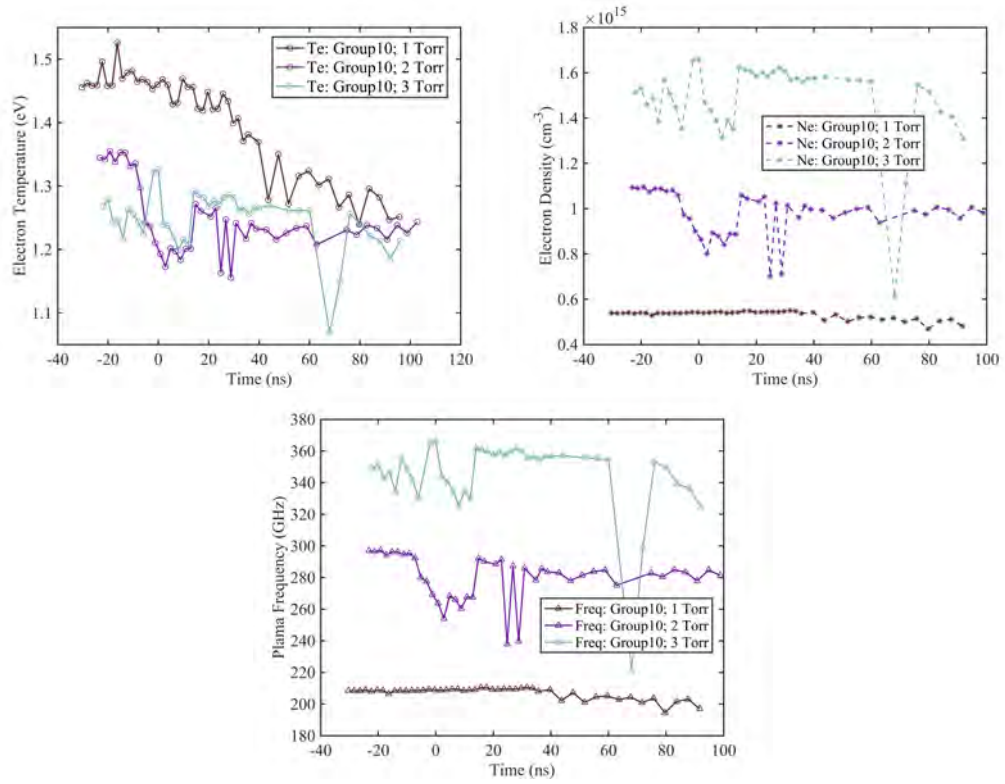


Figure 6.20: Time-resolved results of pressure study at 14 kV, 4 kHz

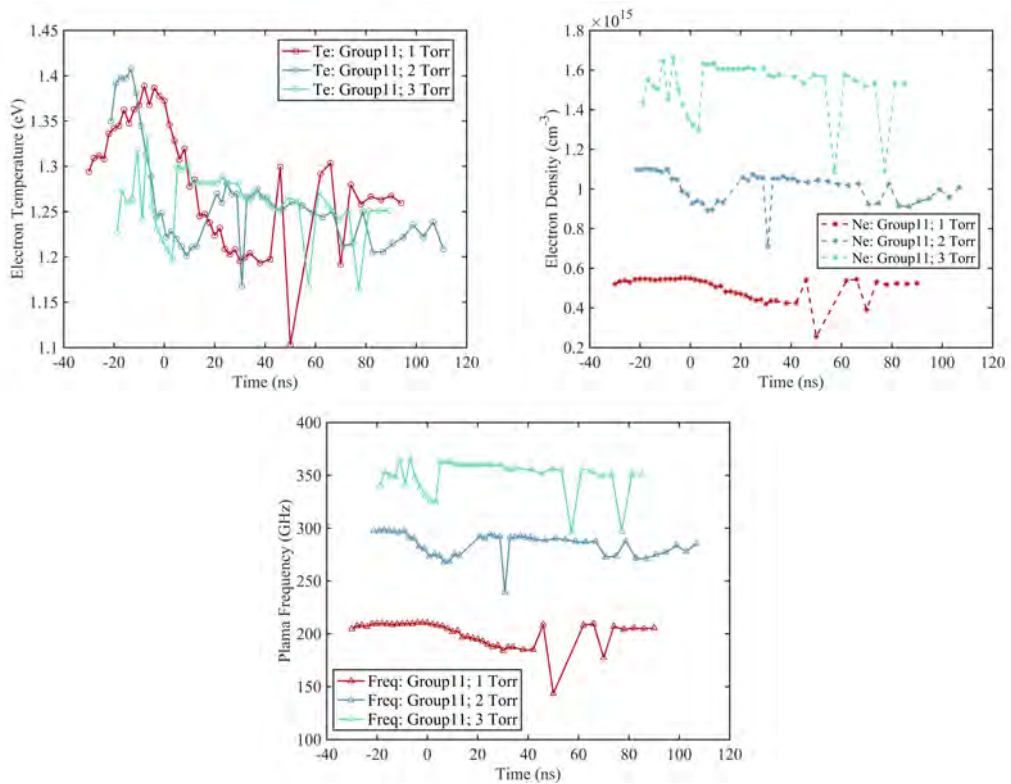


Figure 6.21: Time-resolved results of pressure study at 20 kV, 1 kHz

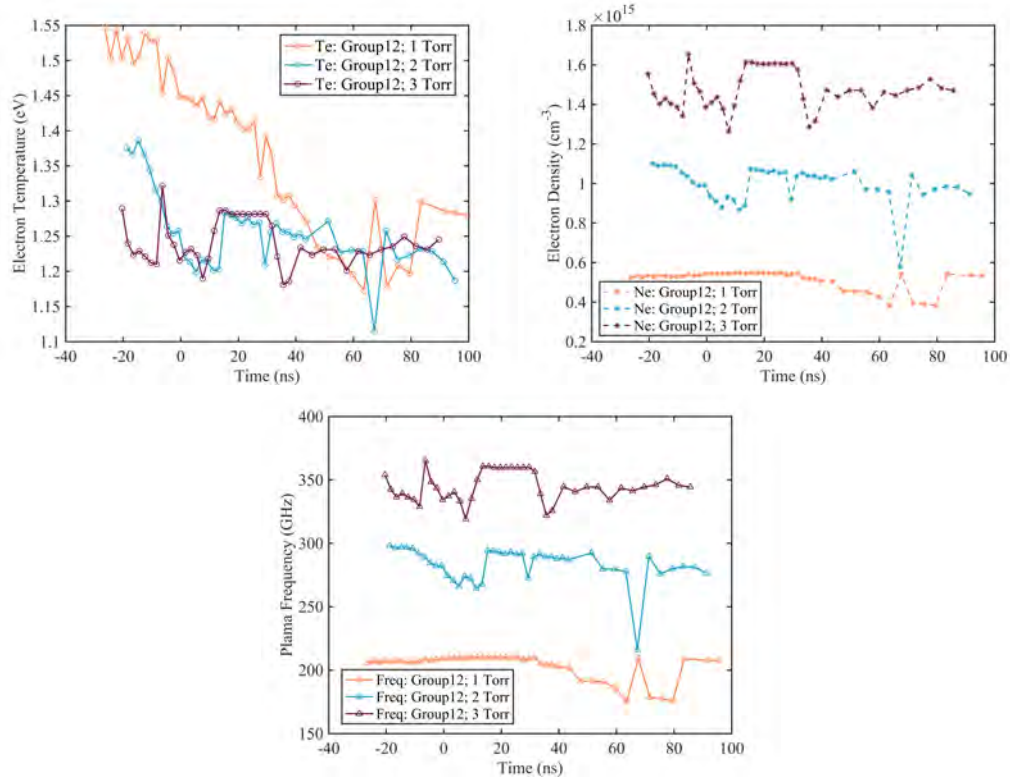


Figure 6.22: Time-resolved results of pressure study at 20 kV, 4 kHz

reach max  $T_e$  while the 8-kHz case reached maximum  $T_e$  about 35 ns before the peak voltage (at  $\sim 5\%$  peak voltage). This indicates that a large difference in the plasma dynamics of higher and lower frequency pulsed plasmas is how the intensities of argon neutrals and ions rise and fall. The line ratio was defined as the neutral intensity to ion intensity, so higher ion counts with a similar neutral count gave a lower line ratio and thus a higher  $T_e$  (as seen in Figure 6.10). At lower frequency plasmas, Ar I dominated the emission spectra. Both Ar I and Ar II initially increased as delay time was increased and the plasma emission captured was at a higher voltage pulse. However, Ar I counts were initially 2-3 times larger than Ar II counts, so as more argon neutrals were ionized and the Ar II counts increased, the line ratio dropped, and  $T_e$  thus increased with time. Eventually, Ar II counts began to decrease while Ar I counts increased, and  $T_e$  dropped.

For high frequency (i.e., 4 kHz and 8 kHz) plasmas,  $T_e$  started at a maximum value because the ion emission was immediately stronger than the neutral emission at that low

voltage. With time, more neutrals were excited, thus continuously increasing the intensity of Ar I and decreasing  $T_e$ . No rise was seen in these high frequency plasmas, potentially because the ICCD/spectrometer was not sensitive enough. A low  $T_e$  ( $< 1$  eV) required Ar II counts 100s–1000s times smaller than Ar I counts, and these extremely low intensities occurred before 5% maximum voltage pulse. The SNR below 5% voltage maximum was too low to calculate an accurate line ratio.

For the voltage studies, it was interesting to note that while electron temperature varied temporally in a similar manner as the pulse frequency studies, the maximum  $T_e$  was only weakly dependent, if not independent, of the applied voltage. Electron temperature decayed faster with increasing discharge voltage, similar to simulation results observed by Liu et al [10]. Lower voltages, such as the 8-kV case in Figure 6.14, gave a more steady  $T_e$  output for longer, which was directly correlated to the longer voltage pulse fall times of lower voltages shown in Table 6.3. However, conducting the voltage study at a high pulse frequency like 4 kHz in Figure 6.16 demonstrated that all voltages, even lower discharge voltages, reached their maximum  $T_e$  before maximum voltage. This was additional data that increasing pulse frequency shifted maximum electron temperature leftwards in time.

The pressure effect on electron temperature was the least obvious. All plasmas in the pressure study groups had a rise and slow decay in electron temperature. The different pressures seemed to time shift these events such that higher pressure plasmas increased and decreased the soonest in time. There was also a trend of electron temperature being inversely proportional to pressure, which correlated with results from literature [70]. There was a shorter mean free path at increased pressure conditions, so greater thermal energy was lost to the more frequent collisions, resulting in a lower  $T_e$ . The rise and decay rates of  $T_e$  also increased with increasing pressure as increased collisions led to increased energy transfer.

Note that the maximum  $T_e$  and  $n_e$  of the 3 Torr test condition are not seen in any of the results figures as those maximums occurred before 5% maximum voltage. With a high

starting density of argon neutrals, not much discharge voltage was needed to reach a high argon ion density and intensity. As time increased (i.e., further into the plasma lifetime), neutral excitation processes dominated. Similarly, few maximums in the 4 kHz test conditions (Groups 8, 10, and 12), even for the 1-Torr plasmas, were seen.

### 6.5.2 Effects on Electron Density

While the maximum electron density of a plasma was relatively independent of pulse frequency, higher frequencies started at a lower  $n_e$  at a given time and had a faster decay rate. The visual results in Figure 6.6 show that a significantly brighter plasma was generated as pulser frequency was increased, but an independence in  $n_e$  from the time-resolved results indicated that while higher pulser frequencies introduced more electrons to the plasma system, more argon neutrals were not ionized. Instead, the dominant process and the cause of the increased visual intensity in the plasma was a large increase in excited argon neutral population. The faster  $n_e$  decay rate at higher pulse frequencies could be a result of more three-body recombination processes occurring (described in Section 4.1) as more electrons were pushed through the plasma more often.

The electron density profile was also relatively invariant with respect to voltage, but higher discharge voltage conditions led to  $n_e$  decaying sooner after maximum voltage pulse, similar to the  $T_e$  response. Therefore, changing discharge voltage changed how soon recombination processes occurred in the plasma, with higher voltage plasmas recombining sooner. The  $n_e$  decay rates were approximately constant across the voltage cases.

In general for the 1-Torr case, maximum  $n_e$  was temporally later than maximum voltage pulse. This time delay could be attributed to the dependence of ionization rate to electron temperature. The argon neutral and ion population fraction at a given pressure from PrismSPECT was used as a good indicator of ionization rate (i.e., higher populations of a given ion imply higher ionization rate for that ion). The cross-over between argon

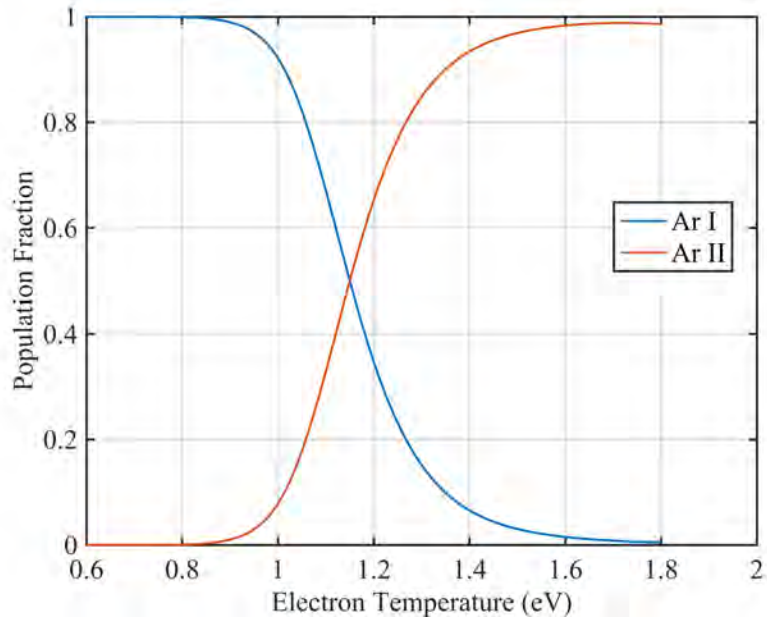


Figure 6.23: PrismSPECT-simulated population fraction of argon neutrals (Ar I) and ions (Ar II) as a function of electron temperature for a 1-Torr plasma.

neutral and +1 ions at 1 Torr is 1.15 eV (shown in Figure 6.23), and  $n_e$  began to decay when  $T_e \approx 1.2 - 1.3$  eV.

The effect of pressure on electron density was approximately linear, as clearly seen in Figures 6.17-6.22.  $n_e$  for all three pressures followed similar temporal profiles – after remaining approximately constant,  $n_e$  drops, rises to almost the same value, and slowly decays again. These events were time-shifted for the different pressures. In Figure 6.19, where additional tests were taken for the 1 Torr case past the voltage pulse,  $n_e$  displayed the same behavior as the 2 Torr and 3 Torr cases. The time scales for the constant, drop, rise, and slow decay of  $n_e$  were significantly longer. This faster temporal response at higher pressures could be attributed to greater recombination at higher pressures.

### 6.5.3 Effects on Plasma Frequency

Clearly indicated in Equation 1.5, plasma frequency followed the electron density trends. All tested plasmas had a plasma frequency above the minimum 10 GHz needed for a VLF plasma antenna, so an even faster pulse modulation scheme could be used to break up the

incoming signals, or the requirements for discharge voltage and pulse frequency could be relaxed.

Neither pulse frequency nor discharge voltage affected the maximum plasma frequency of  $\sim 210$  GHz, but plasma frequency dropped to a lower value faster at high voltages. This indicated that plasma antennas desiring a faster shut off time would want higher discharge voltages. Plasma antennas with too low of a plasma frequency and were limited in pulse frequency and discharge voltage could still reach  $> 10$  GHz by increasing the argon pressure.

#### 6.5.4 Ionization & Recombination Times

From the data provided and with reference to PrismSPECT simulations of argon neutral and ion populations, plasmas in all operating conditions had ionization times in the tens of nanoseconds based on the difference in time between the crossover point of Ar I and Ar II populations and the initiation of the voltage pulse. The plasmas also had recombination times in the tens of nanoseconds (10-100 ns), although recombination times were longer than ionization times. Higher discharge voltages and higher frequencies led to faster electron density decay, which suggested faster recombination times. These results indicated that the ionization and recombination times were sufficiently fast for the VLF plasma antenna to be feasible using any of the operating conditions listed in Table 6.2.

#### 6.5.5 Uncertainty Analysis

As illustrated in Figure 6.5, the time-resolved electron temperature, electron density, and plasma frequency values were obtained from several averaging steps. This subsection breaks down the uncertainties involved in the data collection and analysis.

The camera/spectrometer setup necessitated the collection of emitted light from a spherical volume of the nanosecond-pulsed, argon plasma discharge. This light was collectively passed into the spectrometer slit as a spatial average. Therefore, the resulting

emission spectra contained no information about a specific, spatial location in the plasma but rather of the spatially-averaged, volumetric plasma discharge.

While there was uncertainty associated with spatial inhomogeneities and this spatial averaging, the averaged emission spectra are representative of the overall plasma, as shown in literature [44, 54, 58, 64, 65]. Accordingly, the spatial-averaged light was sufficient for the results presented herein, which were results for the overall plasma. However, it was important to analyze the uncertainty due to spectral and temporal averaging used in data processing.

The averaged dark-subtracted spectrum shown in Figure 6.5 was used for the experimentally-determined line ratios rather than the raw emission spectra. The average spectrum, representative of all emission spectra at each given time in the plasma's lifetime, was generated by averaging 20 raw light spectra and subtracting the average of 20 raw dark spectra. To investigate the effects of spectra emission averaging, over 10000 different light and dark spectra were analyzed – 20 raw emission spectra for 51 time delays of 10 randomly chosen test conditions. Figure 6.24 shows example light and dark spectra, each type with 20 raw emission spectra and the calculated average spectra. A bound on maximum uncertainties of 12% and 3% were calculated for the average light and dark spectra, respectively, by looking at the “worst-case” differences between the average and raw spectra. The overall uncertainty for spectra averaging is  $< 12\%$ , as calculated with a geometric mean for uncorrelated uncertainties [71].

The other critical averaging step was in the line ratio analysis where the  $T_e$  and  $n_e$  values corresponding to each Ar I to Ar II intensity line ratio of a given time (as detailed in Tables 6.4 and 6.5) were averaged to obtain the time-resolved  $T_e$  and  $n_e$ . An analysis was conducted to determine bounds on the effect of averaging the emission spectra and line ratios on the final  $T_e$  and  $n_e$  values. It is important to note that different line ratios have differing sensitivities to  $T_e$  and  $n_e$  [56]. Therefore, the collective uncertainty was determined empirically using an analysis that tracked five test conditions through the entire

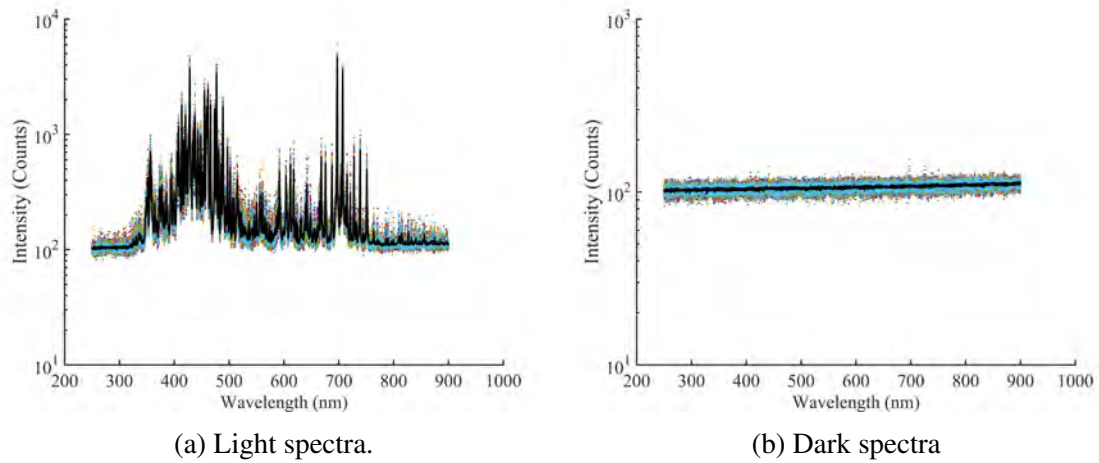


Figure 6.24: 20 individual raw emission spectra at a given delay time and the averaged emission spectra (in black).

process shown in Figure 6.5 to calculate the maximal effects averaging would have on  $T_e$  and  $n_e$ . Results of the tracked process for the 12 kV, 1 kHz, 1 Torr test condition from Group 4 in Table 6.2 are detailed in Figure 6.25.

Figure 6.25 illustrates the electron temperature and electron number density calculated from the averaged line ratio of each of the 20 individual emission spectra for a given delay time. The error bars represent the standard deviation calculation of individual line ratios for each spectrum.  $T_e$  and  $n_e$  values and standard deviation of individual line ratios as calculated from the average emission spectrum (i.e.,  $1.39 \text{ eV} \pm 0.041 \text{ eV}$  and  $5.45 \times 10^{14} \text{ cm}^{-3} \pm 7.80 \times 10^{12} \text{ cm}^{-3}$ ) were shown as solid red and dotted lines respectively. The solid red line also represented the values of  $T_e$  and  $n_e$  used in the time-resolved, nanosecond-pulsed plasma analysis in Section 6.4.

In all tests analyzed,  $> 95\%$  of the electron temperature and number density from all individual spectra were within the standard deviation bounds of the calculated values from the averaged emission spectra. That is, each individual emission spectrum was within the error bound for the average value with a probability  $P \geq 0.95$ . It was therefore justified to use the averaged emission spectra for  $T_e$  and  $n_e$  line ratio calculations with confidence to within the standard deviation. The averaged result was used to help suppress random

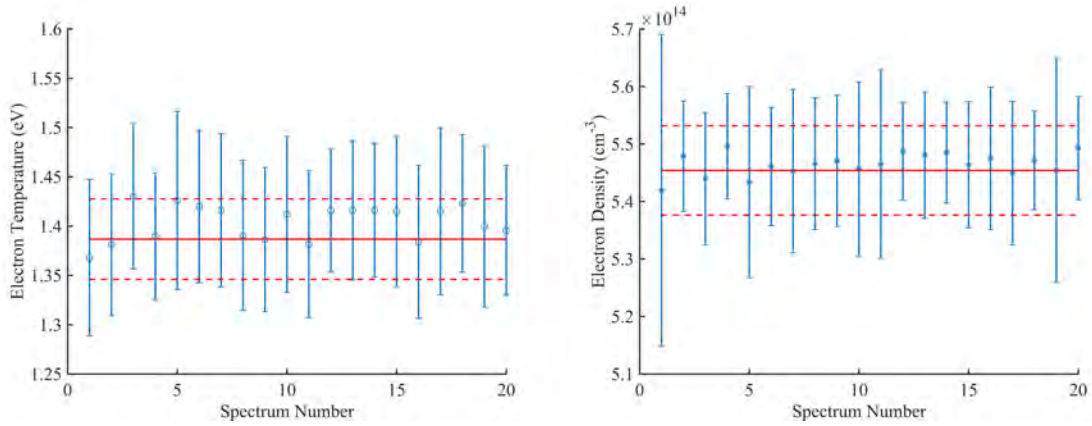


Figure 6.25: Spread of 20  $T_e$  and  $n_e$  values from each emission spectra at a given delay time and test condition (blue markers) and  $T_e$  and  $n_e$  values and standard deviation from the averaged spectra (solid and dotted red lines).

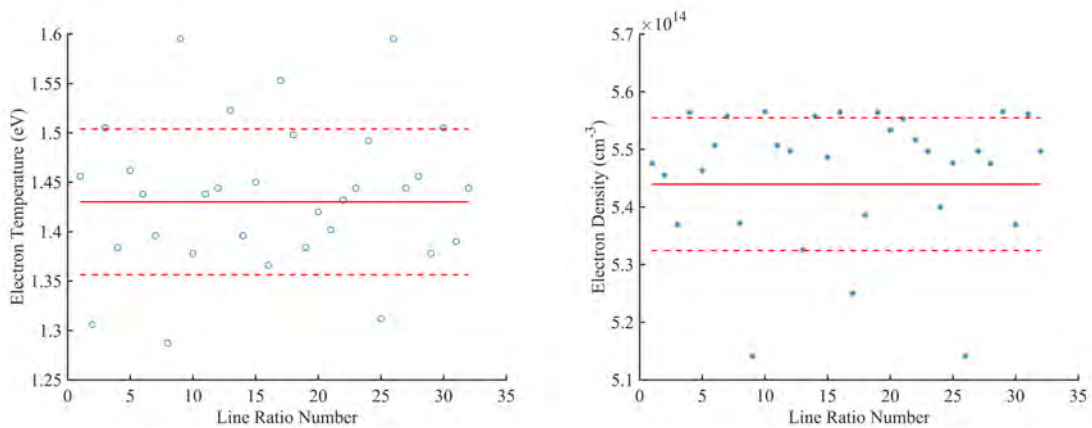


Figure 6.26: Spread of  $T_e$  and  $n_e$  values from individual line ratios of a given emission spectrum (blue markers) and  $T_e$  and  $n_e$  values and standard deviation from averaged line ratio (solid and dotted red lines).

errors in this measurement. The maximum uncertainty bound was 11% and 8% for electron temperature and density respectively.

Another analysis was conducted for the uncertainty bound in line ratio averaging.  $T_e$  and  $n_e$  were calculated for each individual line ratio of a dark-subtracted emission spectrum. Figure 6.26 shows the results from a single emission spectrum from the same test condition (12 kV, 1 kHz, 1 Torr) as above. The mean and standard deviation of the electron temperature and density values for individual line ratios were represented by the red solid and red dotted lines, respectively. Greater than 75% of all analyzed  $T_e$  line ratio sets and > 85% of  $n_e$  line ratio sets were within the standard deviation bounds of the averaged line ratio. With a maximum uncertainty bound of 14% and 7% for electron temperature and density respectively, it was justified to use  $T_e$  and  $n_e$  measurements from the averaged line ratio instead of individual line ratios for the time-resolved analysis.

The following additional uncertainties were estimated from literature: spectra distortion through the glass tube ( $\sim 5\%$ ), wavelength and intensity calibration source and actual calibration ( $\sim 3\%$ ), intensity calibration source and actual calibration from 300-750 nm ( $\sim 5\%$ ), instrument broadening (1%), peak wavelength-matched intensities (5-10%), PrismSPECT modeling (1-10%) [44, 56, 58, 69]. From all the uncertainties listed in this subsection, a maximum bound on the overall uncertainty for  $T_e$  and  $n_e$  was therefore estimated to be 27% and 23%, respectively.

## CHAPTER 7

### CONCLUSIONS & FUTURE WORK

The work detailed in this dissertation explores the ability to use an ICCD-spectrometer assembly to obtain time-resolved spectroscopy data for a nanosecond-pulsed plasma. The emission data were analyzed with the line ratio method to determine the nanosecond time evolution of electron density, electron temperature, and plasma frequency for nanosecond pulsed plasmas. The plasmas were generated using a wide range of operating conditions with varying discharge voltage, pulse frequency, and argon pressure to confirm the parameters needed for a functional VLF plasma antenna cell. Results indicated that any of the plasmas generated indeed had sufficiently rapid ionization and recombination times in the tens of nanoseconds as well as a sufficiently high plasma frequency in the hundreds of GHz to be used in a VLF plasma antenna. Trends discovered in testing could inform plasma antenna design based on desired characteristics and create an optimized pulsed plasma to switch rapidly between acting as a conductor and acting as a dielectric.

While using OES with line ratio analysis to calculate plasma parameters is not new, using it to research plasmas on the nanosecond timescale is. The major contribution of this dissertation was to measure and analyze the time evolution of plasma parameters through the lifetime of a pulsed, argon plasma discharge to increase understanding of nanosecond-pulsed plasma dynamics.

Further investigations into the physics of nanosecond-pulsed plasmas could include varying electrode geometry and gas selection as discussed in Chapter 2. Gas selection is a critical variable in determining breakdown voltages and reaction processes within a plasma, so changing gas properties to a lighter inert gas, such as helium, or to a mixture of gases, such as a Penning mixture or an inert gas/oxygen mixture, would affect the plasma parameters as well as ionization and recombination times of the plasma. Examining the

effects of electrode geometry and gas selection would give additional flexibility in the plasma antenna design. Relating peak wavelengths to exact line transitions and processes would also give more detailed insight into the plasma excitation, ionization, recombination, de-excitation, and metastable species generation of pulsed plasmas. Additional future work would entail developing the signal propagation technology needed for transmission through the plasma antenna cell.

# Appendices

**APPENDIX A**  
**ACTON SP-308 CALIBRATION**

See the procedures for WinSpec spectrometer calibration, wavelength calibration, and intensity calibration on the following pages.

## VAIPER Spectrometer Calibration Procedure

### Overall Calibration Procedure

1. Conduct SP-308 wavelength calibration in WinSpec.
2. Conduct wavelength calibration.
3. Conduct intensity calibration.
4. Run wavelength calibration code in MATLAB.
5. Run intensity calibration code in MATLAB.

### WinSpec Wavelength Calibration Procedure for SP-308

1. Follow the Spectrometer Calibration procedure listed in the WinSpec manual.
  - a. Once the calibration has been completed, **FULLY CLOSE** the WinSpec program so the new calibration values are saved. **If WinSpec crashes before this step, all the new calibrations will be lost.**
  - b. Re-open WinSpec and continue with the rest of the calibrations.

### Wavelength Calibration Procedure

2. Align SP-308 and Mercury-Argon source
  - a. Place Mercury-Argon Source (HG-1 from OceanOptics) on platform on opposite side of the glass plasma cell as the SP-308.
  - b. Align HG-1 so light source directly enters SP-308 slit.
3. Set WinSpec parameters
  - a. Set Gain = 100, number scans = 20, and gates/scan = 1.
    - i. See “Experimental Procedure” for details on how to set those values.
  - b. Set a ROI with a height of 15-20 pixels.
  - c. Calibration files will be split into “Mercury” and “Argon” due to large differences in intensities
4. Mercury calibration
  - a. Set PTG “Trigger” to “Internal Trigger”
  - b. Set PTG “Gate Time” to 0.1 ms.
  - c. For dark spectra, set “Name” = “waveDarkHg” and take dark spectra.
    - i. Cover the slit of the SP-308 with a dark cloth/cover.
  - d. For light spectra, set “Name” = “waveLightHg” and take light spectra.
    - i. Uncover slit of SP-308.
5. Argon calibration
  - a. Set PTG “Gate Time” to 6 ms.
  - b. For dark spectra, set “Name” = “waveDarkAr” and take dark spectra.
    - i. Cover the slit of the SP-308 with a dark cloth/cover.
  - c. For light spectra, set “Name” = “waveLightAr” and take light spectra.
    - i. Uncover slit of SP-308.

6. Save files as ASCII files
  - a. See “Experimental Procedure” for details.
7. Update test log

### Intensity Calibration Procedure

1. Align SP-308 and tungsten light
  - a. Turn on Tungsten light and **WAIT 20 MINUTES** for bulb to warm up. As light heats up, spectrum shifts toward shorter, higher energy wavelengths.
  - b. Note the time and ambient temperature that the Tungsten light turned on in test log.
2. Set WinSpec parameters
  - a. Set Gain = 100, number scans = 20, and gates/scan = 1.
    - i. See “Experimental Procedure” for details on how to set those values.
  - b. Set a ROI with a height of 15-20 pixels.
3. Take calibration data
  - a. Set PTG “Gate Time” to 20 us.
  - b. For dark spectra, set “Name” = “intensityDark” and take dark spectra.
    - i. Cover the slit of SP-308 with a dark cloth/cover.
  - c. For light spectra, set “Name” = “intensityLight” and take light spectra.
    - ii. Uncover slit of SP-308.
4. Save files as ASCII files
  - a. See “Experimental Procedure” for details.
5. Update test log

**APPENDIX B**  
**EXPERIMENTAL PROCEDURE**

See the time-resolved, nanosecond-pulsed plasma procedure on the following pages.

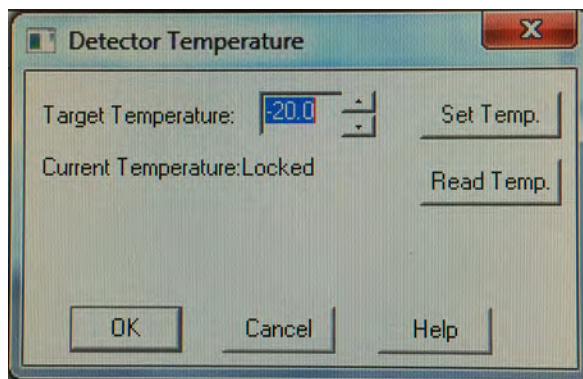
## VAIPER Nanosecond-Pulsed Plasma Testing Procedure

This procedure below is indicative of what I did to run my experiments and may be modified as necessary for future testing.

1. Secure blackout curtains over the windows and ensure there is minimal stray light in the test area. Place a testing sign outside the room (sample sign below).



2. Ensure all hardware components are secured and all diagnostics, power supplies, mass flow controllers, etc. are operational.
3. Turn on PI-MAX controller and SP-308 spectrometer.
4. Open WinSpec and click "Revert to Previous Settings" if using previous calibration settings. Otherwise, perform a spectrometer calibration.
5. In WinSpec, **set the detector target temperature to be -20.0 C**. When the detector is locked, the window will show "Locked," and the green "TEMP LOCK" indicator light on the PI-MAX controller will be illuminated.

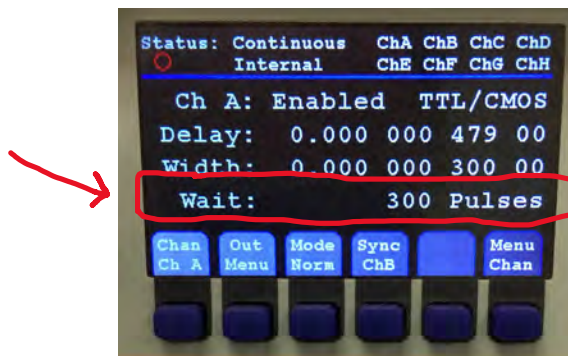


6. Perform wavelength and intensity calibrations.
7. Turn on the vacuum pump with the roughing valve and vent valve closed. Let pump warm up for 10-15 minutes.

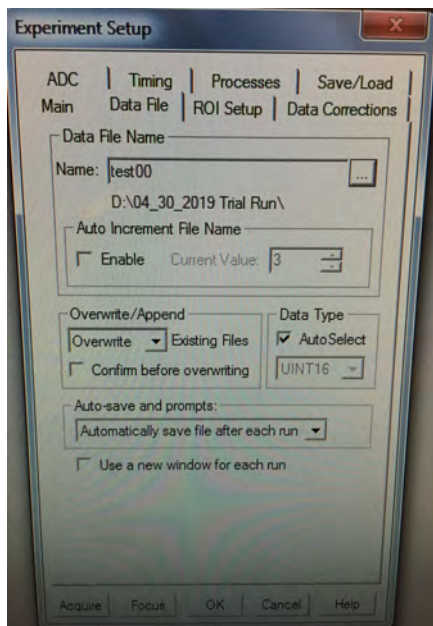
8. Open roughing valve  $\sim\frac{1}{2}$  turn to allow pressure drop. Note base pressure in test log (should be 50-100 mTorr).
9. In order, open the argon bottle, the argon regulator valve, and the green manual valve.
10. Turn on mass flow controller (MFC) if not already on.
11. Turn on oscilloscope and verify all probes and diagnostics are connected to their respective channels.
12. Set oscilloscope to "Normal" mode with a timebase of 50.0 ns/div, 1.25 kS, and 2.5 GS/s.
13. Set oscilloscope trigger to 2.00 V on the positive edge of the gate monitoring signal channel.
14. Turn on the delay generator and verify T0 is set to the desired plasma pulse frequency for that given test.



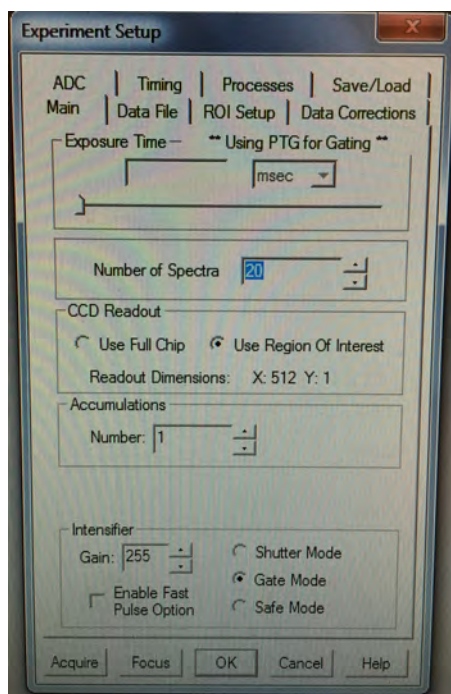
15. Calculate the appropriate number of "Wait" pulses for Channel A (the PI-MAX controller).



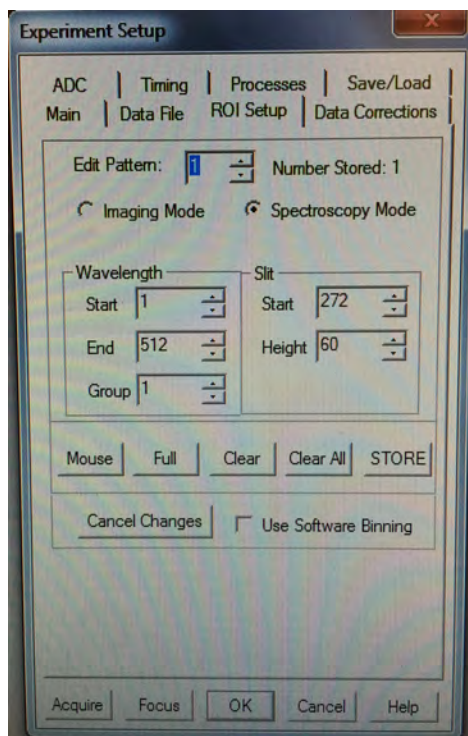
16. Verify the high-voltage differential probe leads are firmly connected to the resistive voltage divider.
17. Verify the NSP leads are connected to air-side power flanges and there is sufficient Kapton tape between leads to prevent arcing.
18. Turn on the NSP, FT-1, and photodiode.
19. Create a new test data folder (i.e., MM\_DD\_YYYY Description) on test computer with Winspec application.
20. In Winspec, go to Acquisition → Experimental Setup → Data File → point to folder created in Step 18 and set "Name" to test00.
  - a. Match the rest of the properties to the figure below.



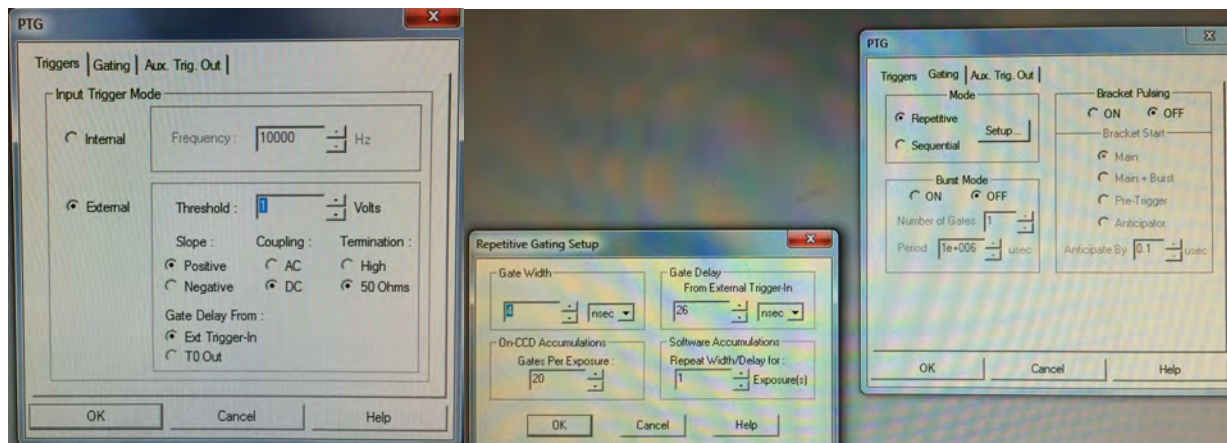
21. Set the “Main” tab in Experimental Setup to the same parameters as shown in the following figure.



22. Set the “ROI Setup” tab in Experimental Setup. Define the ROI slit if you already know the numbers. Otherwise, wait and we’ll come back to this.



23. Set the high voltage setup and repetitive gating setup to the appropriate values (see figures).



24. Set gain to 255 if at pressure of 1-Torr argon. Otherwise, need to decrease it (will know from previous experience what gain to set so maximum spectral peaks don't saturate out intensity of spectrometer)

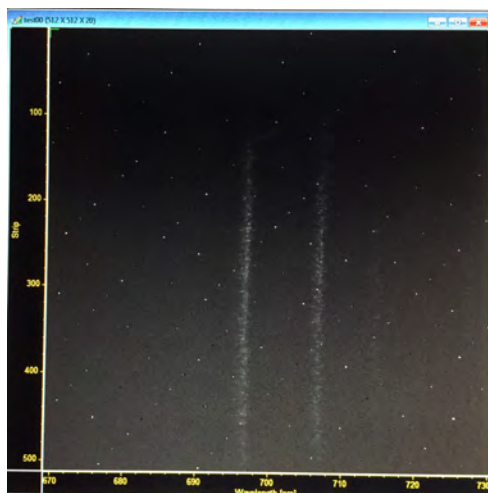
25. Allow MFC to start flowing argon gas and set the target pressure (however the pressure is maintained – by flicking MFC switch or through the Arduino).

26. Hit run on the pulse delay generator and turn off the lights.

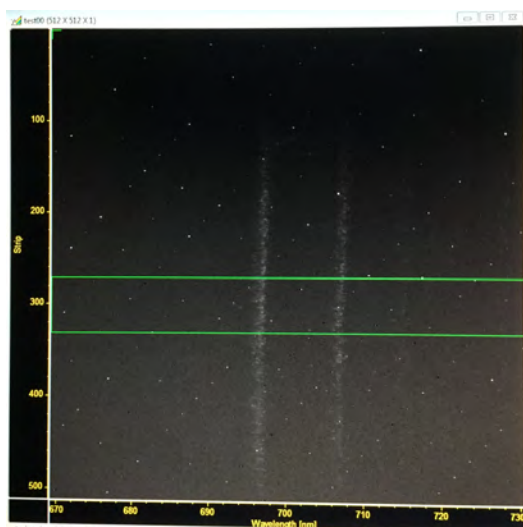
27. Output the NSP and slowly tick up voltage using coarse adjustment (and then fine adjustments if going up to 20 kV) until the desired voltage output.

28. Using Spectrometer → Move, move the spectrometer to a desired target wavelength (i.e. 700 nm) to look at the plasma. Click focus.

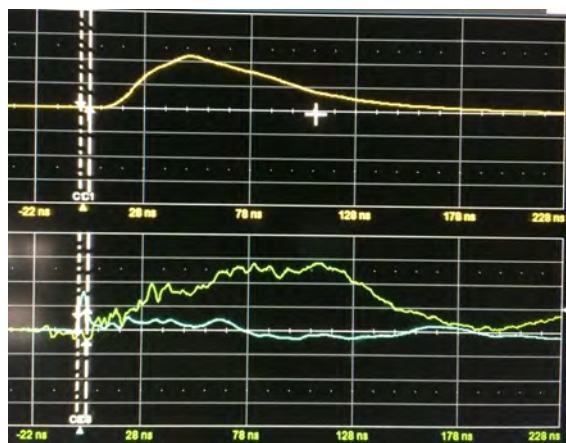
29. If full chipped (like the figure below), need to set up ROI.



a. Click stop on “Focus.” Then, Easy Bin → Set ROI so it looks like the following figure

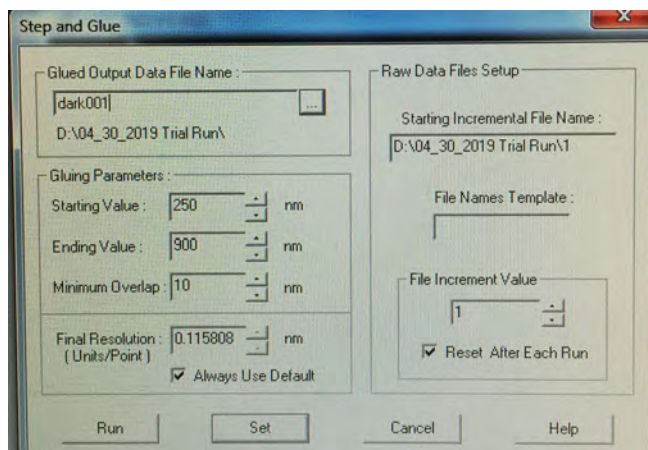


30. Move to beginning of the pulse delay time on delay generator (i.e., see figure of an example beginning oscilloscope trace)

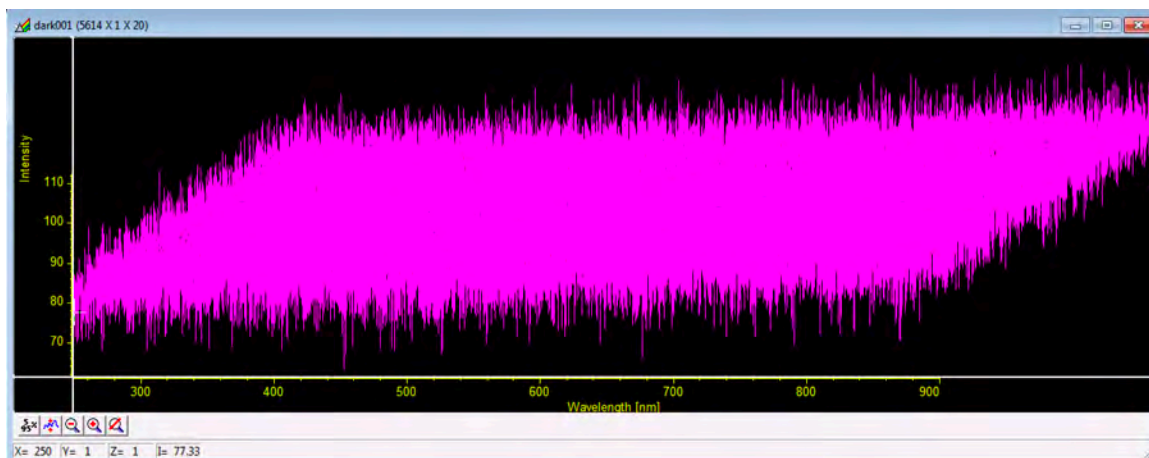


31. Fill Test Log with information.

32. Acquisition → Step & Glue → point to correct folder → dark001

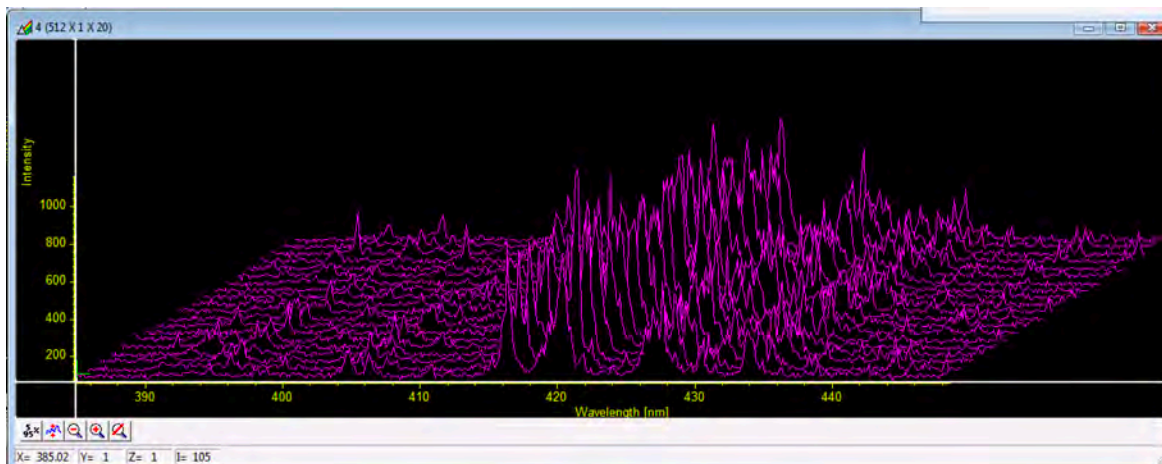


- a. Place a dark cloth/cover over the spectrometer slit and take a dark spectrum.
- b. Take a dark spectrum after every 10 tests (so dark001, dark011, dark021, etc.).
- c. Example of a good step & glue dark spectrum below

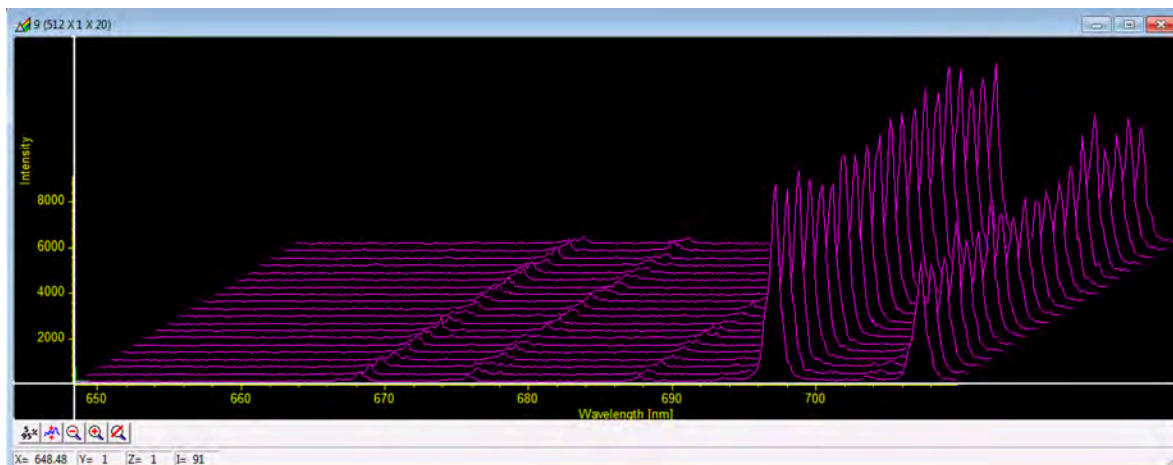


33. Keeping the same delay time, remove the cloth/cover, auto-save the waveforms on the oscilloscope (“Fill”), and take a light spectrum.

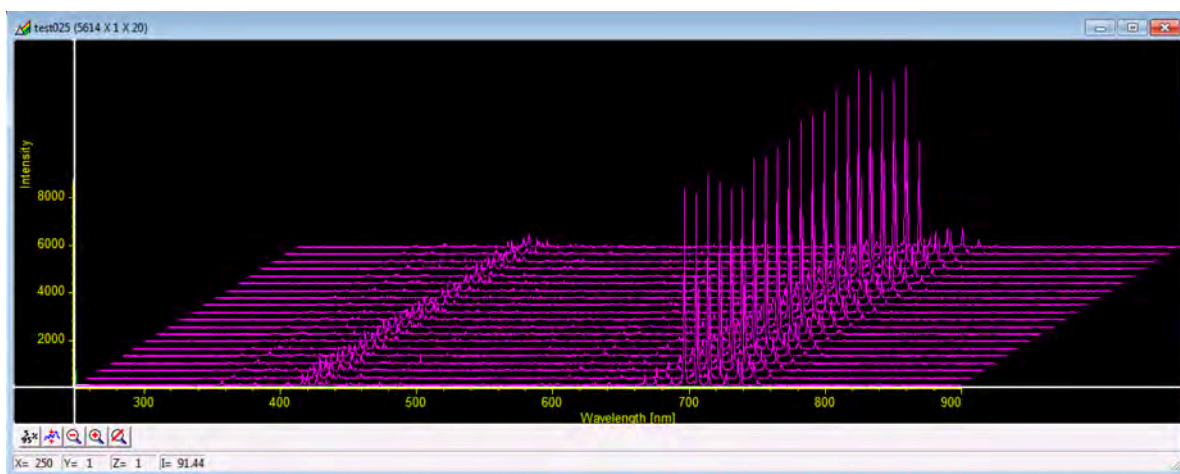
- a. Take an oscilloscope trace for the light spectrum after every dark spectrum.
- b. Example of a good light spectrum below (step 4 of step & glue) – seeing ion peaks



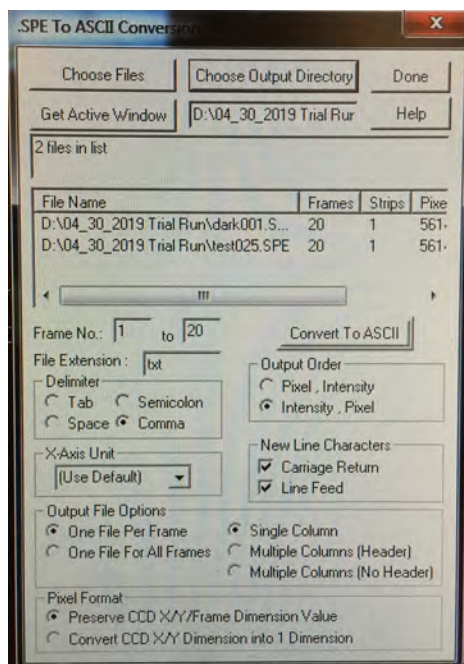
c. Example of a good light spectrum below (step 9 of step & glue) – seeing neutral peaks



d. Example of a good step & glue light spectrum



34. Move the delay generator delay time by 2 ns (until 80% of the photodiode width sweep; then, move by 4 ns each time).
35. Continue the rest of testing.
36. At the end of testing, slowly tick voltage back down to 0 in 2 kV increments (or fine adjustment first, then coarse adjustment).
37. Stop delay generator from running. Then, stop mass flow.
38. Tools → Convert to ASCII (see below figure).



39. Let everything cool down for 30-45 minutes before the next test. Otherwise continue to shutdown procedure below.
40. Turn off the NSP, MFC, delay generator, oscilloscope, and photodiode.
41. Put a cover over the lens and across the spectrometer slit.
42. Turn off argon propellant line in reverse order as turn-on (i.e., green valve, regulator valve, gas bottle).

## APPENDIX C

### DATA PROCESSING

The following code flowcharts describe the major MATLAB codes that were used for data processing: obtaining wavelength and intensity calibrations, experimental peak finding, calculating experimental line ratios, and matching those line ratios to PrismSPECT-generated ratios to calculate experimentally-determined electron density, electron temperature, and plasma frequency.

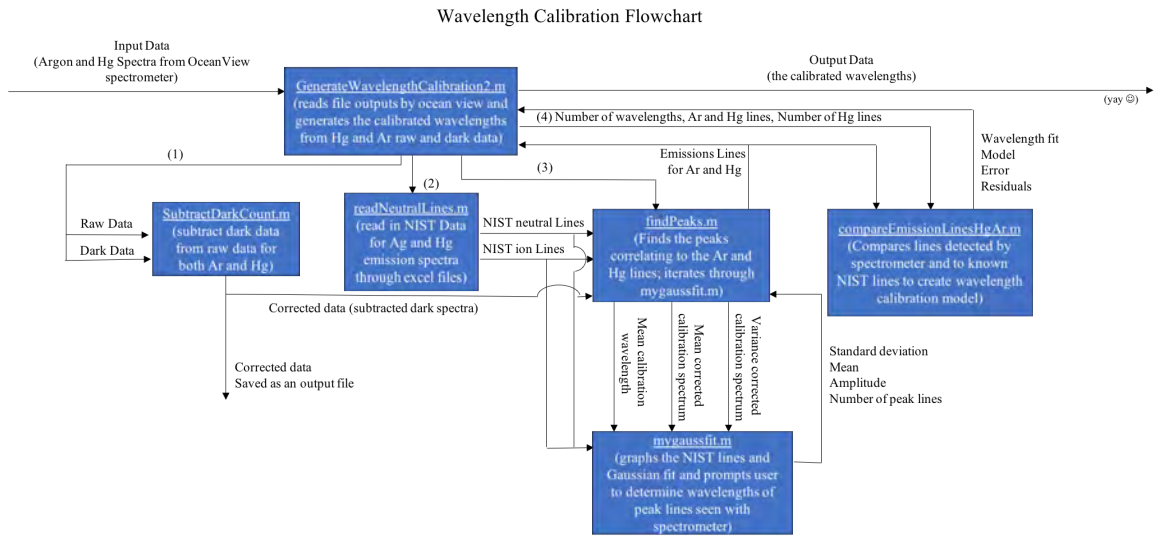


Figure C.1: Taking spectra from wavelength calibrations and calculating appropriate wavelength corrections for experimental spectra.

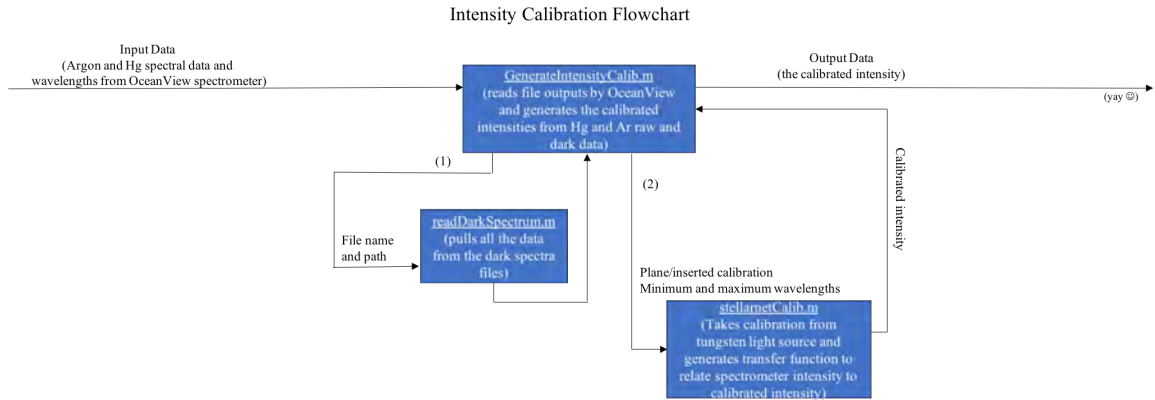


Figure C.2: Taking spectra from intensity calibrations and calculate appropriate intensity corrections for experimental spectra.

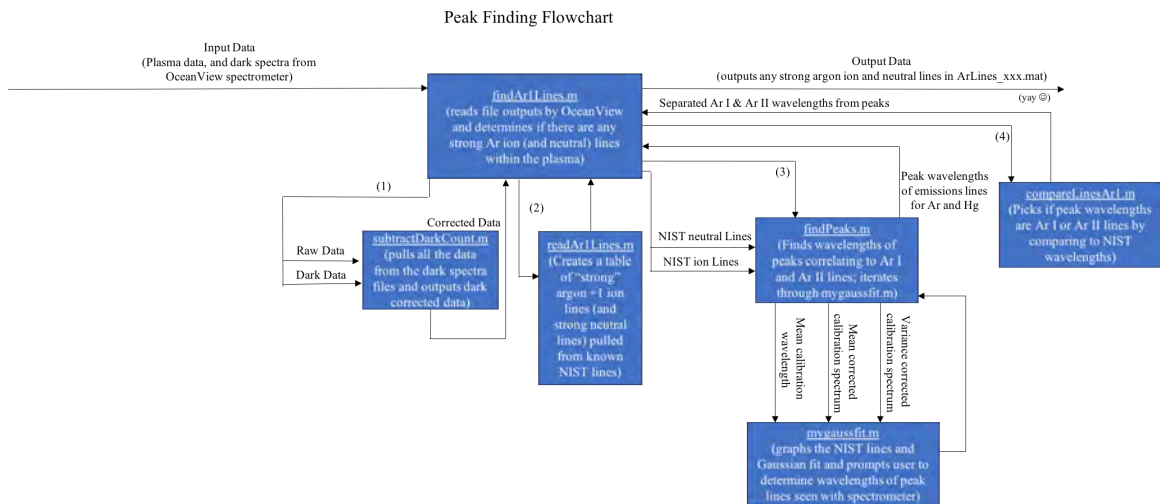


Figure C.3: Taking spectra from nanosecond-pulsed plasma, finding strong Ar I and Ar II peaks, and outputting those peaks' wavelengths and intensities.

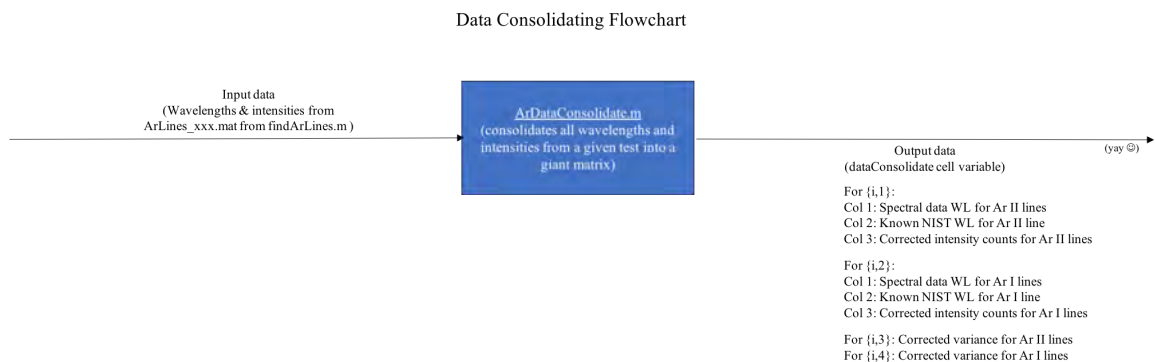


Figure C.4: Consolidating all peak wavelengths and intensities from a given test.

### Line Ratio Flowchart

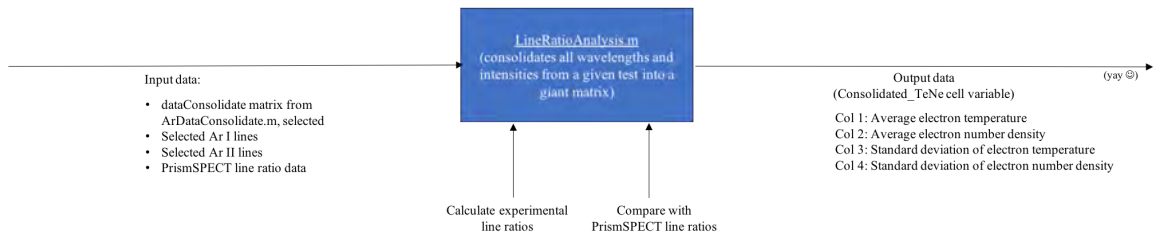


Figure C.5: Calculating experimental line ratios and comparing them to PrismSPECT-generated line ratios.

## APPENDIX D

### PI-MAX TROUBLESHOOTING

A few tips for troubleshooting the PI-MAX (and the biggest problems that I encountered while using it):

- **If a camera beeps in the middle of testing and temperature lock has been lost:**
  - Immediately stop testing and turn the gate intensifier off.
  - If the temperature has become unlocked (either from the window no longer showing “Locked” or the green light on the PI-MAX controller going off), close WinSpec and turn the PI-MAX controller off. Verify that the USB cable connecting the controller to the computer is firmly attached on both ends. Turn the PI-MAX controller on. Reopen WinSpec and keep an eye on the temperature lock. If the value is decreasing once more, keep watching until it locks (because sometimes it drops in temperature towards the target temperature and then immediately climbs back up). If the temperature has been locked, turn the intensifier on, and continue testing.
  - Check the temperature of the room – if it is too hot, the camera will not reach target temperature lock until it is cooler or use fans close to the controller
  - If the temperature is still not locked (or has reached  $> 10^{\circ}$  C), ‘close WinSpec and turn off the PI-MAX controller for at least 5 minutes. Try again.
  - If still nothing, close WinSpec, turn off the PI-MAX controller, and restart the WinSpec computer. Try again.
  - If still nothing, shut down the experiment and try again in a few hours. If the issue hasn’t resolved itself in a few hours, look at the PI-MAX manual or contact PI-MAX technical support.

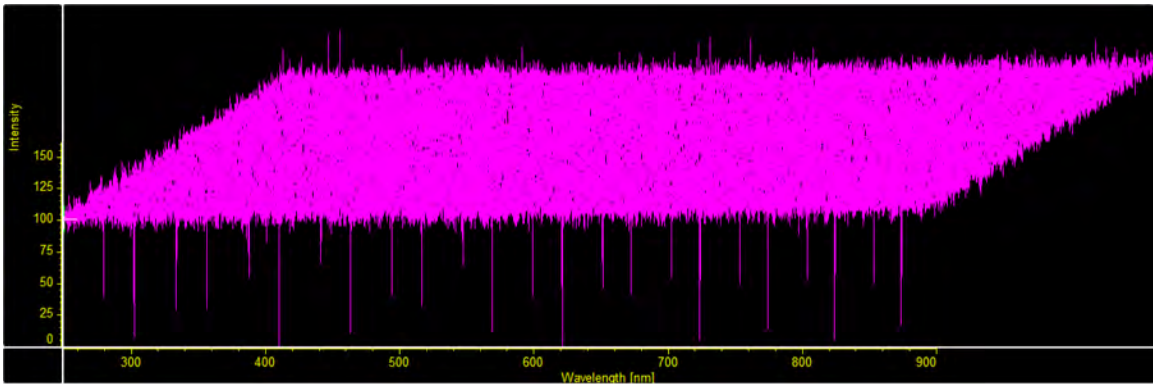


Figure D.1: Measured dark spectra with large periodic noise.

- **If a camera beeps in the middle of testing and PTG control on WinSpec has been lost:**
  - Stop testing and turn the gate intensifier off.
  - Turn intensifier back on and check if PTG control has been regained.
  - If not, turn intensifier back off. Close WinSpec and turn off PI-MAX controller. Verify that the large data and signal cables from the controller to the camera are securely connected. Try again.
  - If still nothing, close WinSpec, turn off the PI-MAX controller, and restart the WinSpec computer. Try again.
  
- **If there are periodic spikes in the dark spectrum (like in Figure D.1):**
  - Is your pulse frequency  $\geq 1$  kHz? If so, it's fine – it's background noise from the spectrometer and will subtract out with the measured light spectra, so the data is still valid. The speckled background seen in Figure D.2 exists even without any plasma generation.
  - If not, check if there's noise from the nanosecond pulser or surrounding electronics.

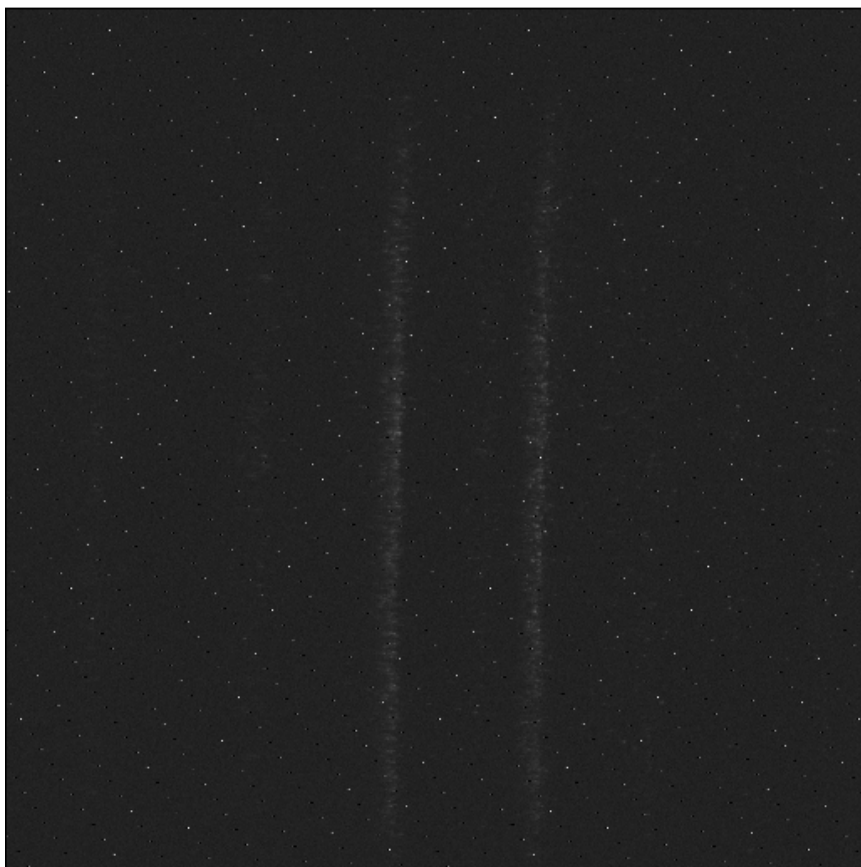


Figure D.2: Speckled background of spectrometer causing large periodic noise.

## APPENDIX E

### NSP TROUBLESHOOTING

A selected list of tips and checks for successfully measuring the NSP voltage waveform is given below (adapted from [50]):

- If the FT-1 is not triggering the NSP, increase the voltage pulse provided by the delay generator to the FT-1.
- Beware of stray capacitance leading to ringing in the voltage waveforms.
  - Check the length of the leads (i.e. are there several meters of lead?)
- Check if a proper voltage divider has been made.
  - All real resistors have associated parasitic capacitance and inductance. How much is in the resistors being used in the voltage divider?
  - Resistance of resistors subject to high voltage nanosecond pulses may be up to 30% lower than their rated DC value, and higher value resistors typically lose a greater percentage of their resistance. Are the resistors designed for pulsed applications? What is the “downrated” resistance value?
  - Can’t have too high of a resistance – the probe capacitance is usually 1-2 pF and the RC timescale should be  $\leq 10$  ns – so the resistor value is typically limited to 5-10 k $\Omega$ .
  - Current drawn by the voltage divider should be  $\ll$  the current drawn by the actual load.
  - Are resistors sized to handle the power passing through them (i.e., especially at high voltages?)

- Use an odd number of resistors and clip the probe across the central resistor.
- Don't use too many resistors in the divider; longer chains are more inductive, which more strongly distort the waveform.
- How to limit reflections in the measured voltage waveform:
  - Limit the length of the output cable. A “short” cable is when the propagation time of the signal through the cable is short compared to the signal's fastest characteristic timescale (e.g., rise time). For example, if a signal rises with a rise time of 10 ns, a cable must be shorter than 5 ft to be “short” since the signal propagation speed through the cable is  $v = c/\epsilon^{0.5}$ . If a longer cable must be used, the rise time can be slowed with more (larger) resistors.
  - Match the cable impedance to the load impedance. The impedance of a cable can typically be characterized as  $Z = (L/C)^{0.5}$ .
- Explicitly ground the oscilloscope.
- Prevent cables from crossing each other. Keep leads running close to and parallel to each other and without any loops.
- Lift diagnostics like the high-voltage differential probe off any metal surfaces by at least 6” to reduce stray capacitive coupling.
- Conduct a measurement test:
  1. Measure the signal purely across the resistor load and verify that the waveform is clean.
  2. Measure with the experimental load (i.e., the plasma cell) attached and verify that the waveform is clean. If noise is introduced, there may be stray EMI.

## REFERENCES

- [1] J. Bittencourt, *Fundamentals of Plasma Physics*, 3rd. Springer-Verlag, 2004.
- [2] A. Piel, *Plasma Physics: An Introduction to Laboratory, Space, and Fusion Plasmas*. Berlin: Springer-Verlag, Jun. 2010.
- [3] S. Yang, X. Gao, V. Yang, W. Sun, S. Nagaraja, J. K. Lefkowitz, and Y. Ju, “Nanosecond Pulsed Plasma Activated  $C_2H_4/O_2/Ar$  Mixtures in a Flow Reactor,” *Journal of Propulsion and Power*, vol. 32, no. 5, pp. 1240–1252, Sep. 2016.
- [4] A Roettgen, I Shkurenkov, M Simeni Simeni, I. V. Adamovich, and W. R. Lempert, “Time-Resolved Electron Temperature and Electron Density Measurements in a Nanosecond Pulse Filament Discharge in  $H_2-He$  and  $O_2-He$  Mixtures,” *Plasma Sources Science and Technology*, vol. 25, no. 5, pp. 055 008–12, Oct. 2016.
- [5] X Duten, D Packan, L Yu, C. O. Laux, and C. H. Kruger, “DC and Pulsed Glow Discharges in Atmospheric Pressure Air and Nitrogen,” *IEEE Transactions on Plasma Science*, vol. 30, no. 1, pp. 178–179, 2002.
- [6] S Hübner, J. M. Palomares, E. A. D. Carbone, and J. J. A. M. van der Mullen, “A Power Pulsed Low-Pressure Argon Microwave Plasma Investigated by Thomson Scattering: Evidence for Molecular Assisted Recombination,” *Journal of Physics D: Applied Physics*, vol. 45, no. 5, pp. 055 203–8, Jan. 2012.
- [7] X. Wen, Y. Xin, C. Feng, and H. Ding, “Simulations and Measurement of Electron Energy and Effective Electron Temperature of Nanosecond Pulsed Argon Plasma,” *Plasma Science and Technology*, vol. 14, no. 1, pp. 40–47, Jan. 2012.
- [8] J Alami, J. T. Gudmundsson, J Bohlmark, J Birch, and U Helmersson, “Plasma Dynamics in a Highly Ionized Pulsed Magnetron Discharge,” *Plasma Sources Science and Technology*, vol. 14, no. 3, pp. 525–531, 2005.
- [9] J Laimer, M Fink, T. A. Beer, and H Störi, “Plasma Dynamics as a Key to Successful Upscaling of Pulsed Plasma Processes,” *Surface and Coatings Technology*, vol. 174–175, pp. 118–123, Sep. 2003.
- [10] R. Liu, Y. Liu, W. Jia, and Y. Zhou, “Fluid Modeling of Plasma Dynamics in Pulsed RF Capacitive Glow Discharges in Low Pressure Argon,” *Physics of Plasmas*, vol. 24, no. 8, Aug. 2017.

- [11] M. Reckeweg and C. Rohner, "Antenna Basics," Rohde & Schwarz, Tech. Rep. 8GE01, Mar. 2015.
- [12] National Radio Astronomy Observatory, Antenna Theory. Available: <https://www.cv.nrao.edu/course/astr534/AntennaTheory.html>.
- [13] M. Cohen, "YIP: Very-short Antennas via Ionized Plasmas for Efficient Radiation (VAIPER)," Georgia Institute of Technology, Tech. Rep., 2015.
- [14] R. K. Said, U. S. Inan, and K. L. Cummins, "Long-Range Lightning Geolocation Using a VLF Radio Atmospheric Waveform Bank," *Journal of Geophysical Research*, vol. 115, no. D23, p. D05208, Dec. 2010.
- [15] M. B. Cohen, U. S. Inan, and E. W. Paschal, "Sensitive Broadband ELF/VLF Radio Reception With the AWESOME Instrument," *IEEE Transactions on Geoscience and Remote Sensing*, vol. 48, no. 1, pp. 3–17, 2010.
- [16] T. J. Cui, W. C. Chew, X. X. Yin, and W. Hong, "Study of Resolution and Super Resolution in Electromagnetic Imaging for Half-Space Problems," *IEEE Transactions on Antennas and Propagation*, vol. 52, no. 6, pp. 1398–1411, Jun. 2004.
- [17] H. D. Voss, M. Walt, W. L. Imhof, J. Mobilia, and U. S. Inan, "Satellite Observations of Lightning-Induced Electron Precipitation," *Journal of Geophysical Research: Space Physics*, vol. 103, no. A6, pp. 11 725–11 744, Jun. 1998.
- [18] U. S. Inan, F. A. Knifsend, and J. Oh, "Subionospheric VLF "imaging" of lightning-induced electron precipitation from the magnetosphere," *Journal of Geophysical Research*, vol. 95, no. A10, p. 17 217, 1990.
- [19] U. S. Inan, N. G. Lehtinen, R. C. Moore, K. Hurley, S. Boggs, D. M. Smith, and G. J. Fishman, "Massive Disturbance of the Daytime Lower Ionosphere by the Giant  $\gamma$ -Ray Flare from Magnetar SGR 1806-20," *Geophysical Research Letters*, vol. 34, no. 8, 2007.
- [20] *NAA Cutler Maine - Navy VLF Transmitter Site*, Jun. 2018.
- [21] A. D. Watt, *VLF Radio Engineering*, 1st. Pergamon Press, 1967.
- [22] G. G. Borg, J. H. Harris, D. G. Miljak, and N. M. Martin, "Application of Plasma Columns to Radio Frequency Antennas," *Applied Physics Letters*, vol. 74, no. 22, pp. 3272–3274, May 1999.

- [23] G. G. Borg, J. H. Harris, N. M. Martin, D Thorncraft, R Milliken, D. G. Miljak, B Kwan, T Ng, and J Kircher, “Plasmas as Antennas: Theory, Experiment and Applications,” *Physics of Plasmas*, vol. 7, no. 5, pp. 2198–2202, May 2000.
- [24] J. P. Rayner, A. P. Whichello, and A. D. Cheetham, “Physical Characteristics of Plasma Antennas,” *IEEE Transactions on Plasma Science*, vol. 32, no. 1, pp. 269–281, Feb. 2004.
- [25] I Alexeff, T Anderson, S Parameswaran, E. P. Pradeep, J Hulloli, and P Hulloli, “Experimental and Theoretical Results with Plasma Antennas,” *IEEE Transactions on Plasma Science*, vol. 34, no. 2, pp. 166–172, Apr. 2006.
- [26] I. Alexeff, T. Anderson, E. Farshi, N. Karnam, and N. R. Pulasani, “Recent Results for Plasma Antennas,” *Physics of Plasmas*, vol. 15, no. 5, pp. 057 104–5, May 2008.
- [27] T. Anderson, *Plasma Antennas*. Artech House, 2011.
- [28] R. Kumar and D. Bora, “A Reconfigurable Plasma Antenna,” *Journal of Applied Physics*, vol. 107, no. 5, pp. 053 303–10, Mar. 2010.
- [29] ———, “Wireless Communication Capability of a Reconfigurable Plasma Antenna,” *Journal of Applied Physics*, vol. 109, no. 6, pp. 063 303–10, Mar. 2011.
- [30] G. A. Emmert and M. A. Henry, “Numerical Simulation of Plasma Sheath Expansion, with Applications to Plasma-Source Ion Implantation,” *Journal of Applied Physics*, vol. 71, no. 1, pp. 113–117, Aug. 1998.
- [31] C. Chan, “Experimental Investigation of Fast Plasma Production for the VAIPER Antenna,” Master’s thesis, Georgia Institute of Technology, Dec. 2017.
- [32] P. Singletary, “Optical Characterization Of A High Speed Plasma’s Electromagnetic Properties,” Master’s thesis, Georgia Institute of Technology, Apr. 2018.
- [33] Y Celik, M Aramaki, D Luggenhölscher, and U Czarnetzki, “Determination of Electron Densities by Diode-Laser Absorption Spectroscopy in a Pulsed ICP,” *Plasma Sources Science and Technology*, vol. 20, no. 1, pp. 015 022–13, Jan. 2011.
- [34] S Iordanova and I Koleva, “Optical Emission Spectroscopy Diagnostics of Inductively-Driven Plasmas in Argon Gas at Low Pressures,” *Spectrochimica Acta Part B: Atomic Spectroscopy*, vol. 62, no. 4, pp. 344–356, Apr. 2007.
- [35] *High Voltage Pulse Generator FPG 1-50NM100A Operating Manual*, FID GmbH, 2016.

- [36] *NSP-30/60/120-5/10/20/30-F/P/N-250/500 User's Manual*, Eagle Harbor Technologies, 2016.
- [37] *HR4000 and HR4000CG-UV-NIR Series Spectrometers Installation and Operation Manual*, OceanOptics, 2008.
- [38] A. Kramida, Yu. Ralchenko, J. Reader, and NIST ASD Team, NIST Atomic Spectra Database (ver. 5.5.6), [Online]. Available: <https://physics.nist.gov/asd> [2018, August 7]. National Institute of Standards and Technology, Gaithersburg, MD. 2018.
- [39] A Roettgen, I Shkurenkov, M Simeni Simeni, V Petrishchev, I. V. Adamovich, and W. R. Lempert, "Time-Resolved Electron Density and Electron Temperature Measurements in Nanosecond Pulse Discharges in Helium," *Plasma Sources Science and Technology*, vol. 25, no. 5, pp. 055 009–14, Oct. 2016.
- [40] F. Chen, "Langmuir Probe Diagnostics," University of California, Los Angeles, Tech. Rep., Jun. 2003.
- [41] R. Manoharan, T. K. Boyson, and S. O'Byrne, "Time-Resolved Temperature and Number Density Measurements in a Repetitively Pulsed Nanosecond-Duration Discharge," *Physics of Plasmas*, vol. 23, no. 12, pp. 123 527–10, Dec. 2016.
- [42] B. T. Yee, B. R. Weatherford, E. V. Barnat, and J. E. Foster, "Dynamics of a Helium Repetitively Pulsed Nanosecond Discharge," *Journal of Physics D: Applied Physics*, vol. 46, no. 50, p. 505 204, Nov. 2013.
- [43] W. Zhou, K. Li, X. Li, H. Qian, J. Shao, X. Fang, P. Xie, and W. Liu, "Development of a Nanosecond Discharge-Enhanced Laser Plasma Spectroscopy," *Optics Letters*, vol. 36, no. 15, pp. 2961–2963, 2011.
- [44] X.-M. Zhu, J. L. Walsh, W.-C. Chen, and Y.-K. Pu, "Measurement of the Temporal Evolution of Electron Density in a Nanosecond Pulsed Argon Microplasma: Using Both Stark Broadening and an OES Line-Ratio Method," *Journal of Physics D: Applied Physics*, vol. 45, no. 29, pp. 295 201–12, Jul. 2012.
- [45] *PI-MAX/PI-MAX2 System*, Princeton Instruments.
- [46] *4 Quik E: High Speed ICCD Camera*, Stanford Computer Optics, 2013.
- [47] *Operating Instructions: Acton SP-300i*, Princeton Instruments.
- [48] *WinSpec: Spectroscopy Software, 2.6B*, Princeton Instruments, 2012.

- [49] F Schwirzke, M. P. Hallal, and X. K. Maruyama, “Explosive Plasma Formation On Electrodes,” in *Eighth IEEE International Conference on Pulsed Power*, IEEE, 1991, pp. 663–666.
- [50] I. Slobodov, “High Voltage Nanosecond Pulse Measurement Techniques,” Eagle Harbor Technologies, Tech. Rep., 2016.
- [51] H. R. Griem, *Principles of Plasma Spectroscopy*. Cambridge University Press, Feb. 2005.
- [52] J Cooper, “Plasma Spectroscopy,” *Reports on Progress in Physics*, vol. 29, no. 1, pp. 35–130, 1966.
- [53] M Numano, “Criteria for local thermodynamic equilibrium distributions of populations of excited atoms in a plasma,” *Journal of Quantitative Spectroscopy and Radiative Transfer*, vol. 43, no. 4, pp. 311–317, 1990.
- [54] K Kano, M Suzuki, and H Akatsuka, “Spectroscopic Measurement of Electron Temperature and Density in Argon Plasmas Based on Collisional-Radiative Model,” *Plasma Sources Science and Technology*, vol. 9, no. 3, pp. 314–322, 2000.
- [55] B van der Sijde, J. J. A. M. van der Mullen, and D. C. Schram, “Collisional Radiative Models in Plasmas,” *Beiträge aus der Plasmaphysik*, vol. 24, no. 5, pp. 447–473, 1984.
- [56] S. Siepa, S. Danko, T. V. Tsankov, T. Mussenbrock, and U. Czarnetzki, “On the OES Line-Ratio Technique in Argon and Argon-Containing Plasmas,” *Journal of Physics D: Applied Physics*, vol. 47, no. 44, pp. 445 201–17, Oct. 2014.
- [57] A. Bogaerts, R. Gijbels, and J. Vlcek, “Collisional-Radiative Model for an Argon Glow Discharge,” *Journal of Applied Physics*, vol. 84, no. 1, pp. 121–136, Jul. 1998.
- [58] X. M. Zhu, Y. K. Pu, N Balcon, and R Boswell, “Measurement of the Electron Density in Atmospheric-Pressure Low-Temperature Argon Discharges by Line-Ratio Method of Optical Emission Spectroscopy,” *Journal of Physics D: Applied Physics*, vol. 42, no. 14, p. 142 003, 2009.
- [59] R. McWhirter and A. Hearn, “A Calculation of the Instantaneous Population Densities of the Excited Levels of Hydrogen-like Ions in a Plasma,” *Proceedings of the Physical Society*, vol. 82, no. 5, pp. 641–654, 1963.
- [60] T. Fujimoto, “Kinetics of Ionization-Recombination of a Plasma and Population Density of Excited Ions,” *Journal of the Physical Society of Japan*, vol. 47, no. 1, pp. 265–281, 1979.

- [61] A. M. Gomes, “Criteria for Partial LTE in an Argon Thermal Discharge at Atmospheric Pressure; Validity of the Spectroscopically Measured Electronic Temperature,” *Journal of Physics D: Applied Physics*, vol. 16, no. 3, pp. 357–378, Nov. 2000.
- [62] H. R. Griem, *Spectral Line Broadening by Plasmas*, ser. Pure and Applied Physics. Academic Press, 1974, vol. 39.
- [63] G. V. Marr, *Plasma Spectroscopy*. Elsevier Publishing Company, 1968.
- [64] R. M. van der Horst, T Verreycken, E. M. van Veldhuizen, and P. J. Bruggeman, “Time-Resolved Optical Emission Spectroscopy of Nanosecond Pulsed Discharges in Atmospheric-Pressure  $N_2$  and  $N_2/H_2O$  mixtures,” *Journal of Physics D: Applied Physics*, vol. 45, no. 34, pp. 345 201–12, Aug. 2012.
- [65] S Yugeswaran and V Selvarajan, “Electron Number Density Measurement on a DC Argon Plasma Jet by Stark Broadening of Ar I Spectral Line,” *Vacuum*, vol. 81, no. 3, pp. 347–352, 2006.
- [66] S Djurović and N Konjević, “On the Use of Non-Hydrogenic Spectral Lines for Low Electron Density and High Pressure Plasma Diagnostics,” *Plasma Sources Science and Technology*, vol. 18, no. 3, pp. 035 011–9, May 2009.
- [67] K. Honglertkongsakul, “Optical Emission Spectroscopy of Argon Plasma Jet,” *Advanced Materials Research*, vol. 770, pp. 245–248, Sep. 2013.
- [68] C. A. Bye and A Scheeline, “Saha-Boltzmann Statistics for Determination of Electron-Temperature and Density in Spark Discharges Using an Echelle Ccd System,” *Applied Spectroscopy*, vol. 47, no. 12, pp. 2022–2030, Dec. 1993.
- [69] *PrismSPECT User’s Guide*, Prism Computational Sciences, Inc, 2018.
- [70] J. B. Boffard, R. O. Jung, C. C. Lin, L. E. Aneskavich, and A. E. Wendt, “Argon 420.1-419.8 nm Emission Line Ratio for Measuring Plasma Effective Electron Temperatures,” *Journal of Physics D: Applied Physics*, vol. 45, no. 4, pp. 045 201–12, Jan. 2012.
- [71] J. R. Taylor, *An Introduction to Error Analysis: The Study of Uncertainties in Physical Measurements*, 2nd. University Science Books, 1982.